THESIS

POST-TRANSMISSION PARALLEL HYBRID VEHICLE DESIGN AND VALIDATION FOR PREDICTIVE ACCELERATION EVENT ENERGY MANAGEMENT STRATEGIES

Submitted by

Derek Adelman

Department of Mechanical Engineering

In partial fulfillment of the requirements

For the Degree of Master of Science

Colorado State University

Fort Collins, Colorado

Summer 2021

Master's Committee:

Advisor: Jason Quinn

Bret Windom
Thomas Bradley

ABSTRACT

POST-TRANSMISSION PARALLEL HYBRID VEHICLE DESIGN AND VALIDATION FOR PREDICTIVE ACCELERATION EVENT ENERGY MANAGEMENT STRATEGIES

Hybrid and electric vehicle technologies provide automotive engineers with the potential to improve vehicle performance and fuel economy through control systems that can utilize optimal energy management strategies (EMS), vehicle-to-everything (V2X), and predictive controls [1] [2] [3] [4] [5] [6]. As described in previous work [7], one such EMS being studied is predictive acceleration events (PAEs), a method that derives optimal energy management for a set of pre-defined AEs and applies said management during AEs to realize real-time energy consumption savings. To further this concept, a hybrid test vehicle platform (TVP) was constructed to test the validity of the EMS strategy, as well as to serve as a test bed for future V2X and prediction technologies being researched at Colorado State University. This thesis covers the design, manufacture, and testing of the TVP as it pertains to the hybrid powertrain, high voltage cooling systems, low voltage control hardware, and controller area network (CAN) communication. Powertrain component design and modeling via finite element analysis (FEA), manufacture and cryogenic assembly, validity of economical identification of low-alloy steels, and heat treatment theory in inert atmospheres and methodology is discussed. Quasi-equilibrium modeling of interconnected cooling loops to predict steady-state operating temperatures is presented along with construction and experimental results during EMS implementation. The sections on low voltage design and integration into the TVP discuss the details of power distribution and consumption of third-party system controllers and high voltage components, accelerator pedal signal modification via frequency modulation and signal conditioning, and off-schedule transmission shifting through modification of the stock vehicle sport mode. Finally, qualitative and quantitative testing of vehicle networking and communication through CAN under electromagnetic interference is presented.

ACKNOWLEDGEMENTS

I would like to thank my advisor, Dr. Bradley, for the opportunity to continue my education in mechanical engineering at Colorado State University and the constant support in the development of the Test Vehicle Platform project. I would also like to thank Dr. Quinn for his support, guidance, and never-ending patience during the EcoCar years that ultimately led me to graduate school.

I would also like to thank Toyota, Ms. Lisa DiMaggio, and Ms. Monica Vanterpool for their sponsorship and support of this project, it has not only forwarded technology and innovation, but also the lives of many young engineers.

DEDICATION

To my parents, for without their love and support I would not be who I am today.

TABLE OF CONTENTS

LIST OF TABLES

LIST OF FIGURES

Chapter 1: Introduction

Hybrid vehicles are generally defined as having two power sources that are capable of motoring the vehicle [8]. The hybrid powertrain is the system of drive components (shafts, gears, engines, electric motors, etc.) that delivers energy from the power sources to the wheels. Two primary powertrain configurations exist. The first is a series hybrid, where only one power source is capable of directly driving the wheels. The most common series configuration uses the electric motor (EM) to drive the wheels with the internal combustion engine (ICE) acting as a generator charging the high voltage battery pack. The ICE cannot directly provide power to the wheels; however this allows the ICE to run in its most efficient operating range. The second powertrain configuration is a parallel hybrid where both electric motor(s) and ICE can provide power to the wheels at the same time. Parallel configurations often use smaller electric motors and battery packs, using them in tandem with the ICE to increase fuel economy. There are five main parallel hybrid configurations, denoted P0 through P4 (parallel-0, parallel-1, etc.) with the number signifying the position of the electric motor with respect the ICE and transmission. P0 corresponds to placing the EM pre-ICE, P1 post-ICE and before any clutches connecting the ICE and transmission, P2 post-ICE and after any clutches, P3 after the transmission but before the propulsion shaft, and P4 generally replaces the differential or is located in the wheel hubs [9]. Note that in P0 and P1 configurations, the tractive elements of the vehicle (the wheels) can never be decoupled from the ICE, whereas in P2-P4 it can via clutches or the transmission. For the TVP project, it is seen in [10] the architecture selected was a P3-parallel hybrid. This was largely due to the relative simplicity in construction and control required.

Chapter 2: Hybrid Powertrain

2.1 Component Overview

In [10], the YASA (Yokeless And Segmented Armature) [11] axial flux electric motor was selected to be the electric drive of the TVP. This is largely because the dimensions and power capabilities of the YASA make it an ideal fit for the P3 configuration in the selected vehicle (2018 Toyota Tacoma). Figures 1 and 2 show an exploded and collapsed view of the powertrain designed and fabricated for the P3 hybrid architecture. Table 1 summarizes the components listed in the exploded view. These parts will be referenced repeatedly in the following subsections. Each subsection will cover an individual part design and manufacture followed by an overview of how the powertrain was assembled. The final section will cover testing of the powertrain.

Referencing the exploded view, the YASA motor was mounted onto the "tailstock" of the transmission, a conical aluminum casting (Part A) that covers the transmission output shaft until it reaches the output shaft slip yoke. In a four-wheel drive Toyota Tacoma, the transfer case would be in the place of the tailstock. The motor mounting consists of an aluminum collar (Part D) welded to the shoulder of the tailstock with a flat aluminum plate (Part I) bolted to it. The YASA motor is then bolted to the flat aluminum plate. The YASA has an internally splined hub that drives an externally splined shaft (Part G). The YASA transmits torque to the hybrid drivetrain by adding or removing torque directly from driveshaft at the output of the transmission and before the propulsion shaft, via the externally splined shaft.

The original Toyota drivetrain was modified to accommodate the YASA motor in its post-transmission installation location. Several steps were taken to accomplish this, using a combination of modified stock components and manufactured new ones. First, the stock slip yoke (Part E) was modified to have a flange plate instead of yoke ears. A slip yoke connects a driveshaft to a universal joint via a splined connection that is not fully constrained axially, allowing the slip yoke to slide axially when the propulsion shaft length changes due to vehicle suspension movement. Yoke ears are the two holes of the

slip yoke that receive the bearings of the universal joint. The flange of the modified slip yoke mates to the externally splined shaft that passes through the internally splined hub of the YASA, protruding from the YASA and mating to another modified slip yoke (Part L). This slip yoke then connects to a shortened propulsion shaft, applying drive torque to the rear differential. The flanged connection between Part E and Part G resides in a pocket formed by the interface of Part D and Part I as seen in the section view. Since this flanged connection is covered by the YASA, it must be constrained axially to keep it from sliding into the motor. To do this, an axially hole was drilled through Parts G and E, ending with a tap into the transmission output shaft (Part C). A screw was then used to clamp the assembly of Part G and E to the transmission output shaft.

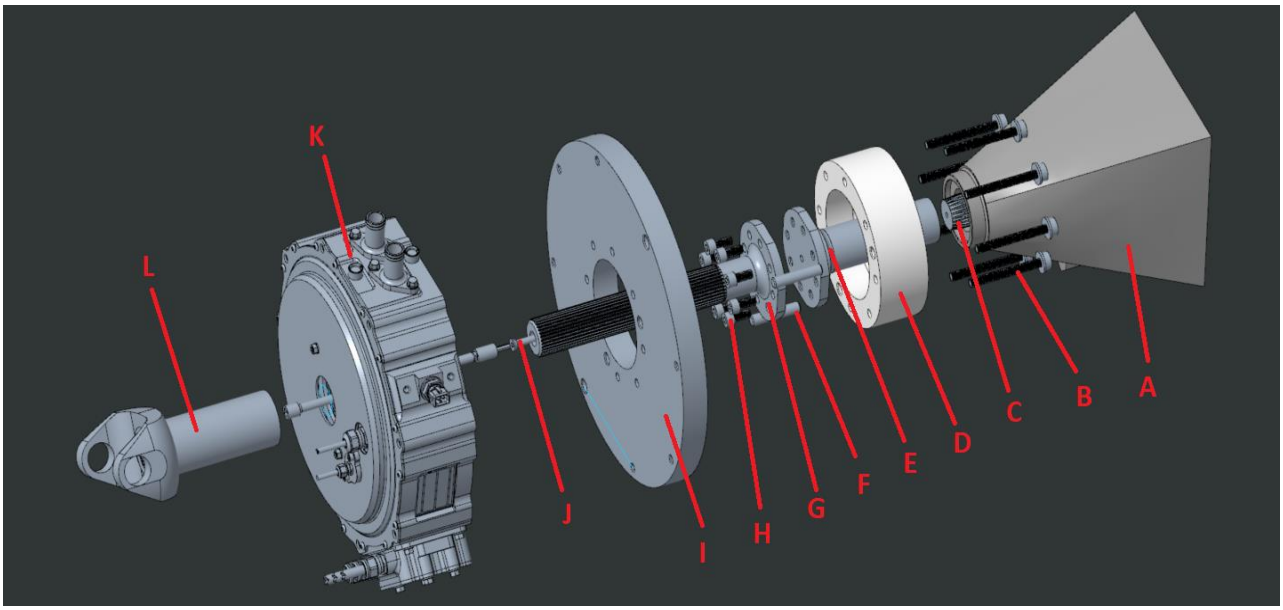

Figure 1: Hybrid powertrain exploded view

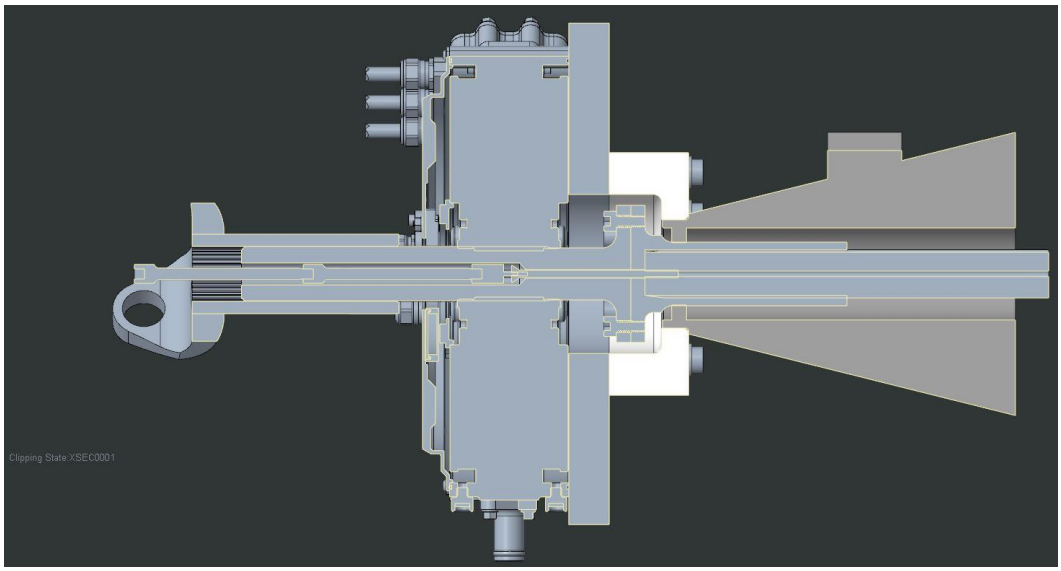

Figure 2: Hybrid powertrain collapsed, section view

Table 1: Hybrid powertrain component list

Part	Colloquial Name	Material	Notes
A	Tailstock	Cast aluminum (AL) alloy	Cast A300 series
B	Mounting bolts	Class 12.9 hardened steel alloy	M8x1.25
C	Transmission output shaft	Unknown	Likely hardened 4140 or 4340 alloy steel
D	Donut	AL 6061-T6	
E	Modified slip yoke	Hardened 4140 (flange)	Stock part of component is likely either 4340 or 4140
F	Alignment pins	316 stainless steel	Dia. M10
G	Flanged shaft adapter	17-4 precipitate hardened (PH) stainless steel	Hardened to H925 condition
H	Flange bolts	Class 12.9 hardened steel alloy	M8x1.25
I	Dinnerplate	AL 6061-T6	Thickness is minimum allowed by screw/thread design
J	Retainment screw	18-8 stainless steel	
K	YASA	AL 6061-T6 Casing, Unknown hardened steel internal spline	Mass 27.5 kg
L	Custom slip yoke	Hardened 4340 (internal spline tubing)	Stock component is likely either 4340 or 4140

2.1.1 Part A and D

As previously mentioned, the YASA mounts to the tailstock via a cylindrical collar. This part is also referred to as Part D, or the “donut.” The challenge of connecting the donut to the tailstock was in maintaining concentricity of the circular features of the donut to the axis of the transmission output shaft, maintaining flatness of the donut surface relative to the tailstock base, and carrying the counter-torque load produced by the YASA (note that the YASA had to be mounted directly to the tailstock to ensure that the YASA was suspended relative to the vehicle chassis/body, i.e. soft mounted. The tailstock bolts

to the transmission, which is soft mounted to the transmission cross member). To meet the requirements for mechanical loading and alignment, it was decided to shrink fit the donut onto the tailstock. The shrink fit, in theory, would align the donut concentrically and the compression from the fit would also carry the torque load from the YASA. To do this, a machined outer surface and shoulder were required on the tailstock and luckily both were present on the stock component, Figure 3.

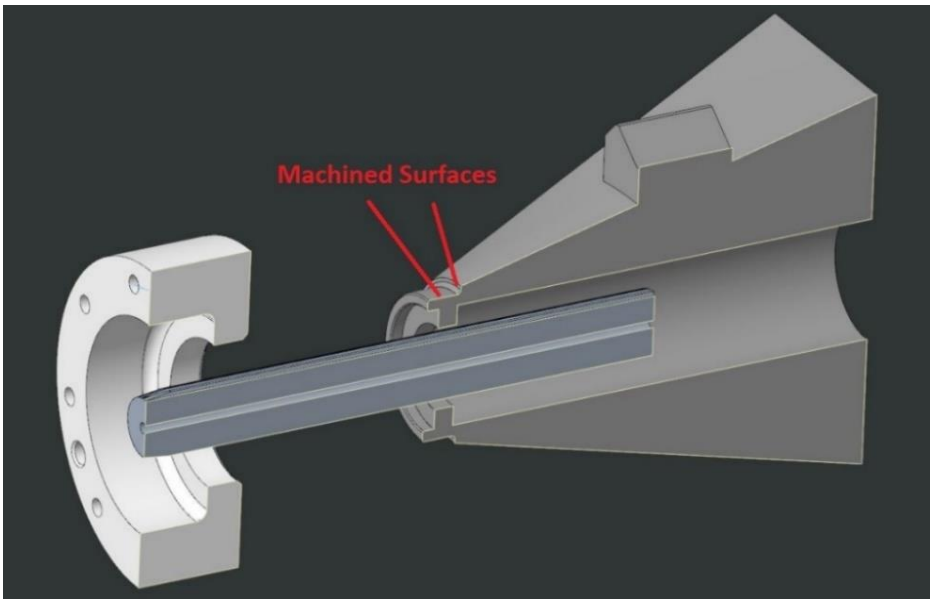

Figure 3: Part D to A interface

To determine the torque carrying capacity of this connection, the contact pressure between the two components after the shrink fit was calculated. This can be done by analyzing the connection using thick-walled cylinder stress equations. Looking axially at the above figure, the system can be represented in Figure 4:

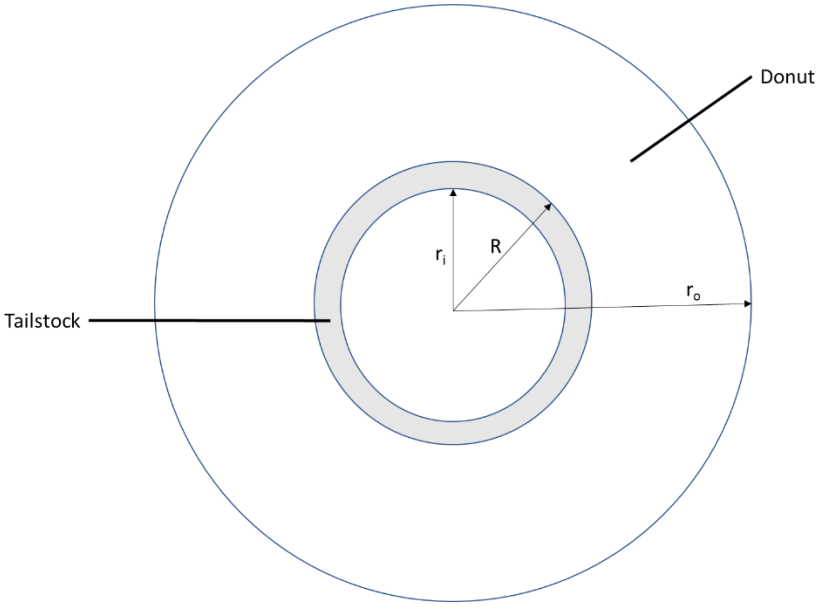

Figure 4: Part D and A radial definitions

where r_i is the inner radius of the tailstock collar, r_o the outer radius of the donut, and R the radius of the interface (where the machined surface is). Lamé's equations for thick wall cylinders, defined as having wall thicknesses greater than 1/20th the diameter [12], for circumferential (σ_c) and radial stress (σ_r), respectively, are:

$$\sigma_c = \frac{r_i{}^2 p_i - r_o{}^2 p_o}{(r_o{}^2 - r_i{}^2)} + \frac{(p_i - p_o) r_i{}^2 r_o{}^2}{(r_o{}^2 - r_i{}^2) R^2} \qquad \textit{Equation 1}$$

$$\sigma_r = \frac{r_i{}^2 p_i - r_o{}^2 p_o}{(r_o{}^2 - r_i{}^2)} - \frac{(p_i - p_o) r_i{}^2 r_o{}^2}{(r_o{}^2 - r_i{}^2) R^2} \qquad \textit{Equation 2}$$

where p_i and p_o and the internal and external pressures acting on the cylinder. The interface pressure for an interference fit is:

$$p = \frac{\delta_r}{\frac{R}{E_o}\left(\frac{{r_o}^2 - R^2}{{r_o}^2 - R^2} + v_o\right) + \frac{R}{E_i}\left(\frac{{r_i}^2 - R^2}{{r_i}^2 - R^2} + v_i\right)} \qquad \textit{Equation 3}$$

where E_o and v_o are the modulus of elasticity and Poisson's ratio for the outer material or hub, respectively, and similarly for E_i, v_i for the shaft, and δ_r the radial interference. If we assume the tailstock and donut have the same E and v, (3) becomes:

$$p = \frac{E\delta_r({r_o}^2 - R^2)(R^2 - {r_i}^2)}{2R^3({r_o}^2 - {r_i}^2)} \qquad \textit{Equation 4}$$

For $r_i = 57.86\ mm$, $r_o = 152.4\ mm$, $R = 68.05\ mm$, $E = 68.9\ GPa$, and an interference of $\delta_r = 0.075\ mm$, the contact pressure is $p = 9.839\ MPa$. Looking at equations (1) and (2) we can plot the circumferential and radial stresses for the tailstock and donut, Figures 5 and 6.

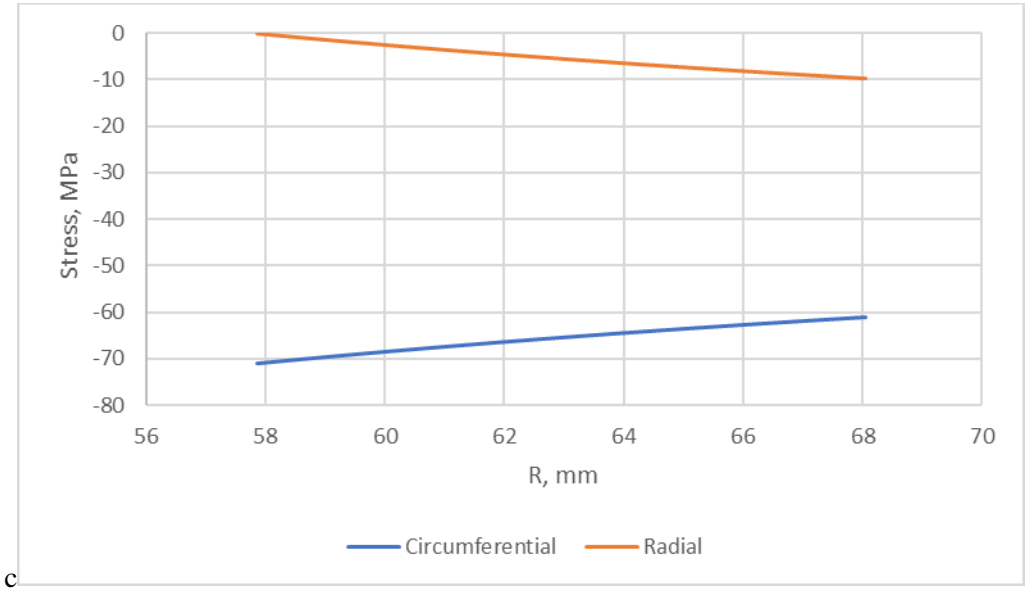

c

Figure 5: Calculated stress in Part A

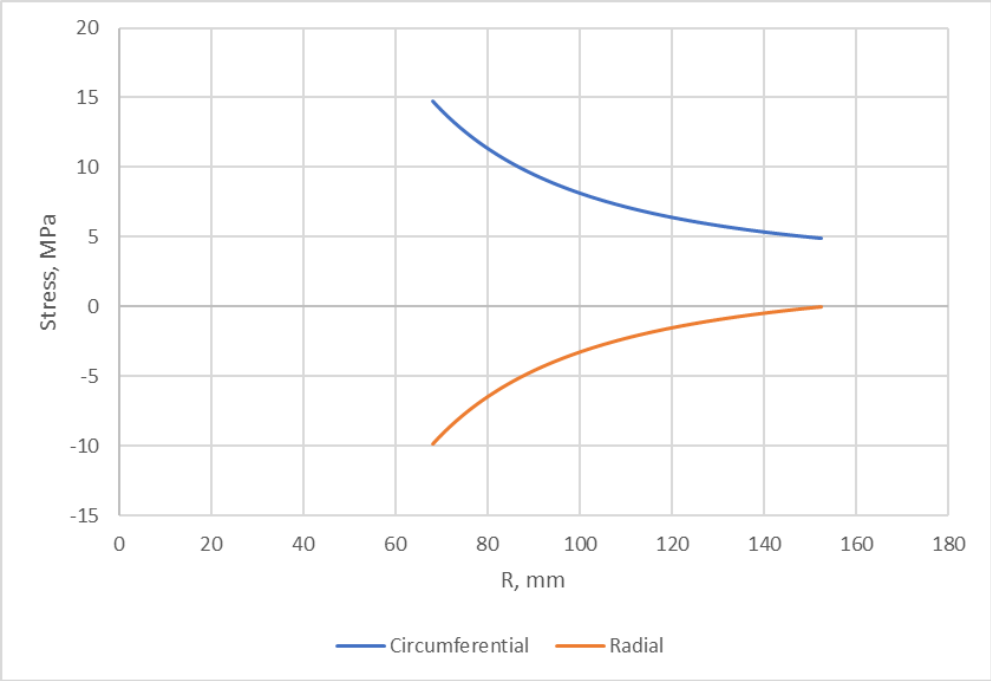

Figure 6: Calculated stress in Part D

We see from both plots that the maximum circumferential or radial stress is well below the yield tensile stress of the AL material (~240 MPa). Using the stresses above and calculating the axial stress due to torque load, the Von Mises stress can also be calculated [13]. Given the relatively low stresses from the shrink fit this calculation is not presented here.

Knowing the contact pressure, the maximum torque load of the shrink fit can be calculated from the following equations:

$$T = rF_f \qquad \textit{Equation 5}$$

$$F_f = \mu F_N \qquad \textit{Equation 6}$$

$$F_N = pA \qquad \textit{Equation 7}$$

where F_f is the static frictional force of the shrink fit, T the maximum torque load, F_N the normal force due to compression at the fitting surface, A the contact area, μ the coefficient of static friction, and r the radial distance to the fitting surface. Using a coefficient of static friction of 1.25 for clean dry aluminum on aluminum, total contact area $A = 2945\ mm^2$, $r = 68.0\ mm$, and $p = 9.839\ MPa$, the theoretical maximum torque load the fitting can carry is $T = 2464.64\ Nm$. This is well above the maximum torque the YASA can produce of ~400 Nm.

The donut was thermally shrunk-fit onto the tailstock by cooling the tailstock with liquid nitrogen. Given the size and irregular shape of the tailstock, experiments were performed to see how much the diameter of the machined surface would shrink, Figure 7.

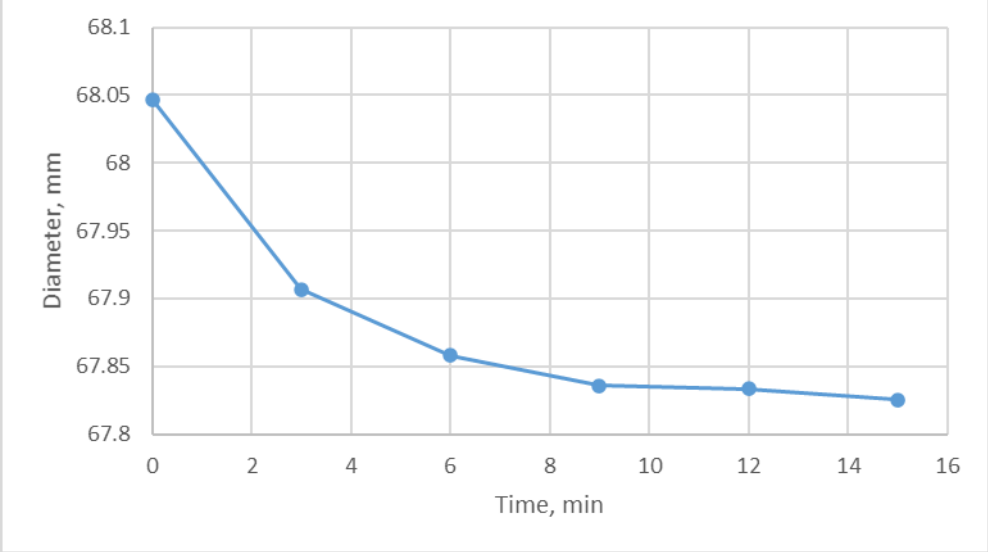

Figure 7: Radial shrinkage of Part A interface when submerged in liquid nitrogen over time

As seen in the above figure, the tailstock collar shrunk 0.22 mm in diameter in 15 minutes. This was enough for an interference of 0.075 mm, however given manufacturing tolerance and defects the donut was also heated in an oven to 175˚C to ensure the fitting process would go smoothly. After fitting,

the flatness of the donut face was measured on a granite surface plate. To do this, the base of the tailstock (the end that bolts to the transmission) was place on the granite surface plate and a dial indicator was used at several locations to measure the deviation in height (from surface plate to donut face) from the center horizontal. The relative locations are shown in Figure 8.

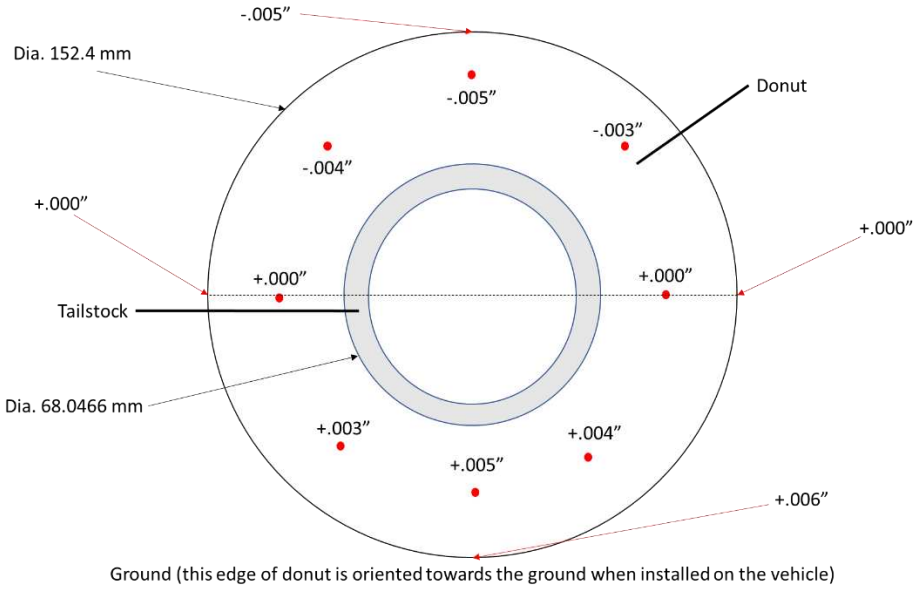

Figure 8: Measured flatness of Part D mounting face relative to Part A interface to transmission

Noting that Part I mates to the face shown in the above figure, the deviations shown would get multiplied several times due to the increased diameter of Part I. This setup would not meet the alignment requirements for the YASA [14]. The simple solution was to fix the mated tailstock and donut assembly into a CNC mill and plane the mounting face with a fly cutter. Extra thickness in the axial direction of the donut was incorporated into its original manufacture for this very purpose.

To ensure the donut would not move during the manufacturing process relative to the tailstock and to help carry cantilever forces, it was decided to also weld the donut to the tailstock on the backside interface, Figure 9. While this partially defeated the purpose of the shrink fit, the fit is still a viable method to concentrically align parts pre-welding and to help maintain alignment before final machining. The welding work was performed by Distinctive Welding, Inc., a local welding shop in Fort Collins that

has extensive experience with a variety of welding techniques and materials. For circumferential machining operations, the inside surface of the tailstock collar was used to generate a reference axis.

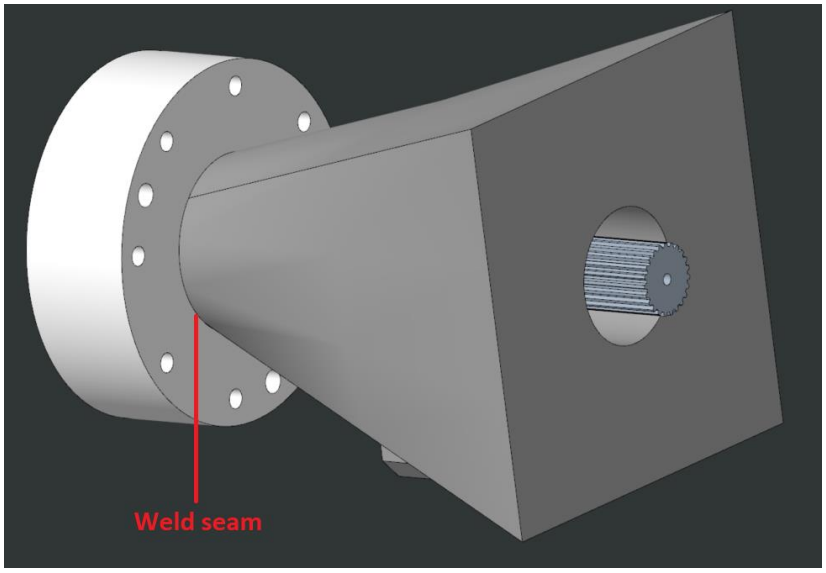

Figure 9: Part D and A interface weld seam location

2.1.2 Part I

Mounting to the donut is Part I, the "dinnerplate", which is simply a large, flat plate that serves as a surface for the YASA to mount to. The key challenge of this part was aligning the outer bolt pattern that attaches the YASA concentrically with the transmission output axis. This was accomplished by first mounting and assembling the dinnerplate to the donut/tailstock subassembly via the inner bolt pattern and then using the inside surface of the tailstock collar as an axial reference for the outer bolt pattern. To ensure accurate, repeatable alignment between the dinnerplate and driveshaft axis, two M10 alignment pins (Part F) were inserted 135˚ apart through the dinnerplate and donut using a locational transition fit. The alignment holes were drilled at the same time as the outer bolt pattern.

The fasteners used to secure the dinnerplate to donut are Class 12.9 M8x1.25 socket head cap screws. The torque required for these bolts at various proof loads can be calculated using the standard fastener equations or found in machinists' tables [15] [16]. However, these calculations and tables are often for fasteners engaging into the same material. In this instance, the alloy steel of the M8x1.25 is

engaging into 6061-T6 AL. Since the aluminum has much lower strength than the steel, a longer thread engagement is needed to ensure the internal threads will not strip when the fastener is proof loaded. The needed thread engagement is calculated using a correction factor comprised of the ratio of yield strength of the fastener to the yield strength of the internally threaded material.

$$J = \frac{S_{yS}}{S_{yAL}} \qquad \textit{Equation 8}$$

$$Corrected\ Thread\ Engagement = J * Nominal\ Thread\ Engagement \qquad \textit{Equation 9}$$

where S_{yS} is the yield strength of the alloy steel fastener and S_{yAL} of 6061-T6. Class 12.9 fasteners have a minimum yield strength of 1100 MPa and 6061-T6 has a yield strength ranging from 240 to 280 MPa [17] [18] [19]. Using 275 MPa results in the correction factor, $J = 4$. The standard metric thread engagement formula is:

$$Min.thread\ engagement\ (mm) = \frac{2A}{0.5\pi(D - 0.6952P)} \qquad \textit{Equation 10}$$

where A is the stress area of the fastener (36.6 mm^2 for M8 fasteners), D is the diameter of the fastener (8 mm for M8), and P is the pitch (1.25 mm/thread for M8x1.25). This results in a minimum thread engagement of a similar material connection of 6.53 mm. Multiplying by our correction factor, we get a minimum thread engagement for the alloy steel to aluminum interface of 26.14 mm.

For the manufacture of the dinnerplate, a 1” (25.4 mm) thick piece of raw stock was selected as it was the closest from the available sizes [20]. To machine the outer diameter and mounting surfaces, the inner bolt pattern was first drilled and tapped into the raw stock in a CNC mill. Then a special lathe mandrel with a flange at one end was bolted onto the raw stock. This allowed a +12” diameter aluminum plate to be mounted in the lathe to face the outer edge and exposed face. The plate was then secured back into the CNC mill that routed the inner 100 mm diameter hole. Figure 10 shows the subassembly of the donut, dinnerplate, transmission and YASA.

Figure 10: Assembly stack of Part D, A, I, YASA, and transmission

2.1.3 Part E

The goal of Part E or the “modified slip yoke” was to be able to reuse the internal splines of the stock slip yoke and to replace the yoke ears with a flanged connection to connect the hybrid drivetrain to the transmission output shaft. The design of this part includes determining the size of the flange, bolt pattern, and diameter of the weld seam connecting the flange to the earless slip yoke, Figure 11. The primary load case of this part is a torque of 2000 Nm, corresponding to the combined maximum output of

the internal combustion engine and electric motor, reflected through the torque multiplication of the transmission.

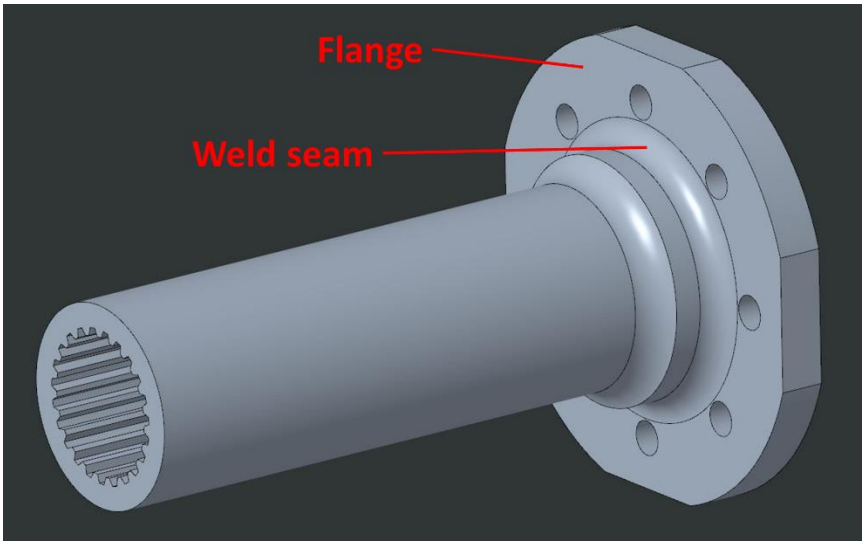

Figure 11: Part E weld seam location

The 2018 Toyota Tacoma in possession of CSU has an inline 4-cyl, 2.7L ICE capable of 180 ft·lbs at 3,800 rpm and a first gear ratio of 3.6 for the 6-speed automatic. Running a simple conversion results in a maximum torque output post-transmission of 878.57 Nm. Adding the maximum torque of the EM to this results in 1278.57 Nm. To ensure a factor of safety, this number was rounded up to 2000 Nm.

Looking first at the design of the flange connection, there were several free variables to choose from that would determine the others: namely bolt size, flange diameter, flange thickness, number of bolts, and factor of safety. The free variables chosen were a flange diameter of 90 mm to fit in the donut pocket of diameter 100 mm, a bolt pattern diameter of 66 mm as it provided space for various fastener head sizes as well as varying weld seam diameters, Class 12.9 fasteners, and a factor of safety (FOS) greater than or equal to 2. The end goal was to determine the bolt size and number needed to meet the load case of 2000 Nm. The bolt material selected has a minimum ultimate tensile strength of 1220 MPa and yield of 1100 MPa. The 80% proof strength is 976 MPa. For ductile materials, it is common practice to take the ultimate shear strength as 60% of the ultimate tensile strength based on maximum distortion

energy theory [21]. It is important to note that shear capacity is further reduced by the fact that the bolt is in tension. It is assumed that for 80% proof loading, the shear capacity decreases by another 10-15%. This is based on reference [22], which showed experimentally that the shear stress capacity of high-strength bolts in tension appreciably decreases for tension loads upwards of 60% the ultimate tensile strength. From maximum distortion energy theory and a further 10% decrease due to bolt pre-load, the ultimate shear strength is modeled as:

$$S_{us} = 0.5S_{ut}, \qquad \textit{Equation 11}$$

or 610 MPa. For proof loading, this corresponds to 488 MPa. This means for a FOS greater than or equal to 2, the shear stress per bolt needs to be less than 244 MPa. Bolt size and number can now be determined.

The shear load per bolt at the bolt pattern radius, r, can be determined from

$$F_s = \frac{T}{rn} \qquad \textit{Equation 12}$$

where n is the number of bolts in the pattern. For the size of the flange, the number of bolts that could be accommodated was roughly 4-10. Using custom spreadsheet software to evaluate these tradeoffs, it was found for four bolts, the required size would be an M12, too large for the application. For a pattern of 10 bolts, an M8 is required to still meet the requirement for stress per bolt of 244 MPa (10, M6 bolts had a stress per bolt >244 MPa). Decreasing to 8 bolts, the stress per bolt was found to be 206 MPa. Thus, an 8-bolt pattern of M8x1.25 Class 12.9 fasteners was selected. This also determined the flange thickness to be at least 6.53 mm from equation (10), so 9 mm was chosen (18 mm total thickness of flange connection).

For the weld calculation, the weld shear stress is determined from

$$\sigma_w = \frac{2T}{\pi D^2 a}$$ *Equation 13*

where a is the throat length of the weld. Throat length is calculated as $a = \sqrt{2}L$, where L is the width of the weld, assumed here to be 0.25" (6.35 mm). Assuming the weld has the same mechanical properties as the parent materials and using the distortion energy theory, S_{us} occurs at a diameter of approximately 20 mm. Given this is significantly smaller than the bolt pattern diameter of 66 mm, the radius was extended in CAD until there was just enough room for the threaded end of the fastener (the fastener threads into the modified slip yoke). This resulted in a weld diameter of 48.5 mm and a corresponding weld stress of roughly 120 MPa, a FOS of 6.

With the main features of the modified slip yoke designed, a CAD model was developed and simulated in FEA software to confirm the calculations above, Figure 12.

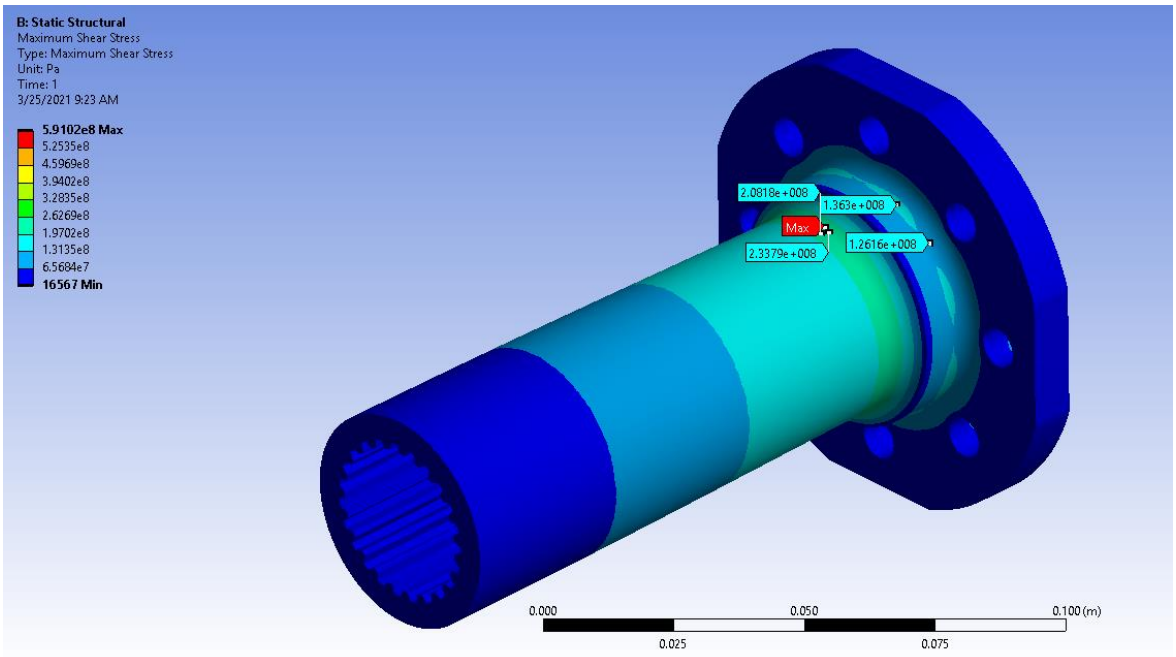

Figure 12: Part E weld seam shear stress concentration, 2000 Nm load case, Pa

As is seen in the above figure, the stress in the weld seam (~126-136 MPa) agrees well with the hand design calculations illustrated above. Note that the maximum shear stress occurs at a fillet that is part of the original stock component. This maximum does not correspond to the scale maximum on the left side of the plot, as the FEA analysis was performed on the assembly of Part E, the fasteners, and Part G, and as such, is the maximum stress in the entire assembly. It is assumed that the stock part was designed with a large enough safety factor to be able to handle the 2000 Nm load case. The strength of this material will be further discussed in the heat treatment section. The post-heat treat manufactured part is shown in Figure 13. Note the flange face and alignment edges were faced in a CNC mill to remove scaling and a muriatic acid bath was used to remove scale on the internal splines.

Figure 13: Part E post-heat treat condition

Looking at the bolt pattern in Figure 14, we see the FEA results agree with the designed stress per bolt of 206 MPa, as the probed locations range from 160 to 210 MPa. For the bolt pattern FEA, it is assumed that the frictional forces between the two flange surfaces are zero and therefore carry no torsional load. In reality, the frictional forces will carry nearly all the load, so the bolt pattern is designed for a worst case. Note the maximum occurs at a highly localized stress concentration and is a numerical artifact as it is not present in any of the other fasteners. This is the maximum stress of the assembly.

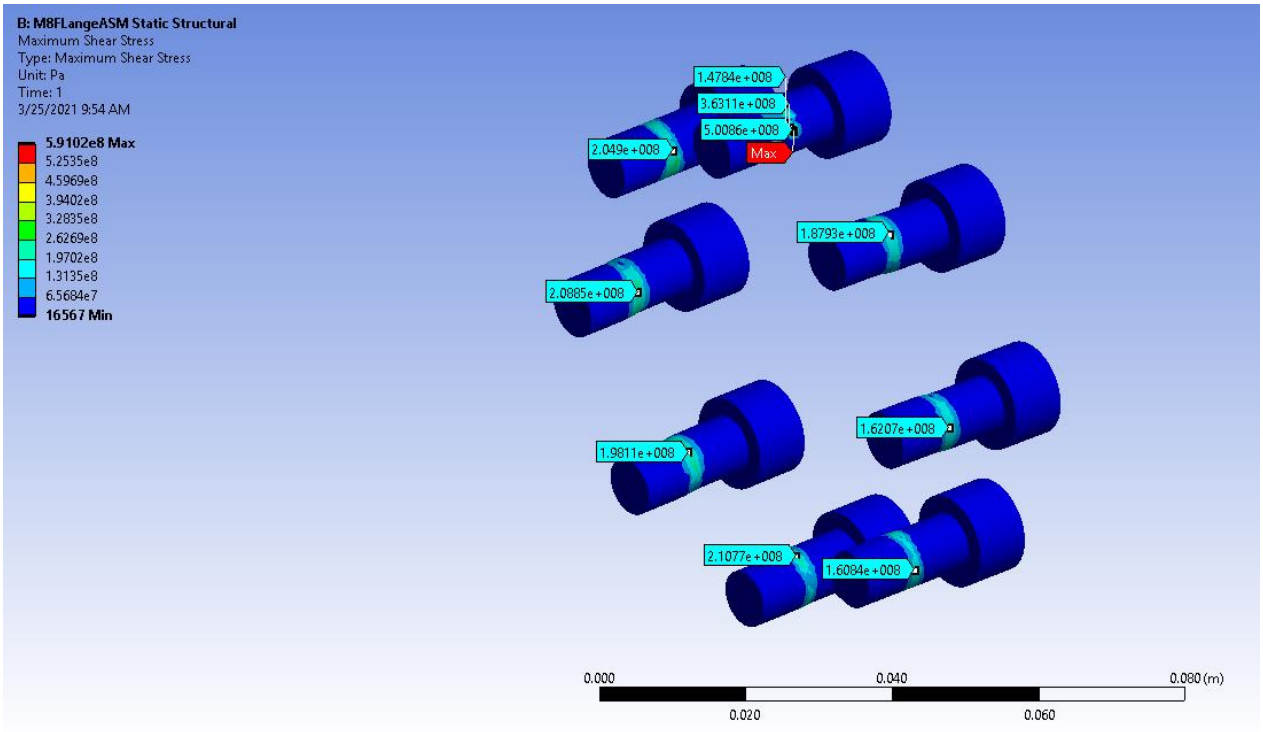

Figure 14: Shear stress concentration for Part H, 2000 Nm load case, no flange friction, Pa

If frictional force is considered with a static friction coefficient of 0.75 and the 8-M8x1.25 bolts each pre-loaded to 976 MPa, the following FEA results, Figure 15. Note the shear stress is on the order of 50-80 MPa, well below the designed 206 MPa per bolt.

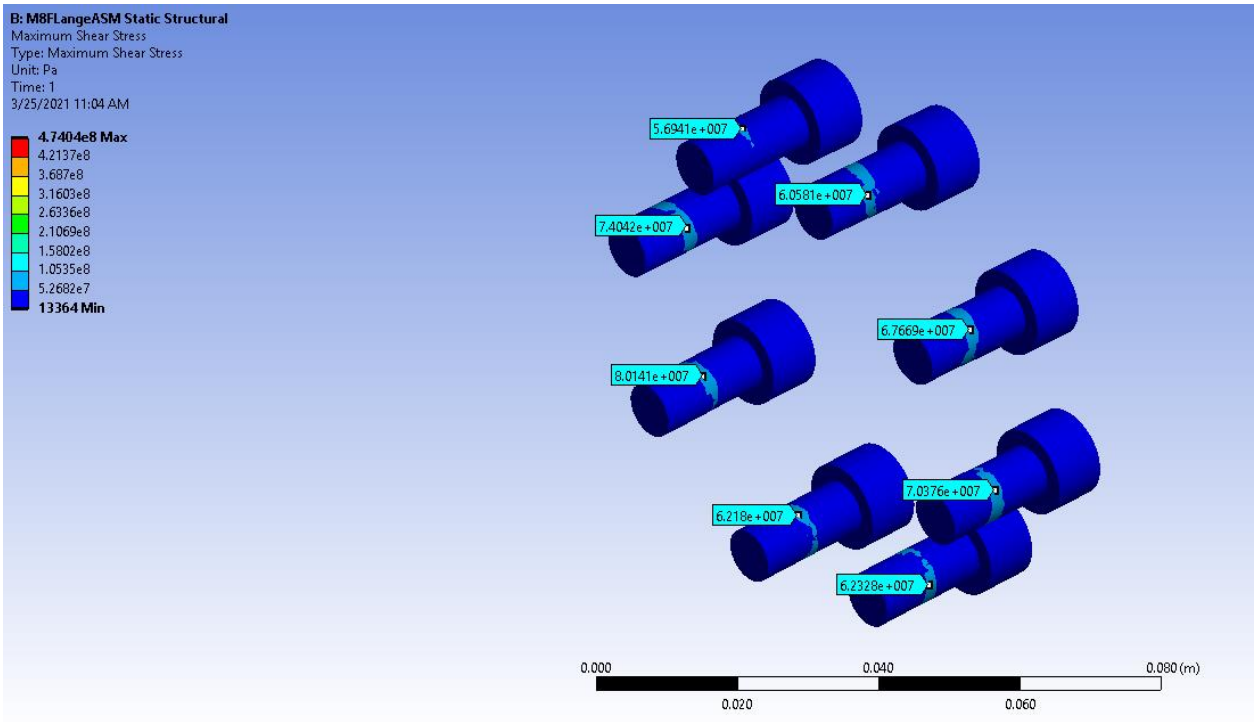

Figure 15: Shear stress concentration for Part H, 2000 Nm load case, flange friction, Pa

2.1.4 Part G

Mating to Part E is Part G or the "flanged shaft adapter." The main feature of this part are the external splines that mate to the YASA EM, allowing the EM to add torsion to the hybrid powertrain. The primary design constraints are the available space for the fillet connecting the flange of Part G to the shaft section and the form factor of the YASA splines.

The fillet is the primary stress concentration and needs to be able to withstand the load case of 2000 Nm. The FOS design requirement is 1.75. The fillet feature was designed using an iterative process of CAD modeling and FEA analysis. The results of this design process are shown in Figure 16. Note that Part G is made of 17-4 precipitate hardened stainless steel in the H925 condition (see Heat Treatment section). The yield stress of this material is approximately 1150-1170 MPa. By the maximum energy distortion theory, this results in a shear yield stress of 690 MPa. Referencing Figure 16, it is seen the maximum shear stress in the fillet is approximately 350 MPa, resulting in a FOS of ~1.9.

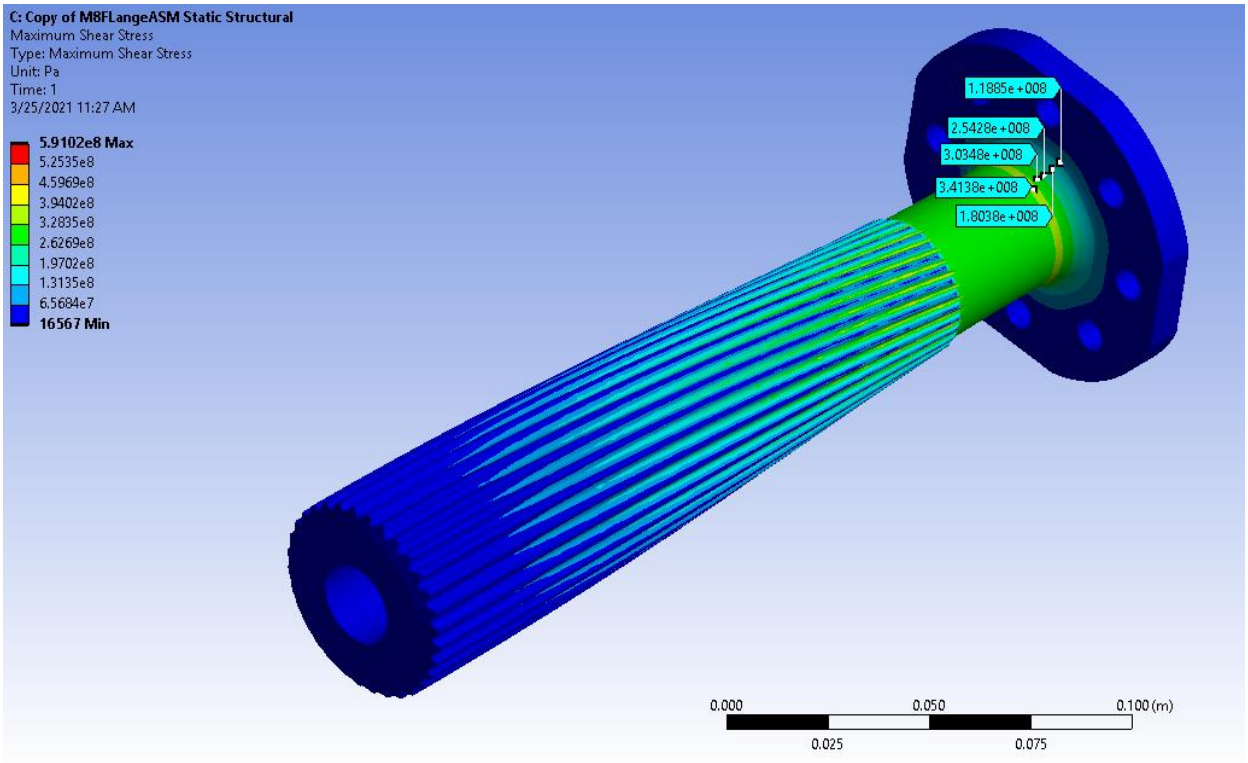

Figure 16: Part G shear stress concentration, 2000 Nm load case, Pa

The design of the splines was relatively straightforward, given the form factor of the YASA internal splines in Figure 17 [23].

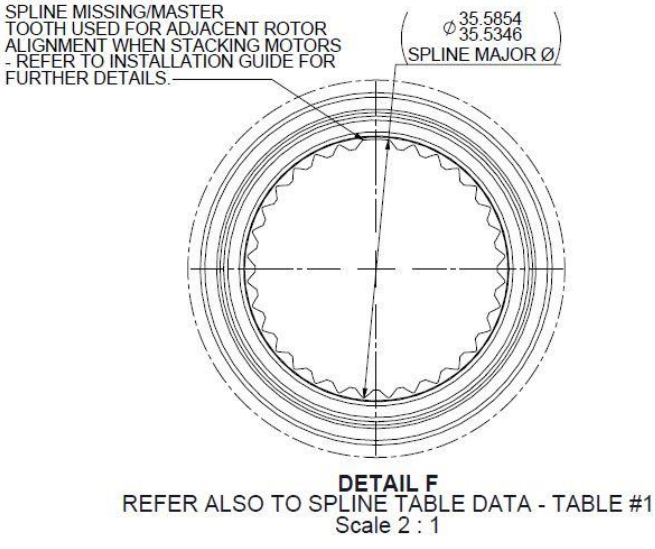

TABLE #1 - INVOLUTE SPLINE DATA INTERNAL SPLINE TO ANSI B92.1-1996 PAGE 70	
SPLINE TYPE	FILLET ROOT SIDE FIT
NUMBER OF TEETH	32
SPLINE PITCH	24/48
PRESSURE ANGLE	45°
BASE DIAMETER (REF.)	19.4572 [0.9428091]
PITCH DIAMETER (REF.)	33.8666582 [1.333333]
MAJOR DIAMETER (MAX.)	35.5854 [1.401]
FORM DIAMETER	35.0266 [1.379]
MINOR DIAMETER	33.3756/33.2486 [1.314/1.309]
CIRCULAR SPACE WIDTH [TOL. CLASS 5]	
MAX. ACTUAL	1.94564 [0.0766]
MIN. EFFECTIVE	1.87452 [0.0738]
MIN. ACTUAL (REF.)	1.91211 [0.0753]
INSPECTION DATA	
MAX. MEASUREMENT BETWEEN PINS (REF.)	30.89402 [1.2163]
PIN DIAMETER	2.032 [0.08]
[DIMENSIONS IN INCHES SHOWN IN BRACKETS]	

SEE SHEET 3 FOR RECOMMENDED SPLINE SHAFT.

Figure 17: YASA internal spline design specifications [23]

Using the standard spline design formulas found in [15] the mating external splines to those in the above figure are shown in Figure 18. It was decided to use a tolerance class 6 to ensure a snug fit between the shaft and the YASA as the spline type for the shaft is straight side fillet root instead of involute side fillet root. The reasons for using a straight side fillet root were that it was easier and more cost effective to manufacture with the available equipment, the relative size of the spline teeth were small enough that the difference between straight and involute was negligible, and custom tooling was not required.

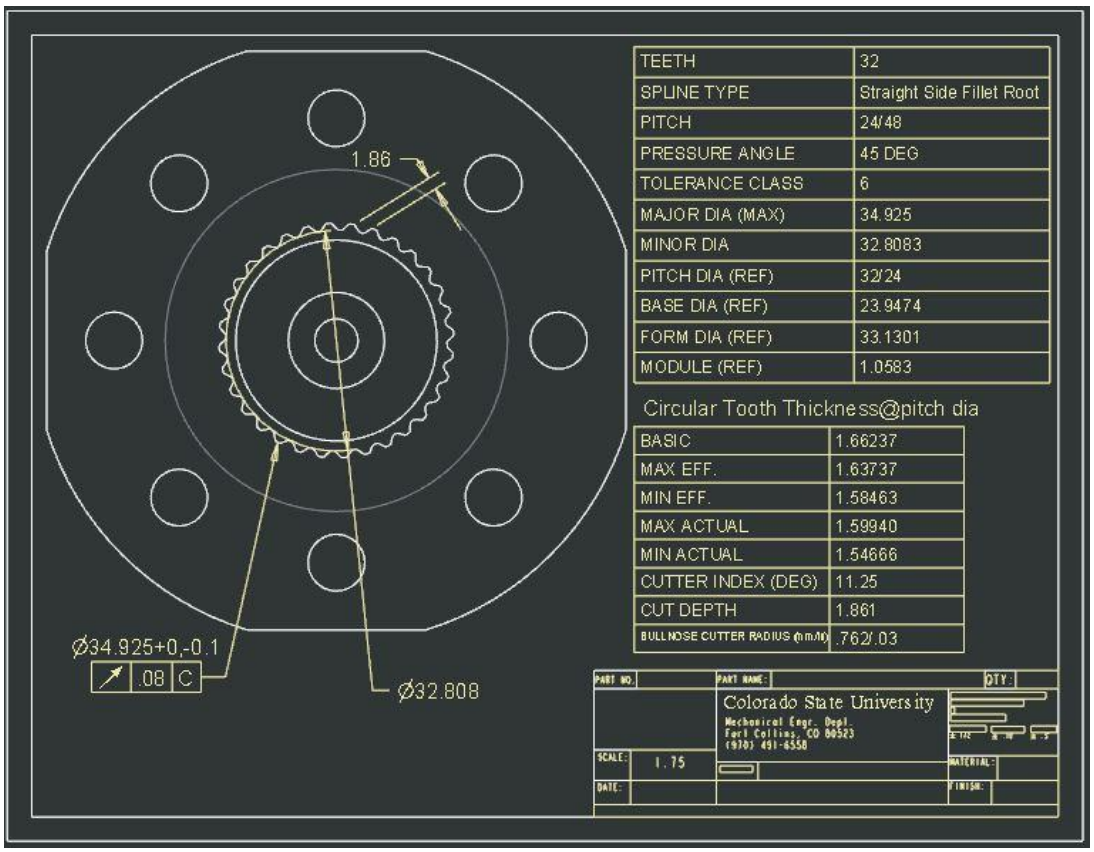

Figure 18: Part G external spline design specifications

The manufacture of the flanged shaft adapter required a four-axis CNC milling machine. Given the part complexity, Figure 19, and the equipment required, the final version of the part was manufactured at the CSU EMEC by Dr. Steven Schaeffer.

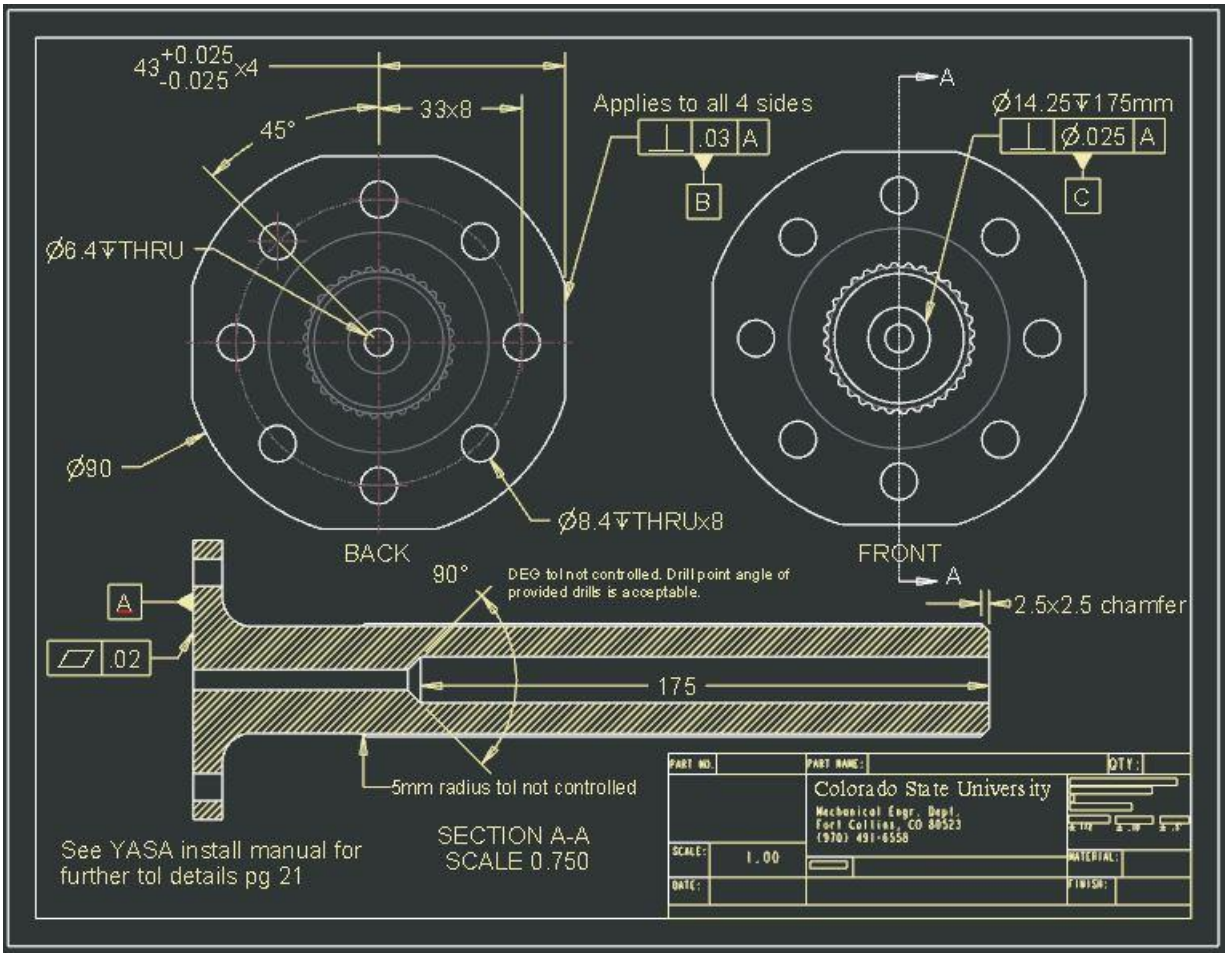

Figure 19: Part G drawing

After heat treatment of a 3.75" round raw stock, the stock was loaded into the CNC and turned down to final dimensions. Using a bullnose endmill the straight side fillet root splines were cut, indexing the fourth axis of the CNC 11.25˚ after each pass, Figure 20. Once the splines were cut, the center supporting the end of the shaft was removed and gun drill bits were used to drill the axial holes. Wandering of the drill did occur given the length of the hole, and as such, the length of the M6 clearance hole was drilled from the flange side. The wandering was not so great as to negatively affect the balance of the shaft (which is also constrained radially by the YASA) or the insertion of the ratchet extensions required to tighten the M6 retainment screw. The final manufactured part is shown in Figure 21.

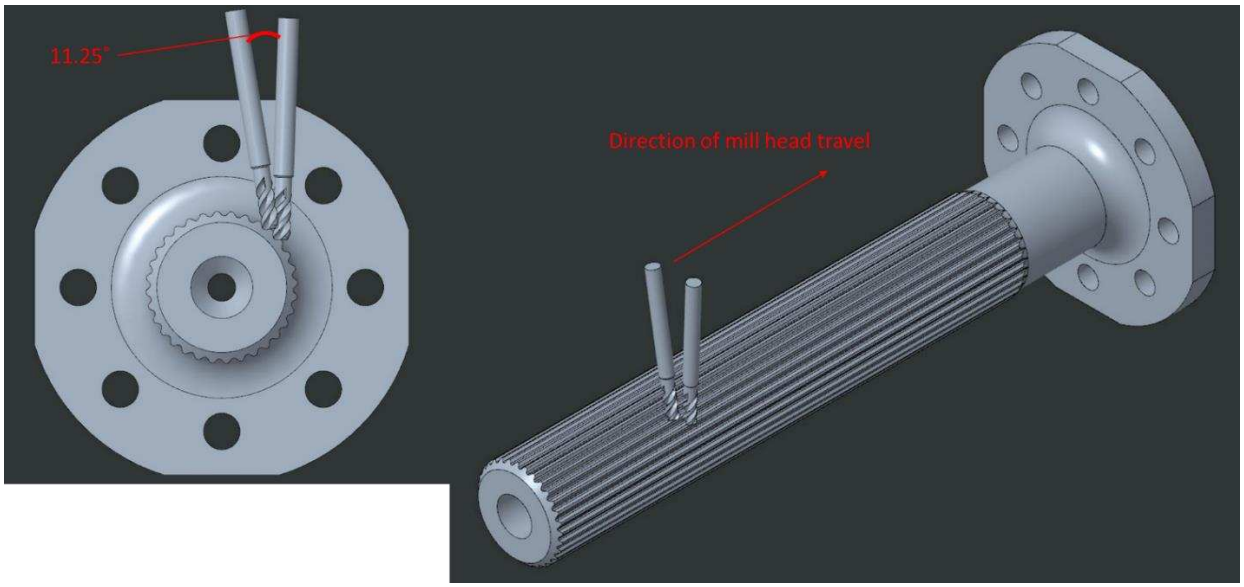

Figure 20: Part G external spline manufacturing method on 4-axis CNC mill

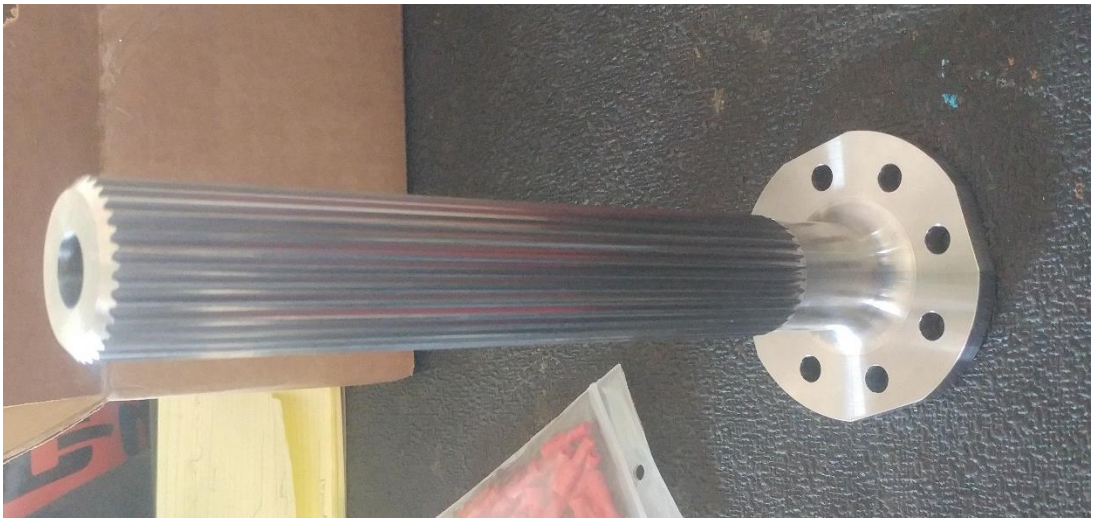

Figure 21: Manufactured Part G

2.1.5 Part L

As seen in Figure 2, Part L or the "custom slip yoke" was designed to mate with Part G, connecting the driveshaft components discussed so far to the propulsion shaft. Part L is made of two primary components, one being the yoke ears, which are an off-the-shelf component that fits the propulsion shaft universal bearing, and the second a 130 mm long tube with internal splines that mate to

Part G. This part was designed to match dimensions of the original stock slip yoke, hence the 130 mm internal spline length, off the shelf yoke ears, and chromium-molybdenum (chromoly) alloy steel.

The greatest challenge of this part was the manufacture of the internal splines. Often, internal splines are created by broaching, however it can be very expensive to have a custom broach made for a single manufactured part. Also, trying to find a local machine shop that had the necessary equipment to broach splines in a 130 mm long piece was nearly impossible. One manufacturer claimed to not know anyone in the state of Colorado with the machine to do it. Regardless, a second, less common method used to create internal splines is wire electronic discharge manufacturing (WEDM). This was the method selected as it was relatively low cost (under $2000), the spline length had no effect on the manufacturing process, tolerance accuracy is high [24], and it could be performed after the work piece was heat treated. The one downside to WEDM is that it takes a relatively long time to perform (8 hours in this case). Alfred Manufacturing Co, Inc. was employed to manufacture this part as they possessed the WEDM capabilities required.

To assemble the yoke ears and tube, the yoke ears first had a 50 mm hole turned down its center axis. The tube was then machined close to final dimensions and with an axial hole slightly smaller than the minor diameter of the final internal splines turned down the center. This was done to promote surface hardening of the future teeth surfaces during heat treatment. Similarly to the donut and tailstock subassembly, the yoke ears were shrunk-fit onto the tube to align the parts and provide resistance to torsion. In this instance however, the subsequent triple pass fillet weld joining the two was designed to carry the torsional loads (using the same design procedure in equation (13)). Distinctive Welding was again employed to perform this weld, as special welding materials are needed for chromoly welding. To align the parts axially during the shrink fit, a pipe was machined to size and used as a shoulder to rest the yoke ears on until they shrank, Figure 22. Once the yoke ears and tube were assembled and heat treated, the part was sent to Alfred Manufacturing to have the internal splines machined via WEDM.

Figure 22: Part L pre-heat treat assembly and manufacture

2.2 Heat Treatment

To meet the strength requirements discussed in the previous section, heat treatment of the powertrain components was performed. This was done using an electronically powered, temperature-controlled kiln, located in the Powerhouse Engines Lab, Figure 23.

Figure 23: Heat treatment kiln

Since stock components with detailed features (splines, threads, chamfers, etc.) needed to be heat treated, it was important to mitigate the formation of iron oxides, commonly called mill scale or simply scale, that begin to form around 700˚C [25]. This was done by continually purging the kiln with nitrogen (N_2) during the heat-treating process, which was required as the kiln is not air-tight, Figure 24. Before beginning a heat treat, the kiln was first purged at a high flow rate for 3 minutes then the flow rate was reduced to a low setting on the flow meter (approximately 10 cc/min). This proved to work well as the flow rate was low enough to not affect the temperature inside kiln during heat treat processes and high enough to prevent ingress of large amounts of oxygen. Figure 25 is a qualitative example of the amount of scale formed on two test pieces and Part L using this process (test pieces were sanded prior to the test until the surface was silver in appearance and free of any debris). The scaling shown amounts to mostly a discoloration, very little scale fell or could be chipped off. Compare to Figure 13, in which the nitrogen ran out during the normalization of Part E, resulting in thick scale formation over the entire surface. Scale was removed from this part by soaking in muriatic acid for 5 hours. Another method employed was to

wrap the parts in stainless steel foil and purge the foil with nitrogen before placing in the kiln. This method worked marginally well, as some pieces showed less scaling than those that were unwrapped, whereas others did not.

Figure 24: Nitrogen purging of kiln setup

Figure 25: Scaling present on test pieces and Part L after heat treatment in nitrogen purged kiln

Note that while the purging gas used was nitrogen, nitride surface hardening does not occur in this setup. Gaseous nitride case hardening usually requires ammonia gas (NH_3) at temperatures up to 530°C [26]. At these temperatures, dissociation occurs resulting in atomic nitrogen that diffuses into the part surface, increasing surface hardness (typically greater than 67 HRC) [27]. For the temperatures encountered in the heat treat processes (maximum 732˚C, ~1350˚F) nitrogen disassociation does not measurably occur [28].

2.2.1 Part G

The material selected for Part G was 17-4 precipitate hardened (PH) stainless steel (aka SAE Type 630 stainless steel) for its high strength properties and relatively simple heat treatment. Evidently, the increase in strength is due to precipitate hardening, a strengthening process by which a uniform dispersion of precipitates forms in the softer surrounding parent material [29]. In 17-4 PH, the precipitate is copper in the body-centered cubic or face-centered cubic, depending on the aging process used [30]. 17-4 PH comes in several heat-treated conditions summarized in Table 2.

Table 2: Heat treatment conditions for 17-4 precipitate hardened stainless steel [31] [32]

Condition	Hardening Temp and Time (air cooled)	Hardness (Rockwell C)	Tensile Strength (MPa) [UTS,YS]
A	Annealed	36 35	1100 [1103,793]
H900	482°C (900°F), 1 hour	44 45	1310 [1379,1275]
H925	496°C (925°F), 4 hours	42 43	1170-1320 [1310,1207]
H1025	552°C (1025°F), 4 hours	38 38	1070-1220 [1172,1138]
H1075	580°C (1075°F), 4 hours	36 37	1000-1150 [1138,1103]
H1100	593°C (1100°F), 4 hours	35	970-1120
H1150	621°C (1150°F), 4 hours	33 33	930-1080 [1034,896]
H1550M	760°C (1400°F), 2 hours followed by 621°C (1150°F), 4 hours	31	[945,765]

The condition selected for Part G was H925 as it provided the highest strength for a 4-hour heating period. The raw stock was 3.75” in diameter and 16” long so a long heating period was used to ensure the core of the material fully reached the heating temperature and had adequate time to heat soak.

Heat treating procedure:

1. Set raw material in kiln and purge with nitrogen for 3 minutes.
2. Reduce nitrogen flow rate to 10 cc/min (or if no flow meter is available, set the flow rate so the nitrogen coming out of the tube is barely perceptible to the touch).
3. Linearly ramp kiln temperature to 925°F over 1 hour.
4. Hold at 925°F for 4 hours.
5. Remove from kiln and let cool in still, room temperature air.
6. Machine after heat treatment. This is done for two reasons:
    a. The hardness of H925 is not so hard as to be unmachinable (~39-40 HRC), and the annealed state can be “gummy” when machined.

b. Heat treating post-machining can result it warping even at the relatively low temperatures in the ~900°F range, especially for the long, slender part considered here.

2.2.2 Part E and L

Part E and L required a more complex heat treatment as they are made from 4140 and 4340 chromoly alloy steel. First, it was necessary to determine that the stock components were indeed chromoly (there are many types of chromoly steel, however the following discussion focuses on 4140 and 4340 and these are by far the most common in automotive applications). Two methods were considered for this, one being a spectral analysis of a stock part sample to determine the exact chemical composition and the second a spark test. Note that the only way to guarantee correct material identification is to perform a spectral analysis. That being said, the second method was chosen as it is significantly faster, cheaper, and there was a very high probability that the stock components were made of chromoly steel [33] [34] [35]. To perform a spark test, a sample is taken to a grinding wheel and images are taken of the sparks produced. The color and pattern of the sparks can broadly inform on the chemical makeup of the sample, Figures 26-28 [36] [37] [38]. Since the spark test can be somewhat subjective, multiple references have been included. The spark test of the stock part sample is shown in Figure 29.

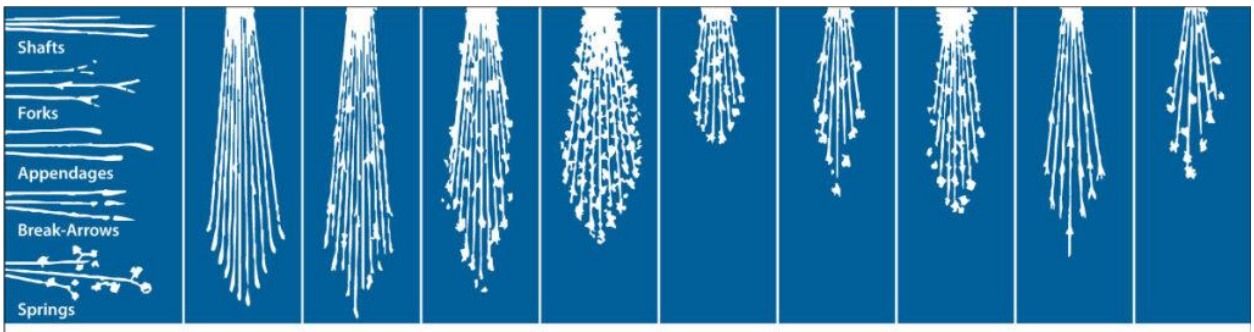

CHARACTERISTICS OF SPARK TEST	LOW C. STEEL (0.1%C)	MILD STEEL (0.25%C)	MED C. STEEL (0.4%C)	HIGH C. STEEL (0.7%C)	GREY CAST IRON	MALLEABLE CAST IRON	AUSTENITIC MANG. STEEL	HIGH ALLOY STEELS 18/18 STAIN	DIE STEEL
Volume of Stream	Large	Large	Large	Med. Large	Small	Moderate	Mod. Large	Moderate	Small
Relative Length	1.6m	1.8m	1.6m	1.4m	0.6m	0.75m	1.1m	1.3m	0.9m
Color at Wheel	Straw	White	White	White	Red	Straw	White	Straw	Red
Color at end	Straw-white	White	White	White	Straw	Straw	White	White	
DESCRIPTION OF SPARK STREAM (COMPARE WITH KNOWN SAMPLES)	As carbon increases in iron, spark changes form long straw shafts with appendages to forked shafts and some springs, number of springs increasing with carbon content.			Mass of small fine repeating springs.	Many small repeating springs.	Long shaft than grey iron, small repeating springs.	Many fine repeating springs.	Alloys reduce spark length of comparable carbon steel.	

Figure 26: Spark formation of various steels and iron [36]

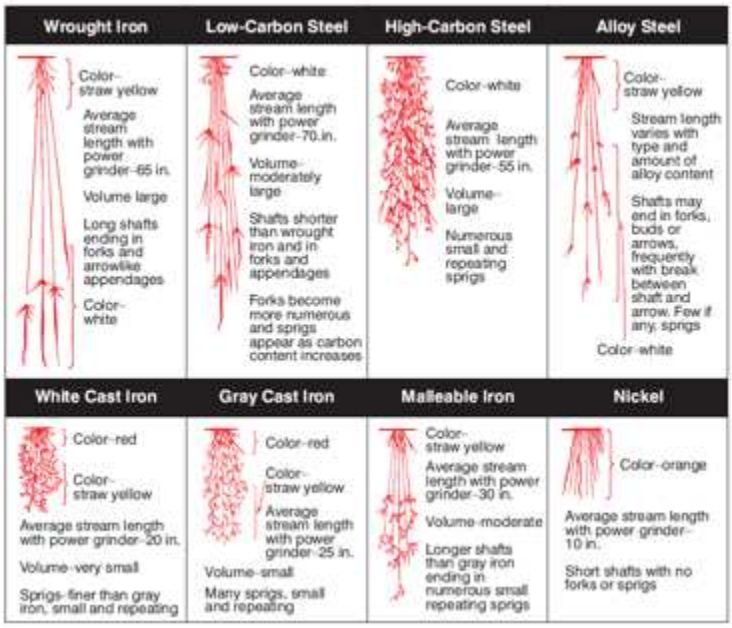

Figure 27: Spark formation of various steels and iron [37]

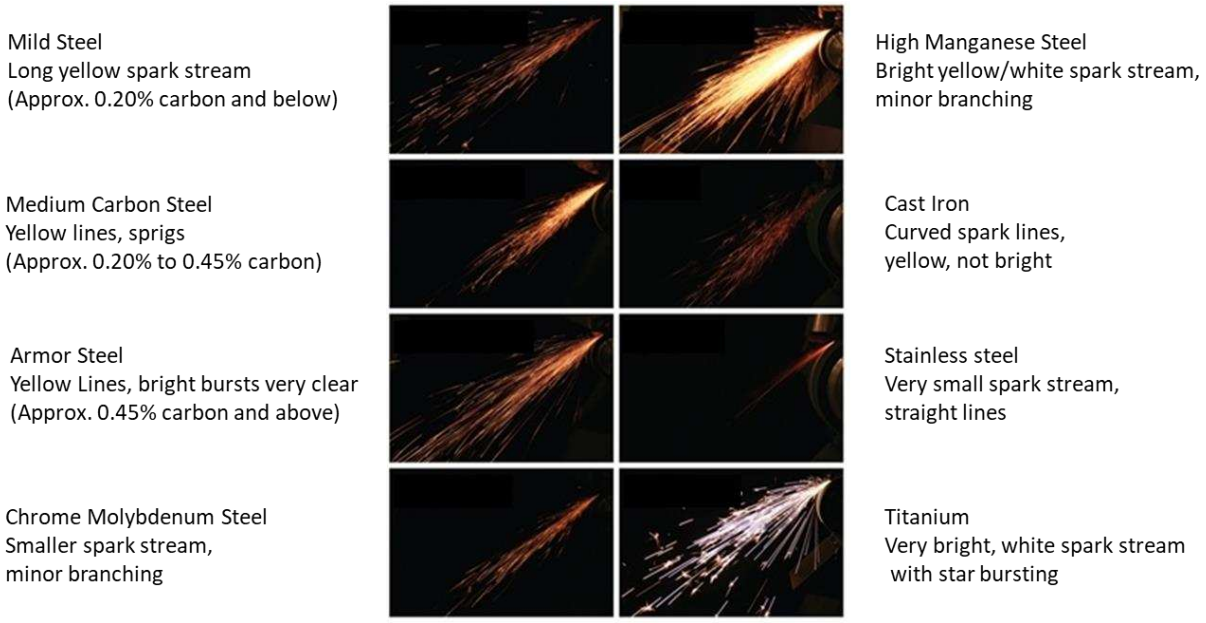

Figure 28: Spark formation of various steels and iron, modified from [39]

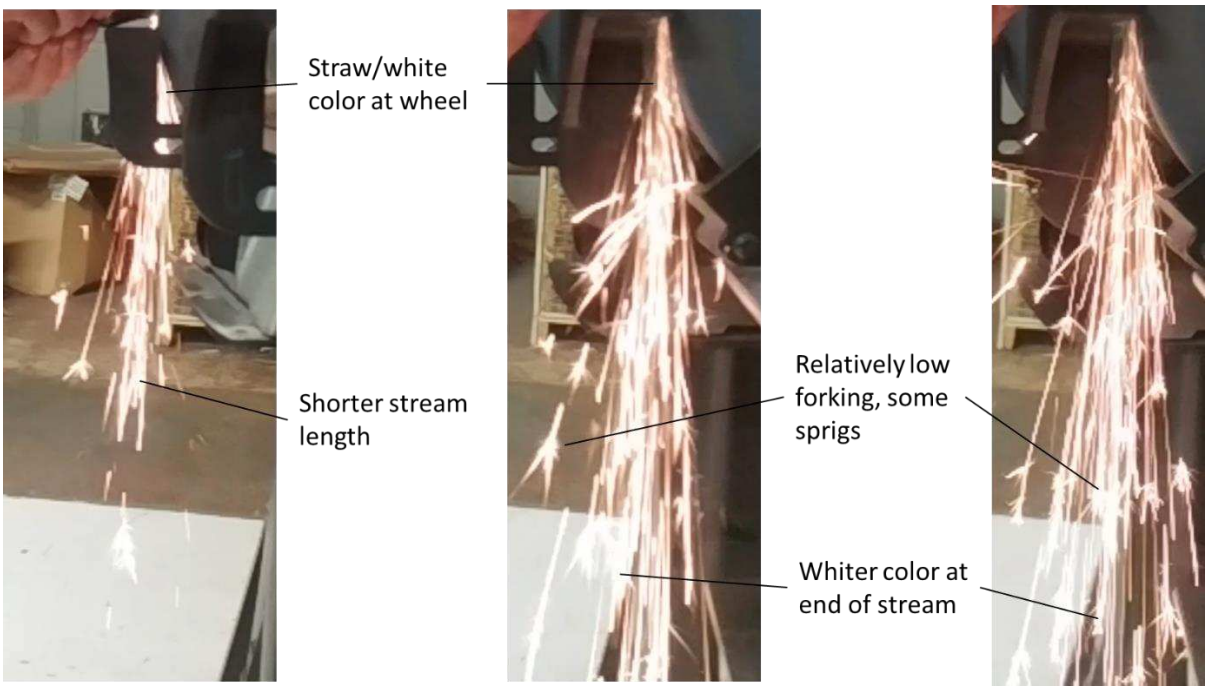

Figure 29: Spark formation of TVP stock section of Part E and L

From the collection of references above, the test sample, and the fact that many automotive drivetrain components are made of 4140/4340 alloy steel, there was enough confidence to weld the stock

components to the custom machined components discussed in previous sections. Since the components were successfully welded together, confidence was further increased that stock components were 4140 or 4340. The following discussion will be based on the materials being 4140 and 4340. It then needed to be determined the weldability of the two materials to each other (note that the process for welding 4140 or 4340 to itself is the same as both use the ER80S-D2 filler rod). The materials are very similar in their chemical compositions, Table 3.

Table 3: Element content in 4140 and 4340 chromoly steels

Element	4140	4340
Carbon, C	0.380 - 0.430 %	0.370 - 0.430 %
Chromium, Cr	0.80 - 1.10 %	0.700 - 0.900 %
Iron, Fe	96.785 - 97.77 %	95.195 - 96.33 %
Manganese, Mn	0.75 - 1.0 %	0.600 - 0.800 %
Molybdenum, Mo	0.15 - 0.25 %	0.200 - 0.300 %
Phosphorous, P	≤ 0.035 %	0.0350 %
Silicon, Si	0.15 - 0.30 %	0.150 - 0.300 %
Nickel, Ni	N/A	1.65 - 2.00 %
Sulfur, S	≤ 0.040 %	0.0400 %

From Table 3, it is seen that the largest difference between the two materials is the addition of Nickel in 4340 which helps improve hardenability, corrosion resistance, strength in high temperature applications, ductility, and fatigue resistance [38] [40]. Determining the weldability of these two components together is a difficult question to answer without performing a detailed study on welded samples. However, the welding of stainless steels to 4340 has been studied in academia with results indicating moderate strength limited by the weaker material is achievable [41]. Also, in the off-roading community welding 4140 to 4340 has been successfully performed in the construction of suspension systems. Based on this evidence, welding the two parts together was considered reasonable. In general, these chromoly alloys can be difficult to weld as they suffer from heat stress cracking and as such, Distinctive Welding, Inc. was employed to perform the welding process on both Part E and L [42].

To perform the heat-treat of Parts E and L, the same kiln setup described for the heat treatment of Part G was used. Several issues need to be addressed in the heat treatment process.

1. Part E and L were comprised of stock components that were already in a heat-treated condition, custom components in an annealed condition, and heat affected zones.
2. Detailed features were present in Part E and L including splines, threads, clearance holes, chamfers, etc. whose dimensions could be altered during heat treatment.
3. Heat treatment required immediate tempering in the same kiln used to austenitize the steel. This meant that the kiln had to quickly cool from roughly 1600˚F to 900˚F while the parts were being quenched.

The first issue was addressed by normalizing the components before heat treatment. Normalizing is similar to annealing except the part is allowed to cool from the austenitic range in room-temperature air instead of slowly in the kiln. This more rapid cooling results in fine pearlite production [29]. While either annealing or normalizing would be acceptable to eliminate pre-existing heat-treated conditions, cold working, and residual stresses, normalizing was chosen as it was a faster process and required less N_2.

The second issue can only be realistically addressed experimentally. Given the nature of the TVP project, this was not an option, so instead industry advice was sought. To this end, in interviewing Brian Masterson, Sr. Mechanical Engineer at Tri-Continental Corp. with over 30 years' experience in designing parts, assemblies, and specifying materials and their heat treatments with fifteen US patents in the biomedical, petrochemical, locomotive, and fluidics industries [43], he advised that while chromoly steels tend to shrink dimensionally when going from annealed/normalized to heat treated conditions, given the relative size of Parts E and L the amount of shrinkage will likely be small enough that tolerances built into the part design should still allow for successful assembly post-heat treat. If not, final machining can be performed on some features like holes and threads to ensure assembly. For the internal splines, Part L was a nonissue as they would be manufactured post-heat treat, but for Part E Mr. Masterson advised that since the splines are part of the stock component in a heat-treated condition, normalization followed by heat treatment would theoretically cause a net expansion and contraction of zero; it was reasonable then to perform the processes and let tolerances protect against slight deviations in original part form.

To address the third issue, practice heat treatments were performed on small chromoly samples to predict how quickly the kiln would cool down from austenitizing to tempering temperatures and the associated temperature dynamics. The process is as follows:

1. Bring the kiln up to 1650˚F and hold for 15 minutes (note this is with N_2 purging the kiln).
2. Open the kiln, leaving lid open, remove and quench samples. While quenching, monitor the temperature gage on the kiln until it reaches tempering temperature. When it does, close the lid (note that kiln is programmed to hold tempering temperature after 15 minutes at 1650˚F).
3. Once samples are hand warm, place back in the kiln. Use the flow meter on the N_2 supply to adjust the flow rate of N_2 if necessary.

The qualitative results of this process were:

- With the kiln lid open, the temperature readout dropped to tempering temperature in approximately 3-5 minutes. The test samples, which were approximately half the size of Part E and L took much longer than this to reach hand warm temperatures (roughly 100-150˚F) in one gallon of quench oil.
- Upon closing the lid, the thermal mass of the kiln caused the temperature readout to rise approximately 200˚F above the tempering temperature (at which the kiln was programmed to hold at). This temperature could be quickly brought down by increasing the flow of N_2 into the kiln, however it was necessary to put obstacles in front of the gas entry port to keep fresh N2 from directly contacting the test samples and to promote turbulence.
- Once the temperature was brought down, the N_2 flow could be reduced back to roughly 10 cc/min, however slight adjustments were required for approximately 10 minutes to maintain temperatures to +/-5˚F of the tempering temperature. This was possible by hand due to the slow system dynamics.

The justification for the heat treatment process for 4140 and 4340 is now presented. Note that given the similarities of the two materials previously discussed, the heat treatment process will be the same. Referencing the eutectic diagram for carbon steels, Figure 30, we see that 4140/4340 chromoly steels (0.38%-0.43% carbon) fall in the hypoeutectoid part of the diagram (carbon content below 0.76%). As such, these metal alloys need to be heated to approximately 900˚C (1652˚F) for normalization and hardening heat treatment processes to ensure phase transformation to austinite.

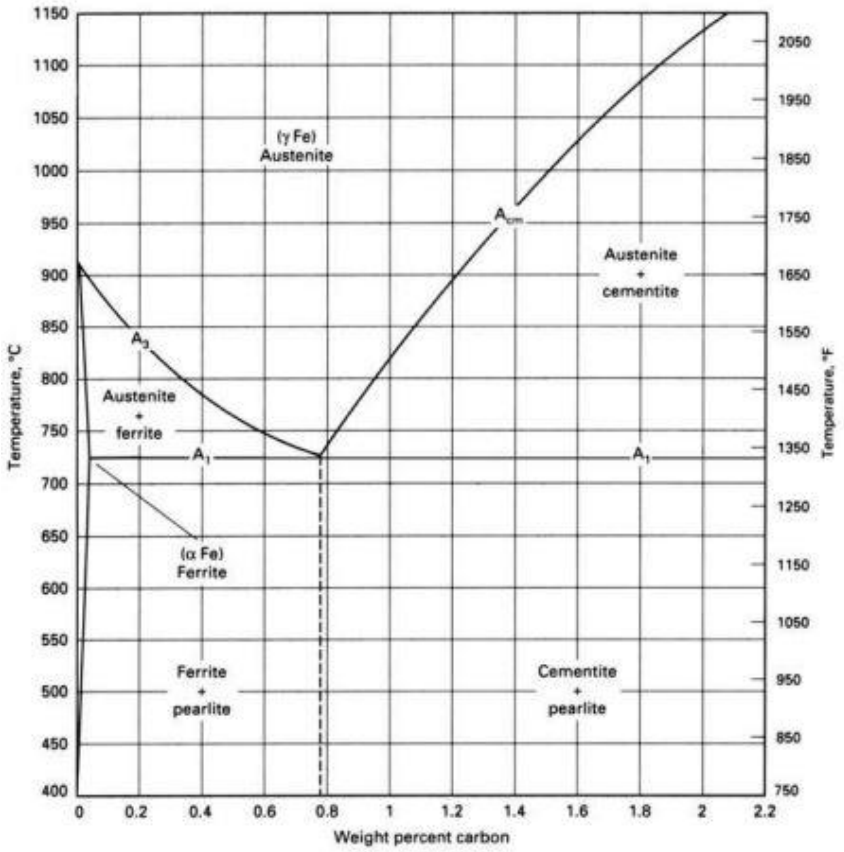

Figure 30: Eutectic equilibrium phase diagram for steel [44]

For the quenching process, quench oil was used. Oil has a quenching rate of roughly 45˚C/s when the part is agitated [29] and as can be seen from the continuous cooling transformation (CCT) diagram for 4340, this results in the formation of primarily martensite in the alloy, Figure 31.

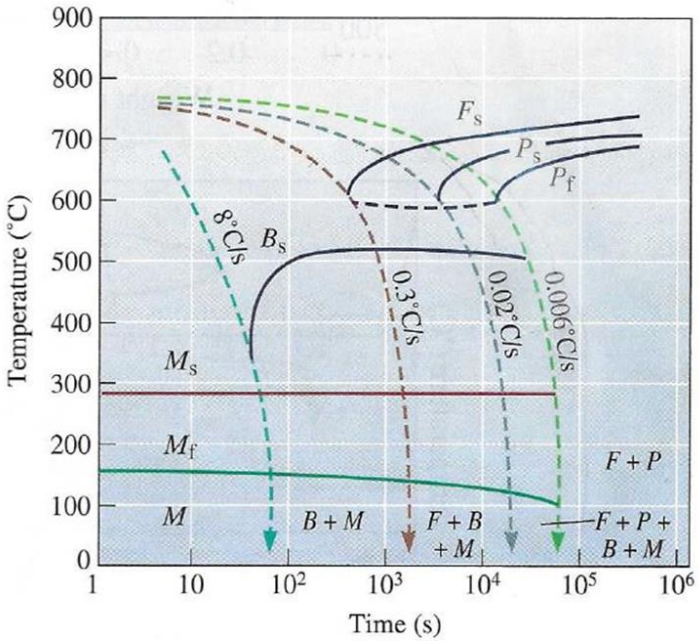

Figure 31: CCT diagram for 4340 [29]

For the tempering process, many steel manufacturers provide tempering diagrams for their products, Figure 32, and these were used to select the tempering temperature. The goal is to temper at the lowest temperature possible to achieve the highest ultimate tensile strength.

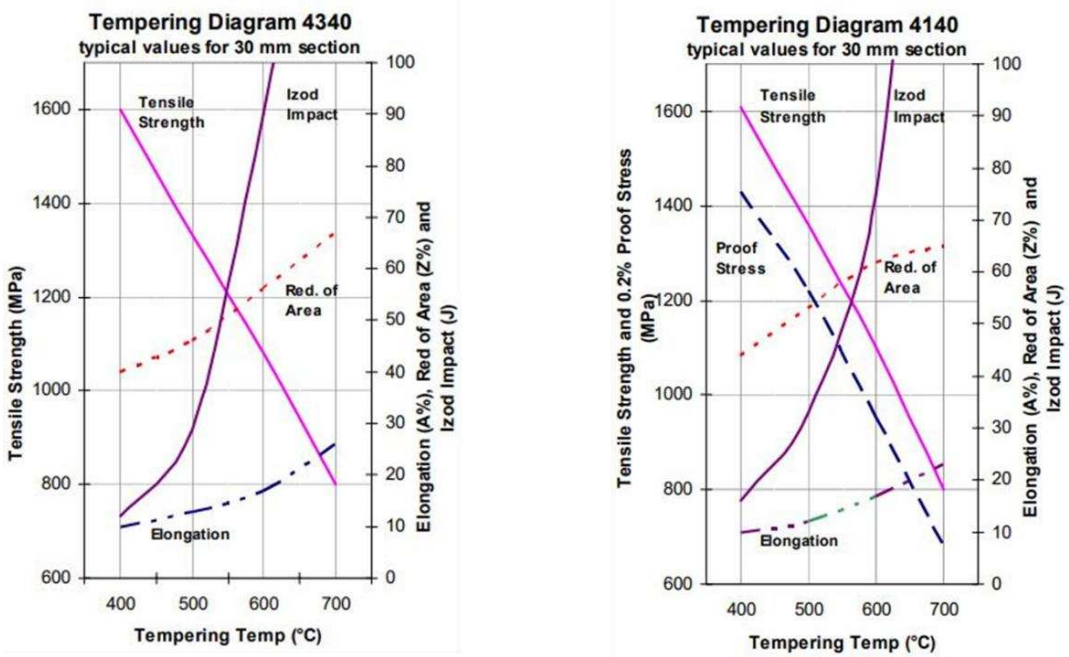

Figure 32: Tempering diagrams for 4340 and 4140 [45] [46]

It is important to note that while lower tempering temperatures result in a harder, stronger material, it also results in one that is more brittle. Chromoly steels also exhibit a unique tempering phenomenon called tempered martensite embrittlement (TME) in which the material suffers significant embrittlement in certain tempering ranges [47]. This is characterized by a "trough" in the toughness vs tempering plot, Figure 33.

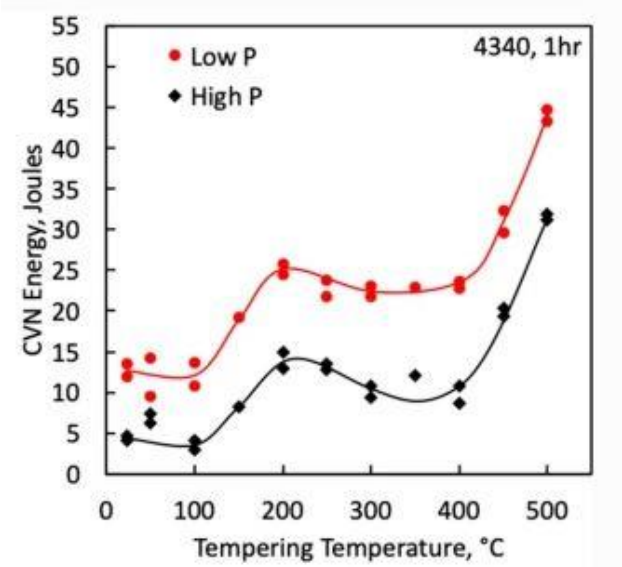

Figure 33: Impact energy of 0.003 wt pct (Low P) and 0.03 wt pct (High P) 4340 steels [47]

For 4340, this range is from about 200 to 400˚C and for 4140 the upper bound is slightly lower, around 370˚C. Since Part E and L can contain 4340, the lower limit for tempering is 480˚C, where 80˚C has been conservatively added as other sources have reported TME occurring around 420-430˚C. Now that the austenitizing temperature, quenchant, and tempering temperatures have been selected, the heat treatment steps are listed.

4140/4340 Normalization:

1. Purge the kiln with N_2 for 3 minutes. Then reduce the N_2 flow to 10 cc/min.
2. Place components in kiln and linearly ramp temperature to 1650˚F over 1.5 hours.
3. Hold at 1650˚F for 30 minutes.

4. Remove from kiln and let air cool.

4140/4340 Hardening:

1. Purge the kiln with N_2 for 3 minutes. Then reduce the N_2 flow to 10 cc/min.
2. Place components in kiln and linearly ramp temperature to 1650˚F over 1.5 hours.
3. Hold at 1650˚F for 30 minutes.
4. Remove from kiln, leaving kiln lid open, and immediately quench in oil. Continuously agitate the part. For larger parts, a 5-gallon bucket of oil is recommended, otherwise the oil will heat up significantly and it will take more time for the parts to reach hand warm temperatures (~150˚F).
5. While quenching, program kiln to 900˚F. When kiln reaches this temperature, close the lid.
6. Once parts are hand warm, place back in kiln and temper for 1 hour per inch of thickness (of thickest part section).
7. Adjust the flow rate of N_2 until the temperature of the kiln stabilizes.
8. After tempering, remove from kiln and let air cool.

2.2.4 Heat Treatment Test Data

After heat treating Parts G, E, and L the surface hardness of the parts were tested to gauge the success of the heat-treating processes. Tests were performed using files of known hardness. If the file could scratch the surface, the material is softer than the file, if it cannot scratch the surface then the material is harder than the file. The files ranged in hardness from 40 RHC to 65 HRC. This method was selected as it ~10x more economical than standard penetrator-based hardness tests and can be performed on the part itself, whereas other methods generally require a heat-treated sample. However, it is less accurate and at best has an uncertainty of +/- 2.5 HRC. The results are summarized in Table 4.

Table 4: File hardness testing data of Part G, E, and L

File Hardness (HRC)	Part G-Scratched?	Part E-Scratched? [Flange, Tube]		Part L-Scratched? [Tube, Yoke ears]	
40	No	Slightly	Slightly	Yes	Yes
45	Yes	Yes	Yes	Yes	Yes
50	Yes	Yes	Yes	Yes	Yes
55	Yes	Yes	Yes	Yes	Yes
60	Yes	Yes	Yes	Yes	Yes
65	Yes	Yes	Yes	Yes	Yes
Expected UTS (MPa)	~1200-1310	~1250-1350	~1300+	~1175-1300	~1250-1350

From the results in Table 4, it is seen that Part G has a Rockwell C hardness somewhere between 40-45, Part E ≤40, and the splines and yoke ears of Part L <40. These results seem to concur with data from several manufacturers which state that 17-4 PH in H925 condition will have a hardness of 40-43 HRC, 4140 tempered at 900˚F a hardness of 36-39 HRC, and 4340 tempered at 900˚F a hardness of 38-40 HRC [48] [31] [49]. A lower hardness range testing kit was not available to find the lower bound of the components. For application in the TVP, such a file test is satisfactory, however for a more critical application or production quality parts, a hardness testing machine and sample pieces would be required.

2.3 Powertrain Assembly

To assemble and install the powertrain into the TVP, modifications of the vehicle body were required. For the dinnerplate and EM to fit, the transmission tunnel was expanded by hammering out the stamped body frame, Figure 34. The transmission with the subassembly of Parts A, D, and I was then installed into the vehicle.

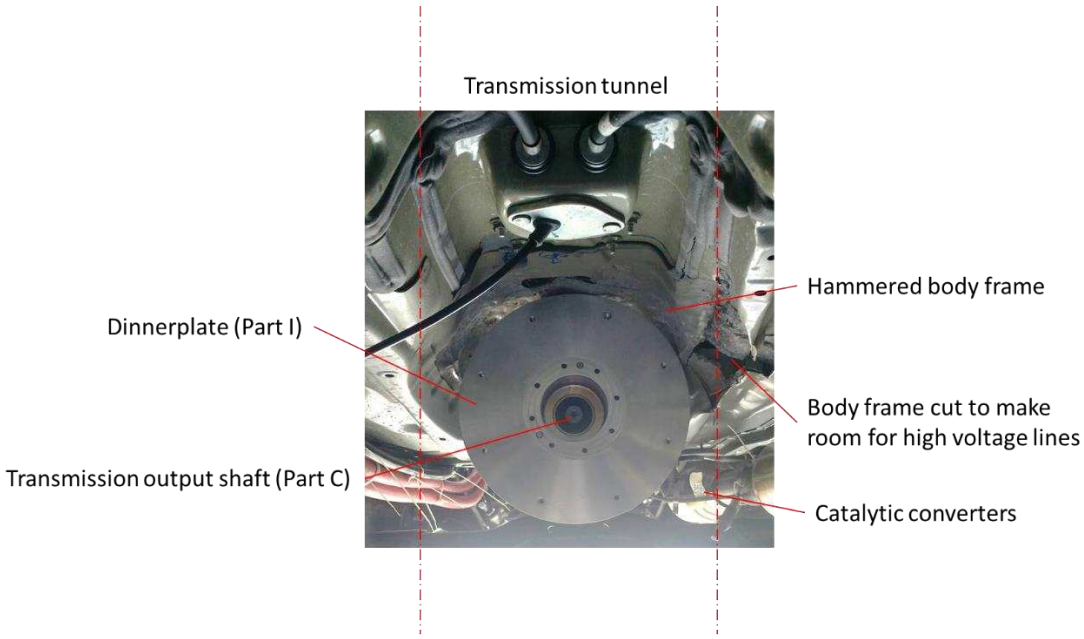

Figure 34: Assembly of powertrain stack into TVP

To install the rest of the powertrain, Parts E and G were assembled with the YASA, then this subassembly was bolted onto the dinnerplate. Parts E and G were assembled by placing both components into a machinist's vice that had parallels on the jaw faces and base. With the vice clamped down, the subassembly was constrained on three of the four alignment faces (see Figure 19). The M8x1.25 Class 12.9 socket cap head screws were then torqued to 41 Nm in a star pattern. The subassembly of Parts E and G was then inserted into the female splines of the YASA, Figure 35. Given the class 6 tolerance fit, the subassembly had to be tapped in with a rubber mallet. Care was taken not to insert the splines of Part G too far, or else the ends of the male splines would lock up on the YASA female splines (~20 mm gap ensures this does not occur).

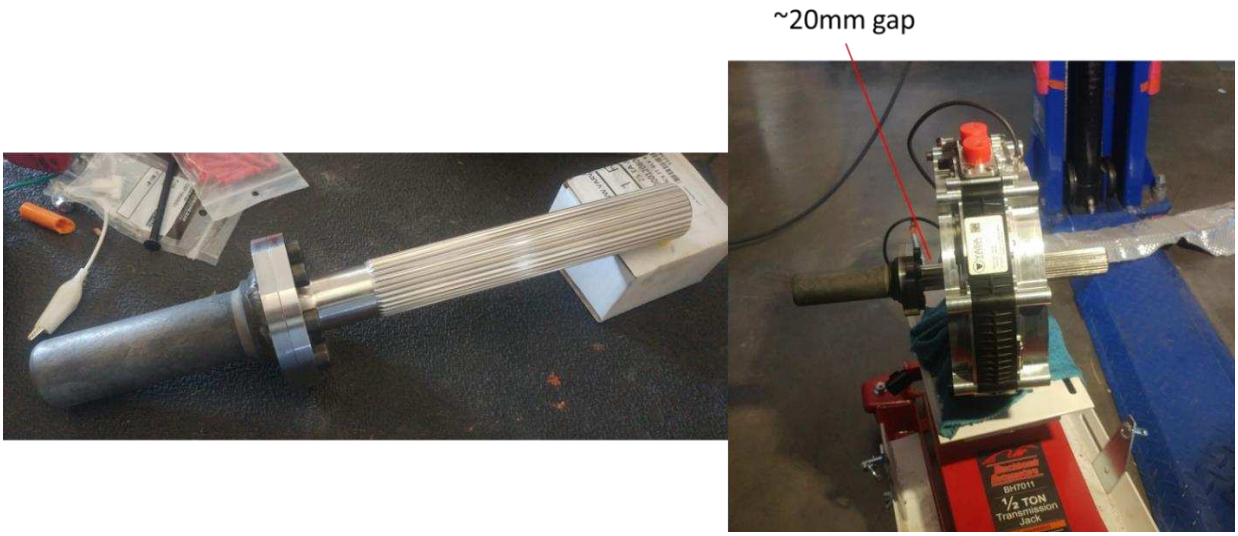

Figure 35: Assembly of Part E, G, H, and YASA

To install the subassembly shown above, a large hole was cut in the body frame directly below the PRNDL. This was done to make clearances for assembly and dynamic movement, as well as for the coolant and electrical ports at the top of the YASA (red caps in the above figure). This hole was then covered with an acrylic sheet and the PRNDL mounted on top, Figure 36.

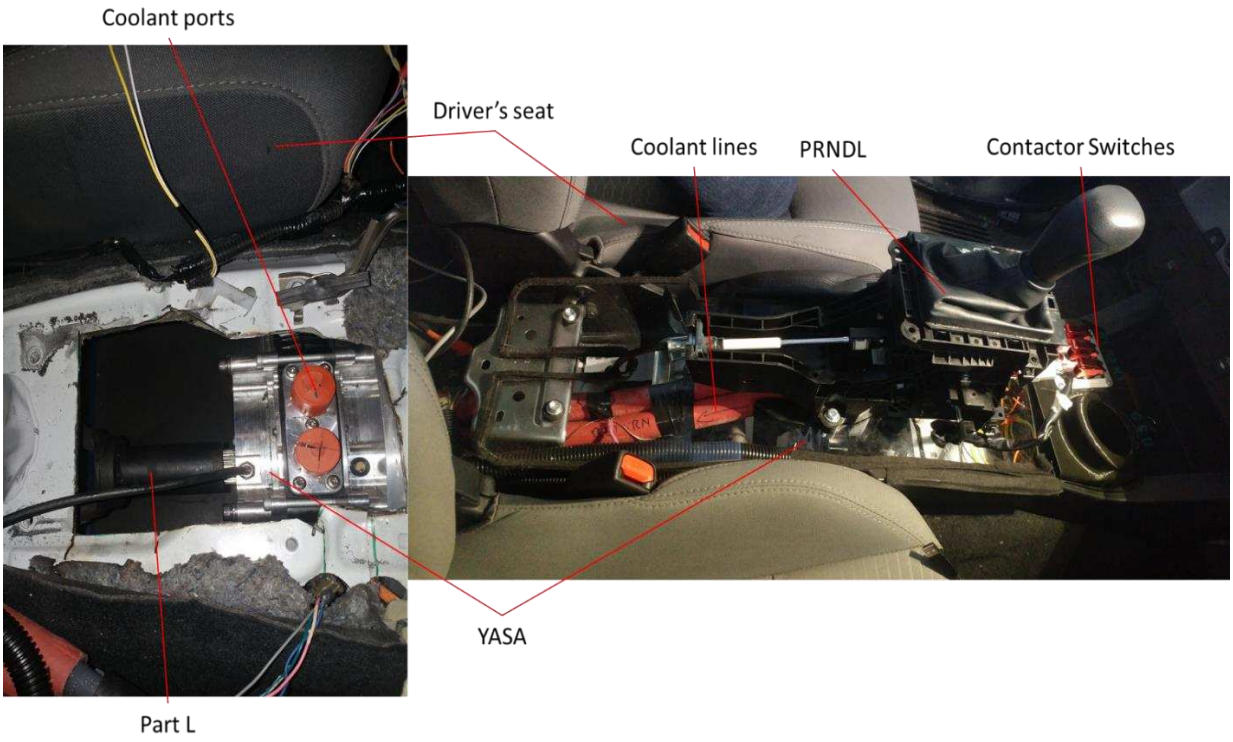

Figure 36: Body and PRNDL modifications

The installation was performed by lifting the YASA on a transmission jack until the tube of Part E cleared the lower edge of the pocket formed by Part I and D. The motor was then slid toward the vehicle front and lifted further until the male splines of the transmission output shaft (Part C) and the female splines of Part E meshed. Then the YASA was slid forward further until it bottomed out on Part I. The YASA mounting bolts were then installed to hand tightness. In the current arrangement described, the inner flange face of Part E is not flush with the end of the transmission output shaft (see Figure 2), so a mallet was used to tap the assembly of Part E and G towards vehicle front until E and C were flush. At this point the YASA mounting bolts were torqued to 41 Nm in a star pattern (except the lower two, as these are 18-8 stainless steel-15 Nm). The retainment screw (Part J) was then installed and this required two ¼" drive extensions to reach the tapped M6 hole in the end of Part C. Thread locker was used on this screw, however if it ever needs to be removed this can be done by first completely unscrewing it from Part C then using a magnet grabber or by putting pipe thread tape on the drill bit so the bit fits snugly into the screw head, pulling it out when the extensions are removed.

To support the cantilever forces experienced by the YASA, supporting brackets were installed that connect the soft mount of the transmission crossmember to the back of the dinnerplate, Figure 37. These brackets were bolted to the soft mount and to the back of the dinnerplate.

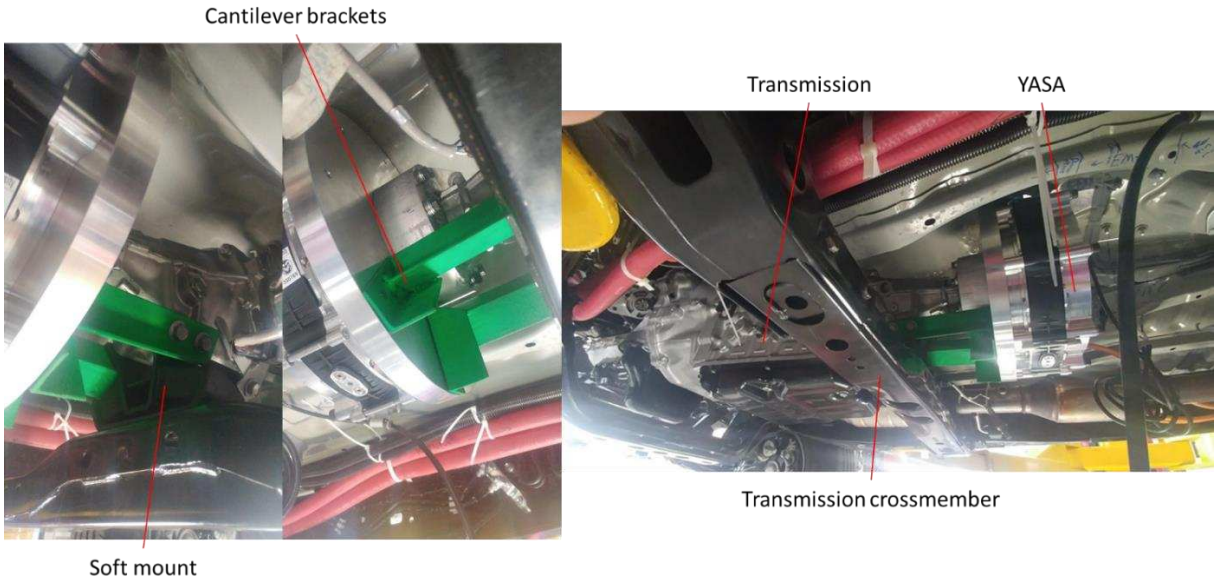

Figure 37: Cantilever support brackets

To complete the drivetrain installation, Part L was assembled to a shorten propulsion shaft and then assembled onto the external splines of Part G, Figure 38. The propulsion shaft shortening and balancing was performed by Northern Colorado Driveline, Inc.

Figure 38: Fully installed powertrain with shortened propulsion shaft

2.4 Powertrain Testing

Due to the prototype nature of the TVP, it was not practical to test each individual part before successful assembly. To test the powertrain, the output shaft of Part G was turned in a series of tests by hand and then the ICE/EM. After each test, the drivetrain components were disassembled and inspected for signs of scraping or accelerated wear (scraping, burrs on spline teeth, metal shavings, etc.). Fasteners were also checked (M8x1.25 on the flange and motor mounts) to ensure they were still properly torqued. During all tests, no excessive forces hindering rotation of the shaft were encountered (demonstrated by the fact that it could be turned it by hand and that the cogging torque of the EM was the largest rotational force encountered) and at higher speeds (up to 30 mph in zero velocity testing on the lift) no perceptible increased power output by the ICE (compared to pre-hybrid drivetrain installation) occurred. The results of this test series are summarized in Table 5.

Table 5: Qualitative system level testing of hybrid powertrain

Test	Component Visual Inspection	Fastener Check	Scraping, bearing humming, or other failure indicative sounds/vibrations?	Notes
Spin output shaft of Part G by hand (no propulsion (prop) shaft)	Passed	Passed	No	
Spin output shaft of Part G via ICE (no prop shaft)	Passed	Passed	No	Only noise encountered was EM electrical whine
Prop shaft installed, spin wheels with ICE on lift	Passed	Passed	No	Heavier engine vibrations when stationary and in drive.
Prop shaft installed, drive vehicle in parking lot via ICE (drivetrain is loaded)	Passed	Passed	No	Vibrations dissipate at speed.
Prop shaft installed, spin wheels on lift with EM	Passed	Passed	No	Whine from EM. This is nominal for the EM.
Spin wheels on lift with both EM and ICE	Passed	Passed	No	Whine from EM.
Drive vehicle at airstrip with both EM and ICE	Passed	Passed	No	Whine from EM, vibrations when stationary and in drive still present, but dissipating.

The results of these tests demonstrated that the TVP powertrain was validated against its design goals and was ready for on-road testing.

Chapter 3: Cooling

3.1 Cooling Loop Requirements and Design

As mentioned above and discussed in [10], the YASA electric motor and Cascadia Motion PM150-SP inverter were selected for the Test Vehicle Platform and both components required liquid cooling. This section will cover the design, construction, and testing of the liquid cooling system in the TVP.

To begin, each of these components had operating specifications from the manufacturer that drove the design requirements and constraints, Table 6.

Table 6: Cooling system design requirements [14] [50]

Requirement/Constraint	YASA	PM150-SP
Max Inlet Pressure (kPa)	100	450
Fluid Flow (LPM)	12*	8-12
Max Temperature (˚C)	90 (<65 ideal)	80, de-rates at 100
Heat Dissipation (kW)	4**	N/A
Fluid Type	Non-Conductive Dielectric Oil***	Anti-Freeze-(50/50 Water/Ethylene Glycol)
Pump Voltage (V)	12	12
Coolant filtration (µm)	150	N/A

*Manufacturer suggested, dependent on application
**Typical heat dissipation capacity of cooling system when running at continuous rated power
***SHELL TELLUS S4 ME 46

With the above constraints in mind, the cooling system developed consisted of an oil coolant loop that dissipates heat from the EM through a liquid-to-liquid plate heat exchanger (L2LPHE) to an anti-freeze loop that dissipates heat from the inverter (INV) and L2LPHE to a radiator located at the front of the vehicle. This construction was selected as there was only room for one radiator without significant modifications. Also, given the nature of the EM usage described in [7], the duty cycle of the EM would be relatively low compared to its continuous power output. A diagram of the designed cooling system in shown in Figure 39.

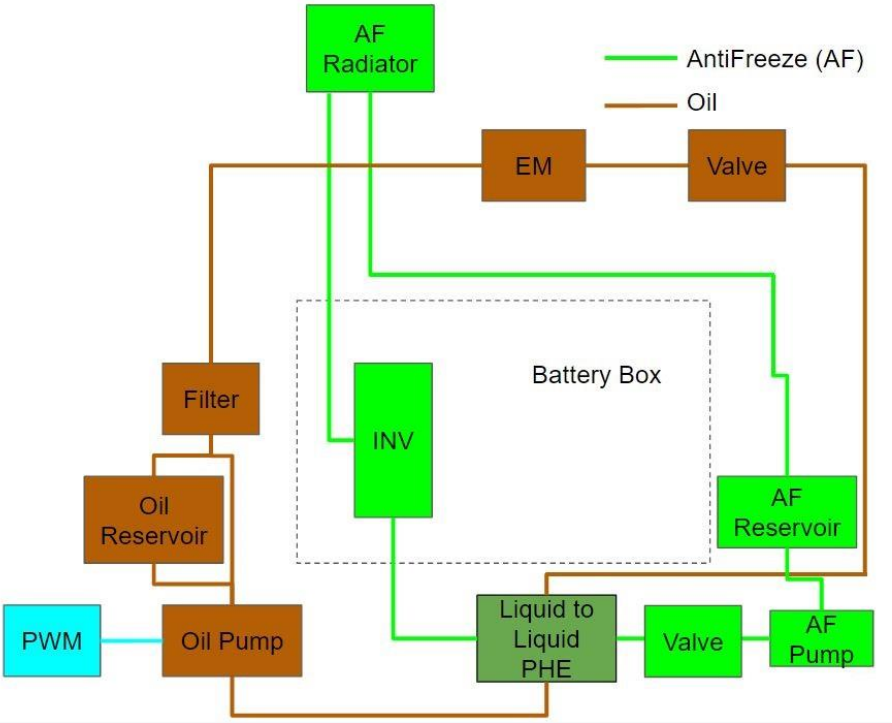

Figure 39: Cooling loop system diagram

Note that both systems contain a coolant reservoir that allows for expansion and contraction of the operating fluid without causing increases in fluid pressure. The system is designed to have atmospheric pressure at the pump inlets; thus, reservoirs are used instead of expansion tanks. Expansion tanks are used in pressurized coolant systems.

For the pumps, the EMP WP29 and the EngineGear GP-612L were selected as they are both 12V pumps that are capable of flow and pressure specifications shown in Table 6. As seen in the above diagram, the GP-612L was powered with a PWM speed controller to accurately control the inlet pressure at the EM. The L2LPHE selected is the McMaster-Carr 35115K61, as it is compact, has a cooling capacity of 20.22 kW, and flow capacity of 26.5 LPM. The radiator came off a previous CSU electric drivetrain test bench where it was used to cool a Cascadia Motion PM100 inverter. The filter is a Fleetguard LF16035 Oil Filter and can filter particles down to 30 µm at 100% efficiency with a flow rate of 33 LPM [51].

On a test bench, the pumps' respective performance with the INV and EM was characterized to ensure they would meet the design requirements. It was found the EMP pump had an outlet pressure of 21 psig and flow rate of 13.67 LPM and the GP-612L, 25 psig at a flow rate of 10.67 LPM. Note that this outlet pressure is the result of speed controlling the GP-612L to ensure ≤100 kPa (14 psig) inlet pressure at the EM. With the pumps characterized and using the part data discussed above, a quasi-equilibrium simulation was performed to predict the steady-state operating temperatures of the system before installing into the TVP.

3.2 Cooling Loop Modeling

Purpose: To determine the steady-state operating temperature of both working fluids at the inlet and outlet of cooled components for different air velocities through the radiator. With said temperatures known, the air velocity required to keep all components (EM and Inverter) within operating temperatures can be determined.

Method: Temperature calculations will be based on the ε-NTU method for counterflow heat exchangers [52] [53]. Starting from an initial condition, the model iterates until a steady-state temperature is reached. The model does not consider dynamic heat transfer, i.e., each iteration in simulation is considered to be in quasi-equilibrium. The electric motor operating conditions correspond to a worst-case situation in which the motor is running constantly at peak continuous power. Fluid flow rates are 13.67 LPM and 10.67 LPM for the AF and oil loops, respectively.

Assumptions:

- Worst-case EM heat production at continuous power is 4kW (from YASA datasheet).
- All EM heat produced is transferred to the oil coolant.
- The radiator is considered to be a counterflow heat exchanger.
- Effectiveness (ε) is assumed to be 0.85 for the radiator.
- No heat is lost or gained through tubing between system components.

- Inverter is assumed 90% efficient. For a 150kW inverter, 15kW of waste heat is produced.
- All inverter waste heat is transferred to the AF loop.
- Fluids in the L2LPHE are in the laminar regime.
- Specific heats are assumed constant.
- No heat is rejected to the environment by the L2LPHE.
- Working fluid properties are constant.
- Heat addition from pumps is negligible.
- Ambient air is assumed to be 25°C.

Results: Simulation results are plotted in Figure 40 through Figure 43. Steady-state values are compared to system constraints in Table 7.

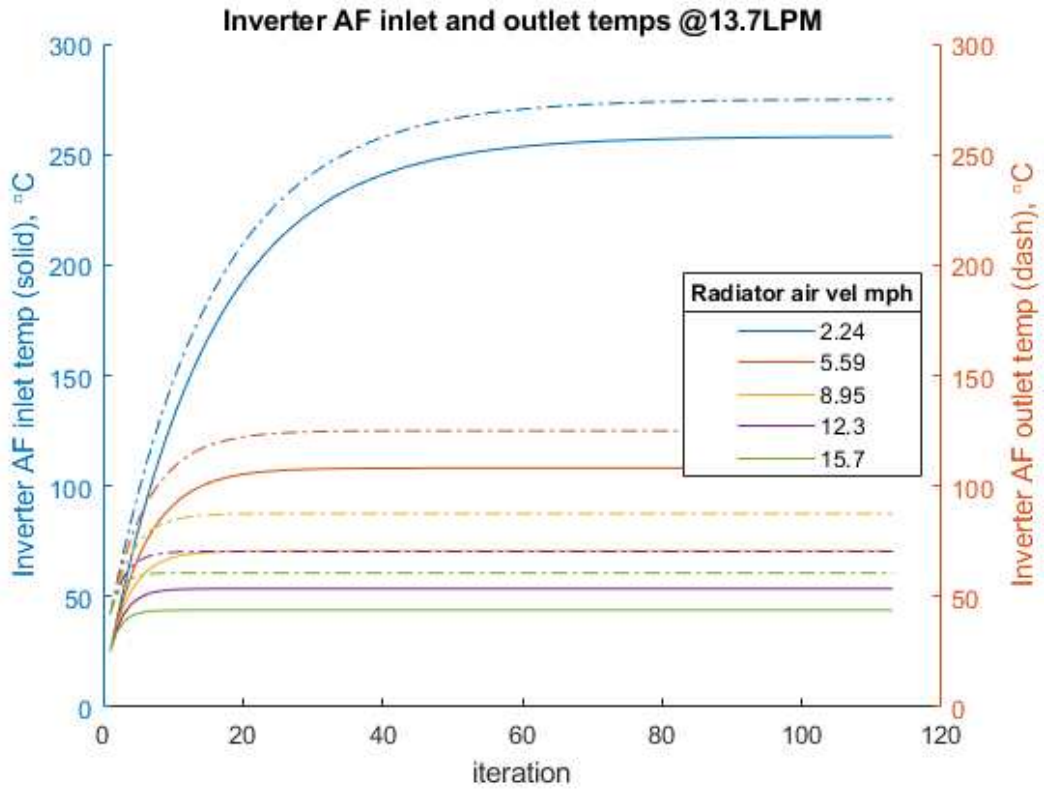

Figure 40: Anti-freeze Inverter inlet and outlet temperatures

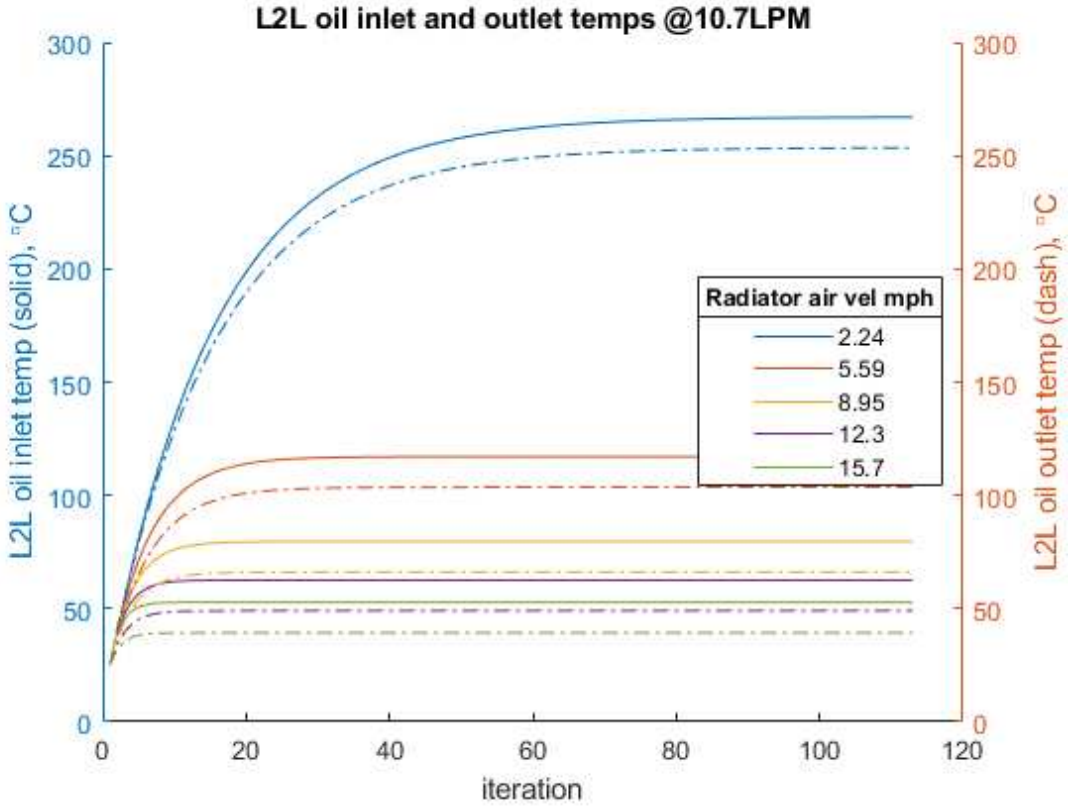

Figure 41: Oil L2LPHE inlet and outlet temperatures

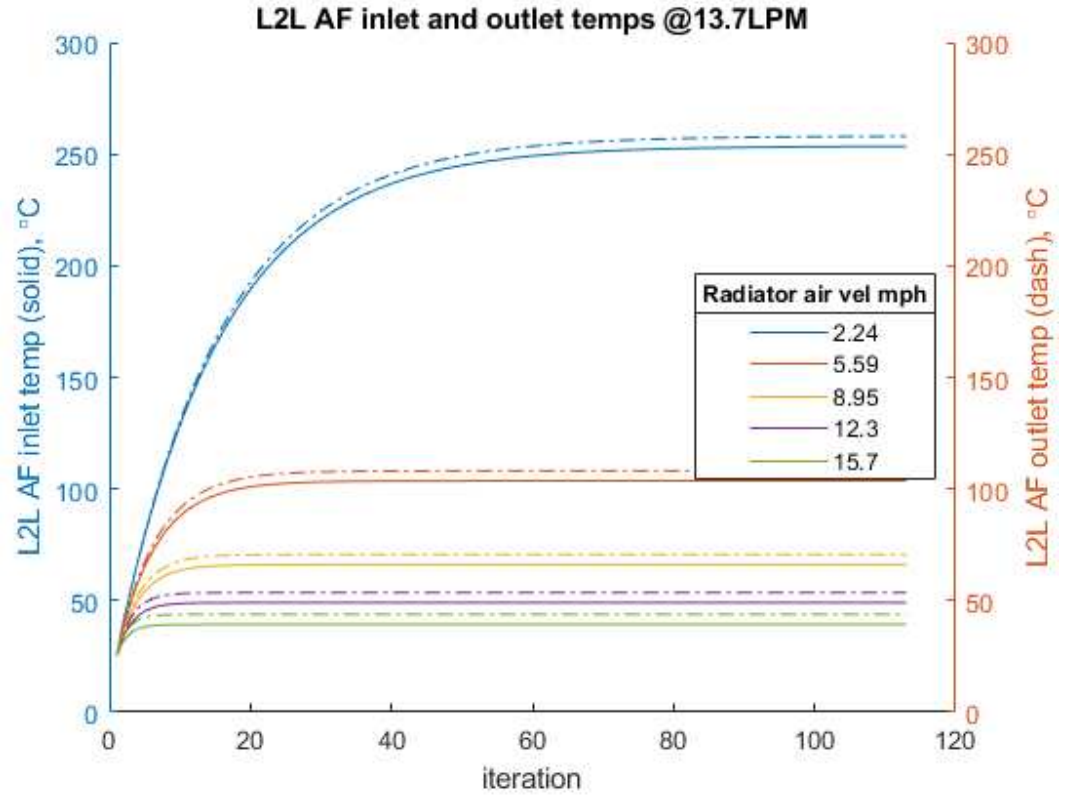

Figure 42: Anti-freeze L2LPHE inlet and outlet temperatures

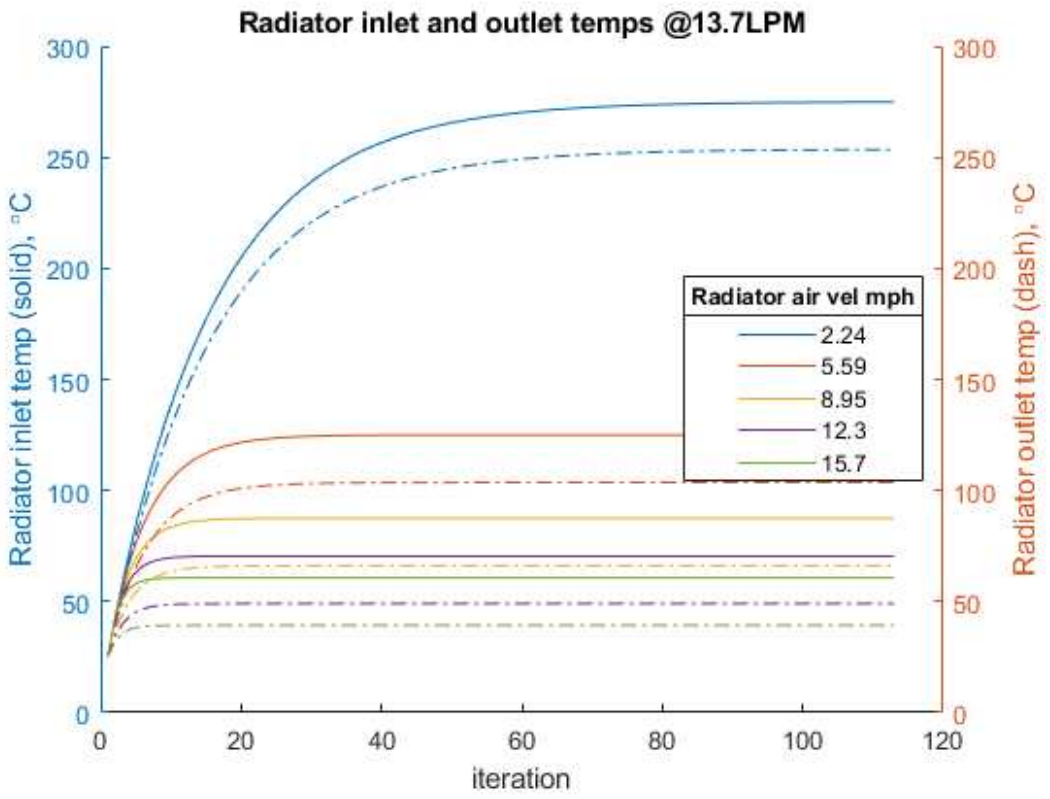

Figure 43: Anti-freeze radiator inlet and outlet temperatures

Table 7: Summary of coolant loop modeling steady-state temperatures at 9 mph airspeed

Component	Steady-state inlet °C	Steady-state outlet °C	Max allowed °C
Radiator (AF)	87.5	66.1	N/A
INV (inverter) (AF)	70.6	87.5	80.0
L2LPHE (AF)	66.1	70.6	176.7
L2LPHE (oil)	79.61	66.1	176.7
EM (oil)	66.1	79.61	90

From Table 7, it is seen that the air velocity of approximately 9 mph through the radiator is not sufficient for all components to stay within allowable operating temperatures. Analyzing the above figures, the minimum allowable air velocity is roughly 12 mph. Given that the usage of the EM is certainly lower in PAE implementation, it is expected that the steady-state operating temperatures will be significantly lower. To increase airflow at low vehicle speeds, a fan was installed on the radiator.

3.3 Coolant Loop Construction, Functional Testing, Drive Cycle Testing and Model Validation

3.3.1 Construction

To construct the cooling loops in the TVP, components were mounted in their respective locations shown in Figure 44. Placement of the pumps, reservoirs, L2LPHE, and tubing was determined primarily based off packaging constraints and ease of installation. One-inch ID heater hose tubing capable of 100˚ C and 200 psig operating conditions was used in the anti-freeze loop and the same tubing with ¾" ID was used for the oil loop. Schedule 40 tube fittings with the same operating specifications were used. In several locations, pressure gages and calibratable, turbine-type flow meters were installed for system testing and monitoring. Waste gate valves were also installed for manual control of loop pressure and flow rate if needed.

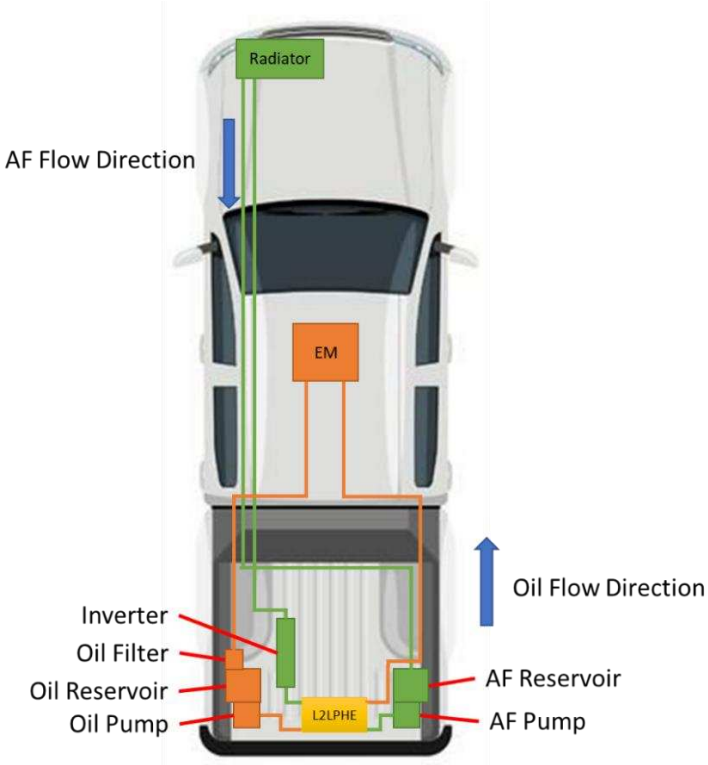

Figure 44: Coolant loop layout in TVP

3.3.2 Functional Testing

Upon constructing the coolant loops into the TVP, functional testing was performed. For the AF loop, a flow rate of 13-14 LPM was achieved, shown in Figure 45, and for the oil loop 10-11 LPM, shown in Figure 46. In Figure 46, it is also seen that slightly less than 14 psig is achieved.

Figure 45: Tested anti-freeze flow rate, LPM

Figure 46: Tested oil flow rate, LPM

It is worth noting that in the functional testing of the oil loop, it was discovered that the non-conductive oil coolant caused significant electrostatic buildup on the tubing due to frictional forces between the fluid and tubing wall and static arcing was observed between the coolant lines and vehicle chassis. While the safety risk was low given the discharge locations were not near/exposed to combustibles, arcing is a reliability issue and causes electromagnetic interference (EMI). To mitigate this, the rubber tubing of the oil loop was wrapped in bare conductive wire/copper tape and grounded to the chassis, shown in Figure 47. This resulted in near elimination of static discharges.

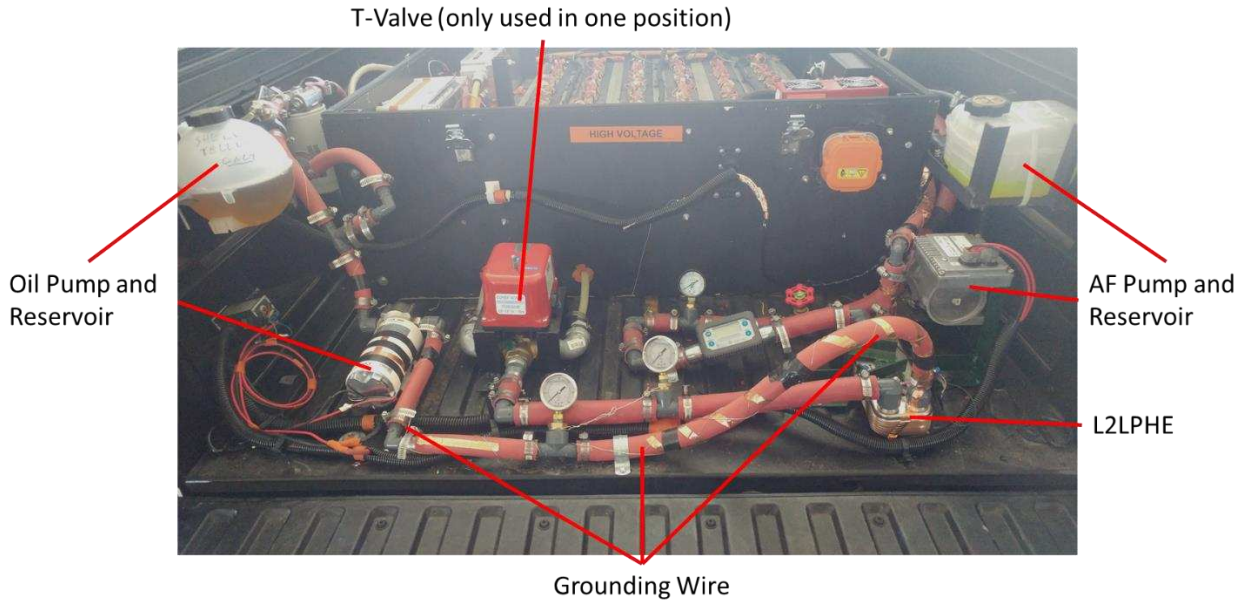

Figure 47: Construction of coolant loops and oil loop grounding wire

3.3.3 Drive Cycle Testing and Model Validation

Cooling loop results for hybrid driving are now presented. The first test consisted of on-road drive cycles with a 60-40 manual torque split between the ICE and the EM, Figure 48. Figure 49 shows the INV and EM temperatures for this drive cycle.

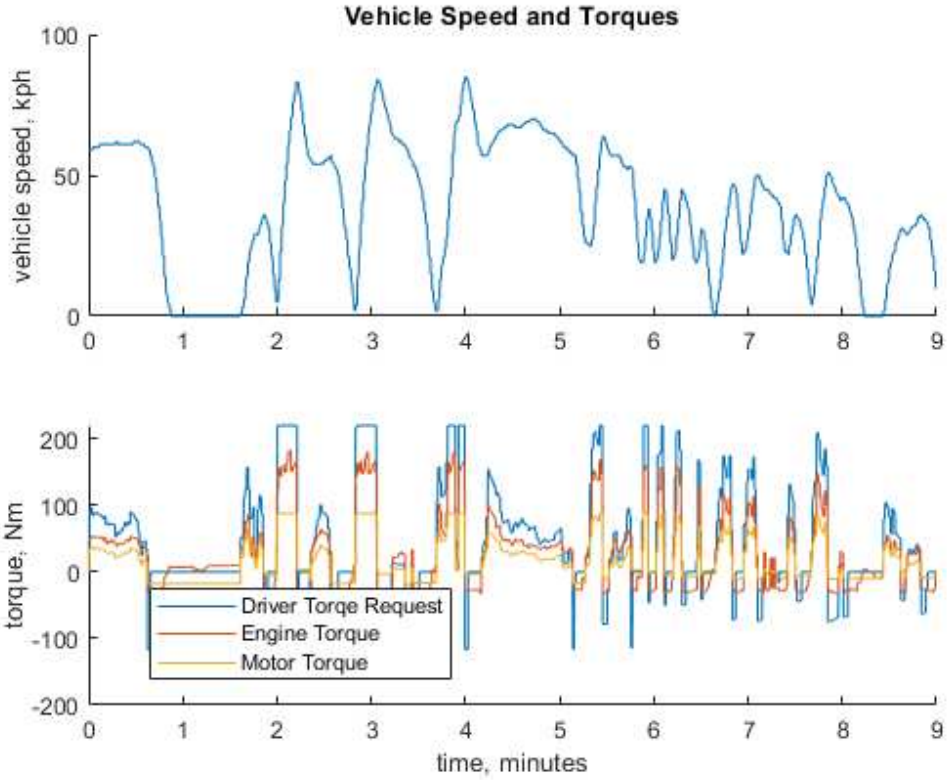

Figure 48: Vehicle speed and torques for 60-40 manual torque split

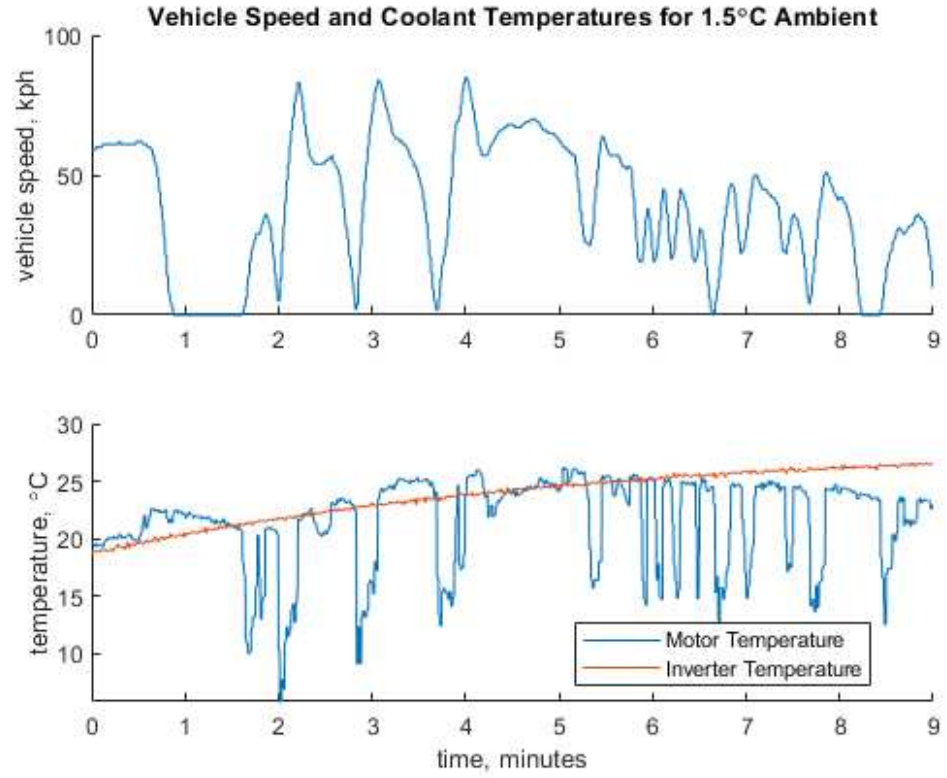

Figure 49: Vehicle speed and temperature data for 60-40 manual torque split

Clearly from the above results, the cooling system is more than satisfactory as both temperatures did not even exceed 30˚C for the drive cycle. Note however that this test was conducted in cold weather at 1.5˚C. This resulted in the coolant flow rates dropping to approximately 12 and 8 LPM for the anti-freeze and oil loops, respectively. Updating the model with these numbers (assuming fluid properties remain unchanged), Figures 50 and 51 result.

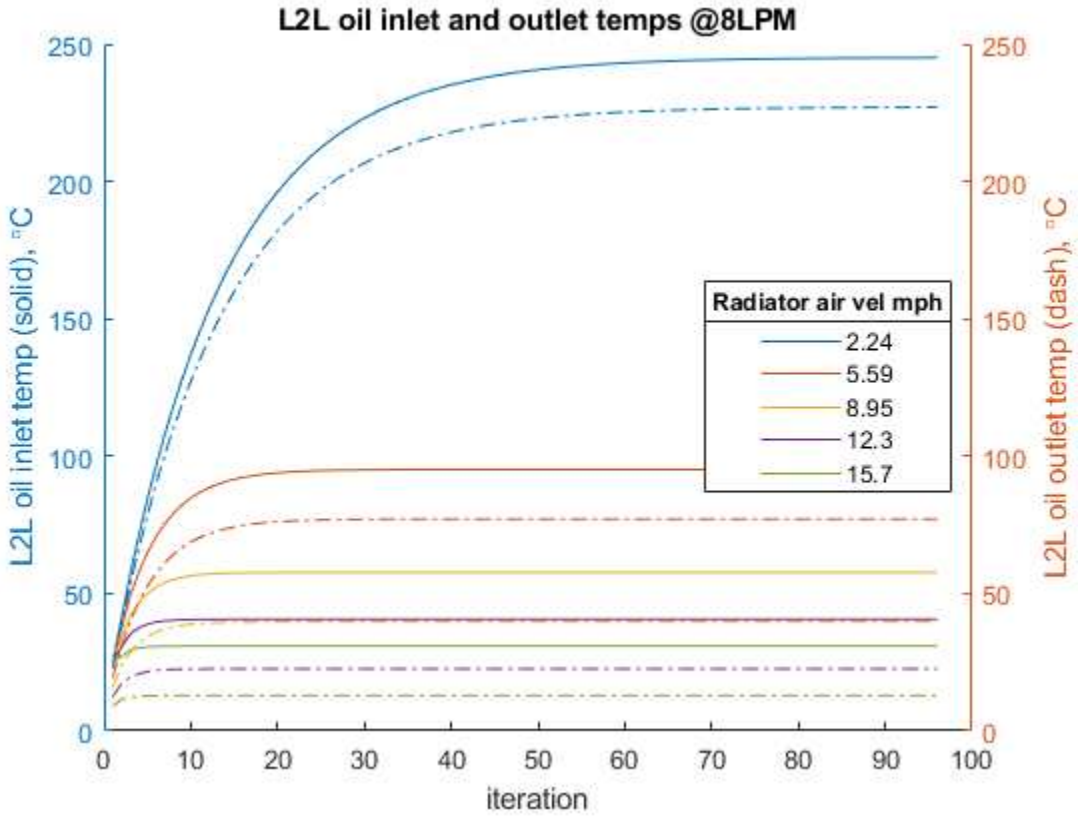

Figure 50: Updated inlet and outlet model temperature for L2LPHE, 60-40 torque split

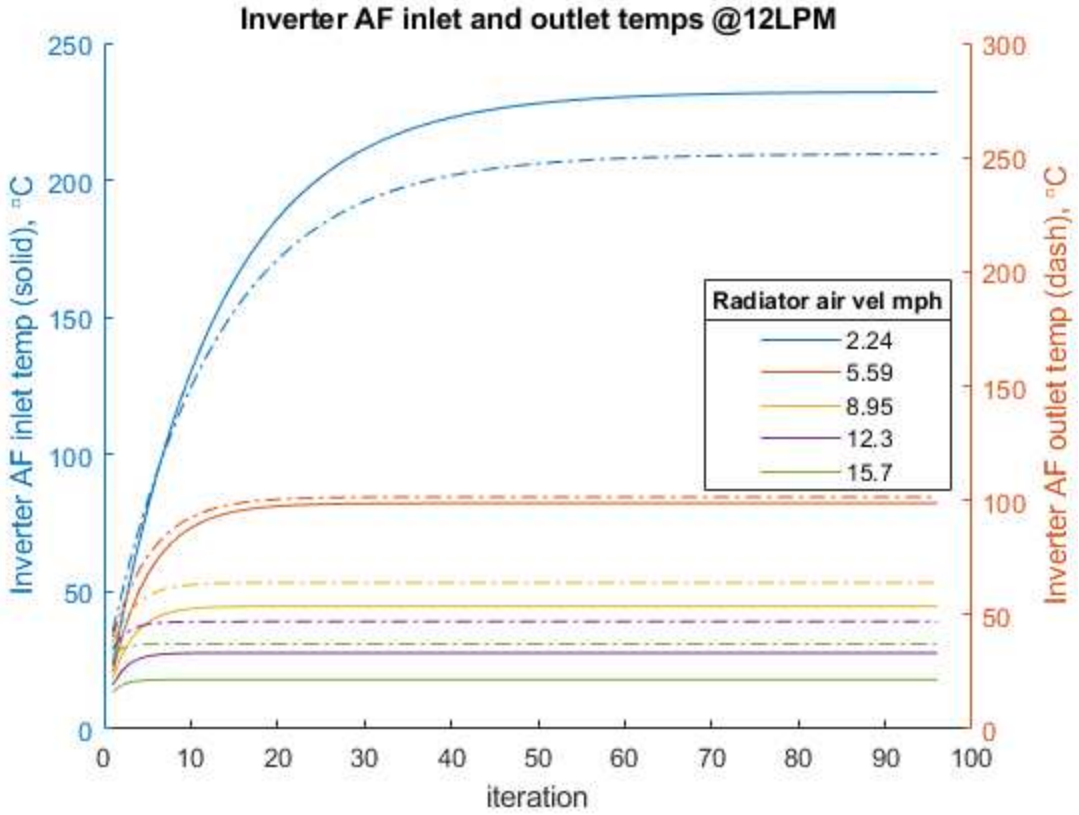

Figure 51: Updated inlet and outlet model temperature for Inverter, 60-40 torque split

Looking at the above figures, we can see that the model is validated against the test data for 60-40 manual torque split. Taking the average of the L2LPHE oil inlet and outlet temperatures (which corresponds to motor outlet and inlet temperatures in the model) the motor temperature is approximated by the model to be 22˚C for an airspeed of 15.7 mph. Doing the same for the Inverter, its temperature is approximated to be 28˚C. The tested EM and INV average temperatures are 21.5˚C and 23.9˚C, respectively. Note that the airspeed in the test data is assumed to be the same as the vehicle speed until the vehicle is traveling below 15 mph. At this point, the radiator fan turns on with an assumed airspeed of 15 mph.

The second test consisted of a ‘baseline’ torque split. In this scheme, the engine is driven at its optimal operating engine speed and torque condition. The residual torque is then made up by the EM. Vehicle speed and torques are shown in Figure 52 and the system temperatures in Figure 53.

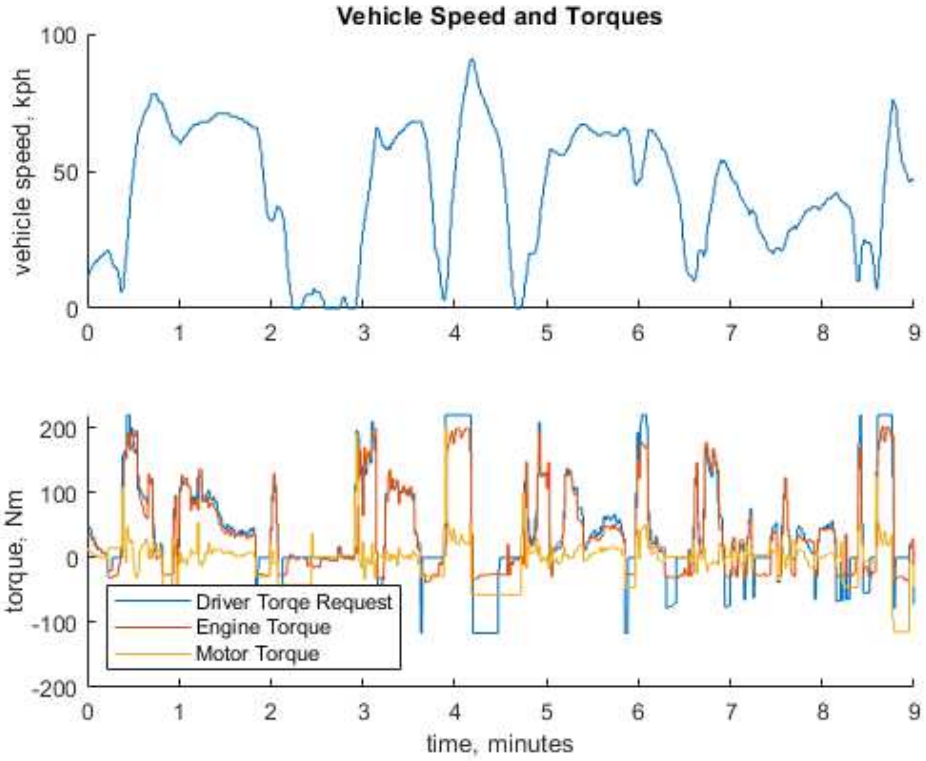

Figure 52: Vehicle speed and torques for baseline torque split

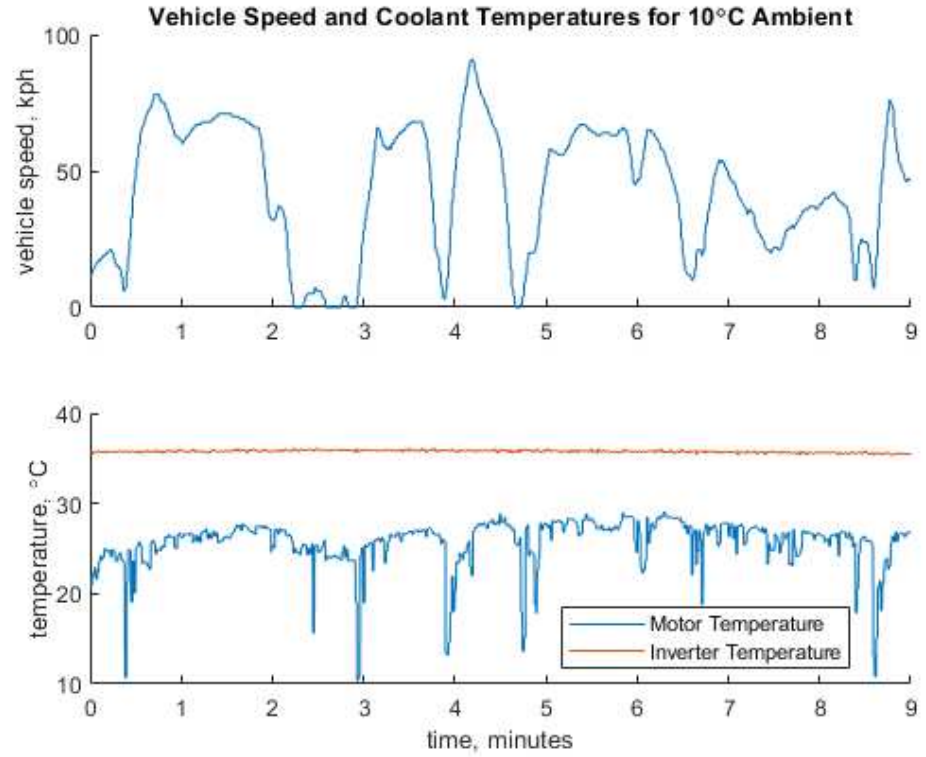

Figure 53: Vehicle speed and temperature data for baseline torque split

From Figure 53 it is seen that the Inverter and EM temperatures are fairly stable during operation for an ambient temperature of 10˚C. It is interesting to note the sudden EM temperature drops occur at the exact same time as sudden increases in EM torque, Figure 54.

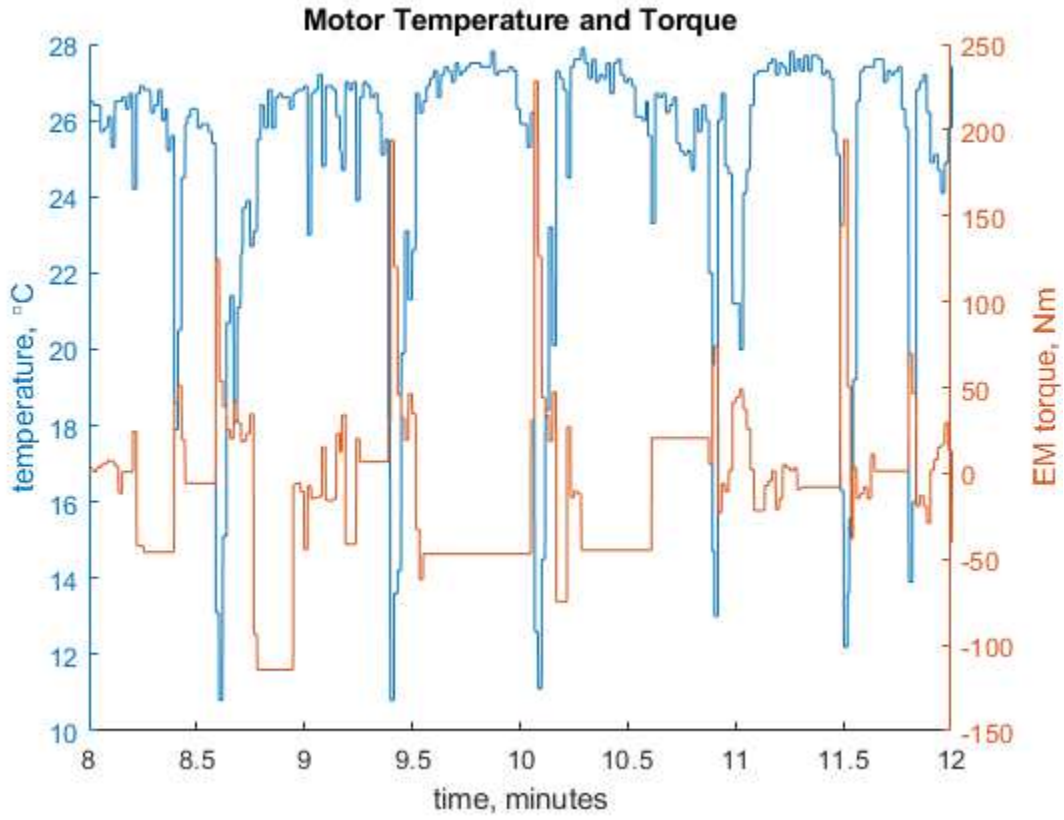

Figure 54: Temperature drops correlating to sudden EM torque increase

It is not immediately clear why this occurs; it could be electrically based: large inrush current to the motor causes EMI interference or power dips to the RTD sensor resulting in low temperature readings. It could also be that since the large torque increase also generally corresponds to motor speed increase, the sudden motion of the EM drastically increases turbulent flow inside the motor resulting in an increased cooling effect. Further work would be needed to determine the cause, however since all temperature readings are well below the design specifications in Table 6, this issue is not addressed.

Comparing the baseline test data to the model, the model average temperature (adjusting for observed ambient temperature of 10˚C, 9 LPM, and 13 LPM flow rates for oil and anti-freeze loops,

respectively) comes to 31.2˚C and 36.8˚C for the EM and Inverter, respectively. The corresponding average observed temperature in the baseline test are 25.5˚C and 35.6˚C. These results indicate that the cooling system is more than adequate for the TVP platform. Given the relative simplicity of the simulation model, it is not useful beyond predicting steady-state operating temperatures.

Chapter 4: Low Voltage and Communication

4.1 Controls Hardware Design

In the TVP, 'controls hardware' refers to the Hybrid Supervisory Controller (HSC), Inverter (aka EMC), battery management system (BMS), on-board charger (OBC), and all associated 12V powered components (pumps, fans, data acquisition equipment). It also refers to the equipment used to interface with, switch, and protect the various circuits. The following sections detail power distribution, communication, and testing. Figure 55 shows the general layout of low voltage wiring and low voltage components in the TVP. Note in the passenger compartment, there are four connectors that control the flow of accelerator pedal position sensor (APP or APPS) voltage signals. Connecting 'APP Connector' to 'ECM Connector' will revert the vehicle to stock ICE propulsion only, while connecting 'APP Connector' to 'HSC Connector' and 'Output Connector' to 'ECM Connector' will allow the HSC to modify or 'spoof' the APP signal from the pedal to the ECM (engine control module).

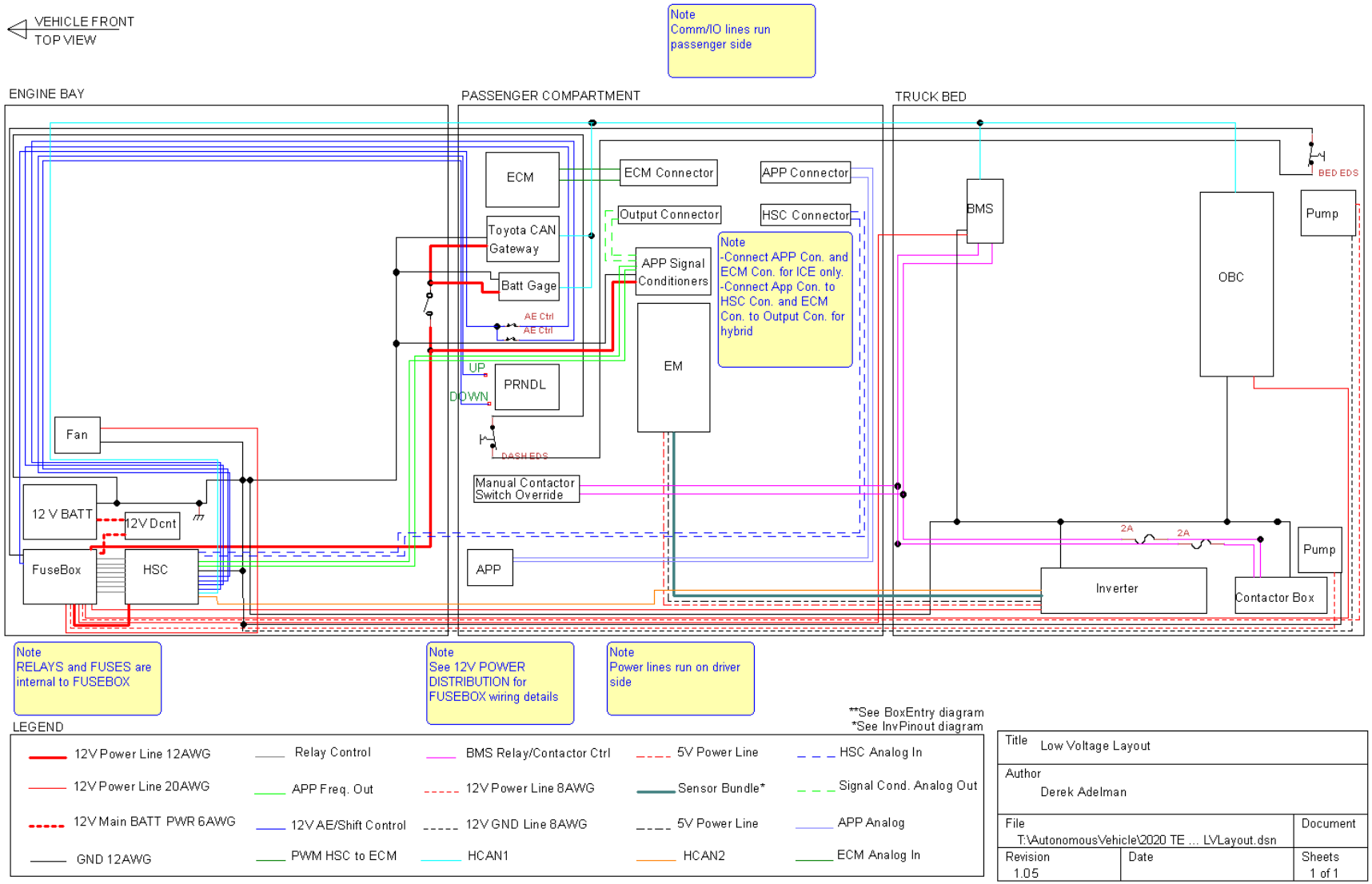

Figure 55: Low voltage controls hardware circuit diagram

Control of the hybrid vehicle with regards to the low voltage system centers around the driver torque request at the accelerator pedal. The driver requests torque by depressing the pedal, sending an analog voltage signal to the HSC, which internally splits the torque request based on the control algorithm between the ICE and EM. The software algorithm requires stock sensor information, which is obtained through the Toyota Gateway, a Toyota-developed controller that transmits information from the stock CAN bus onto Hybrid CAN Bus One (HCAN1) without divulging proprietary Toyota information. The ICE torque is spoofed by the HSC and sent to the ECM and the EM torque is sent to the Inverter via HCAN2.

For testing purposes, the vehicle must remain in its *s-shift* mode which allows the driver to actuate upshifts and downshifts off-schedule using the sport shifter on the PRNDL. This also allows the HSC to command shifts directly using the +/-Shift relays (see Figure 55). The shifter itself works as a simple 12V on-off switch; when the shift switch goes momentarily low the transmission control within the ECM initiates an upshift or downshift depending on the switch direction. Nominally, switch actuation will be controlled by the HSC according to the hybrid shift schedule.

4.1.1 Power Distribution

To power all components added to the TVP, a fuse box was constructed to provide power and overcurrent protection (i.e. automotive slow-blow fuses). A diagram of this fuse box and connections is shown in Figure 56. This fuse box provides power to all hybrid controllers (HSC, BMS, Toyota Gateway, etc), pumps, fans, and signal conditioners. Note that the +/-Shift relays simply pull the internal PRNDL voltage to ground, actuating a shift. The fuse box, along with the HSC, is mounted in the engine bay.

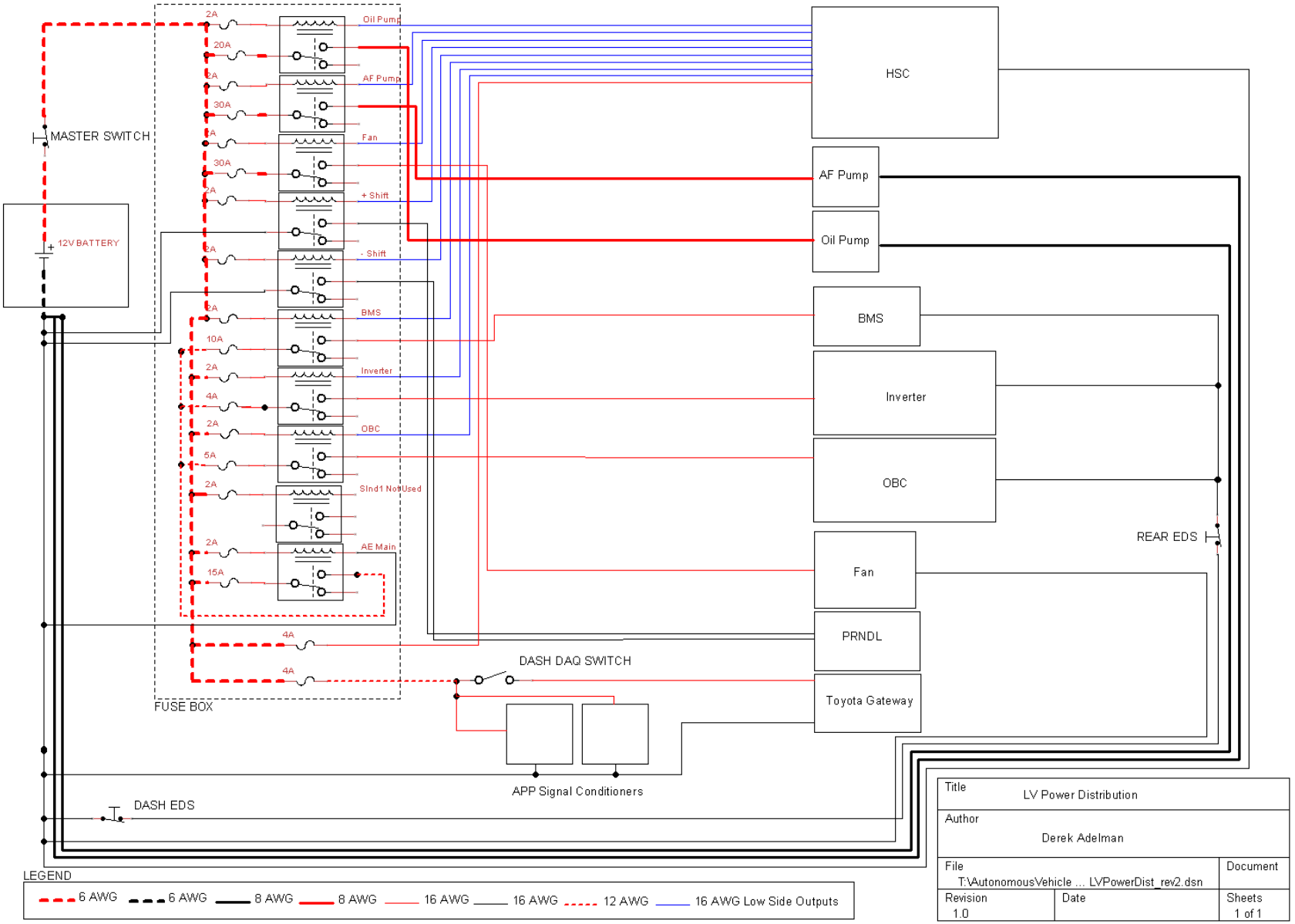

Figure 56: Fuse box circuit diagram

In the design of the fuse box, all 12V powered components that interact or control high voltage (Inverter, BMS, and OBC) have powered supplied to them through the AE (acceleration event) relay. This relay is activated by two normally closed emergency disconnect switches (EDS). When either of these switches are opened, the 12V power to the HV controllers is disconnected, disabling the entire high voltage system for safety purposes. Note also that anti-freeze and oil pumps have dedicated 8 AWG power and ground wires. It was determined during testing that the run from the fuse box to the pumps, located in the rear of the bed, resulted in voltage drop larger than 5% (maximum manufacturer allowed) using the 12 AWG prescribed by the manufacturers. Voltage drop is determined from the standard $V = IR$ equation where V is the battery voltage, I is the max current drawn by the pumps, and $R = \rho\frac{L}{A}$ is the resistance of the wire. Also, testing found the chassis grounding point in the rear of the bed had high resistance relative to the negative terminal of the battery, resulting in very high temperatures at the grounding point. Thus 8 AWG grounding wire was installed.

4.1.2 Accelerator Pedal Position Sensor Modification and Controller Area Network

4.1.2.1 Accelerator Pedal

The APPS signal consists of two analog voltage signals, one from 0.8-3.8V and the other from 1.5-4.5V. The value of these signals is determined by the pedal position which the ECM then uses to calculate and actuate torque from the ICE. To spoof this signal, the APPS signal is rerouted to the HSC and read via two analog-in pins. The HSC can then calculate a new ICE torque based off the torque-split strategy. Since the HSC does not have analog-out pins, a frequency modulated (FM) 0-12V square wave is sent out instead using two low-side driver (LSO) pins and a pull-up resistor circuit. The FM signal is routed to two signal conditioners, located in the glovebox, that convert the FM signals to analog signals corresponding to the original APPS signal ranges. This spoofed signal, now in analog form, is fed into the ECM resulting in an HSC-controlled ICE torque, Figure 57.

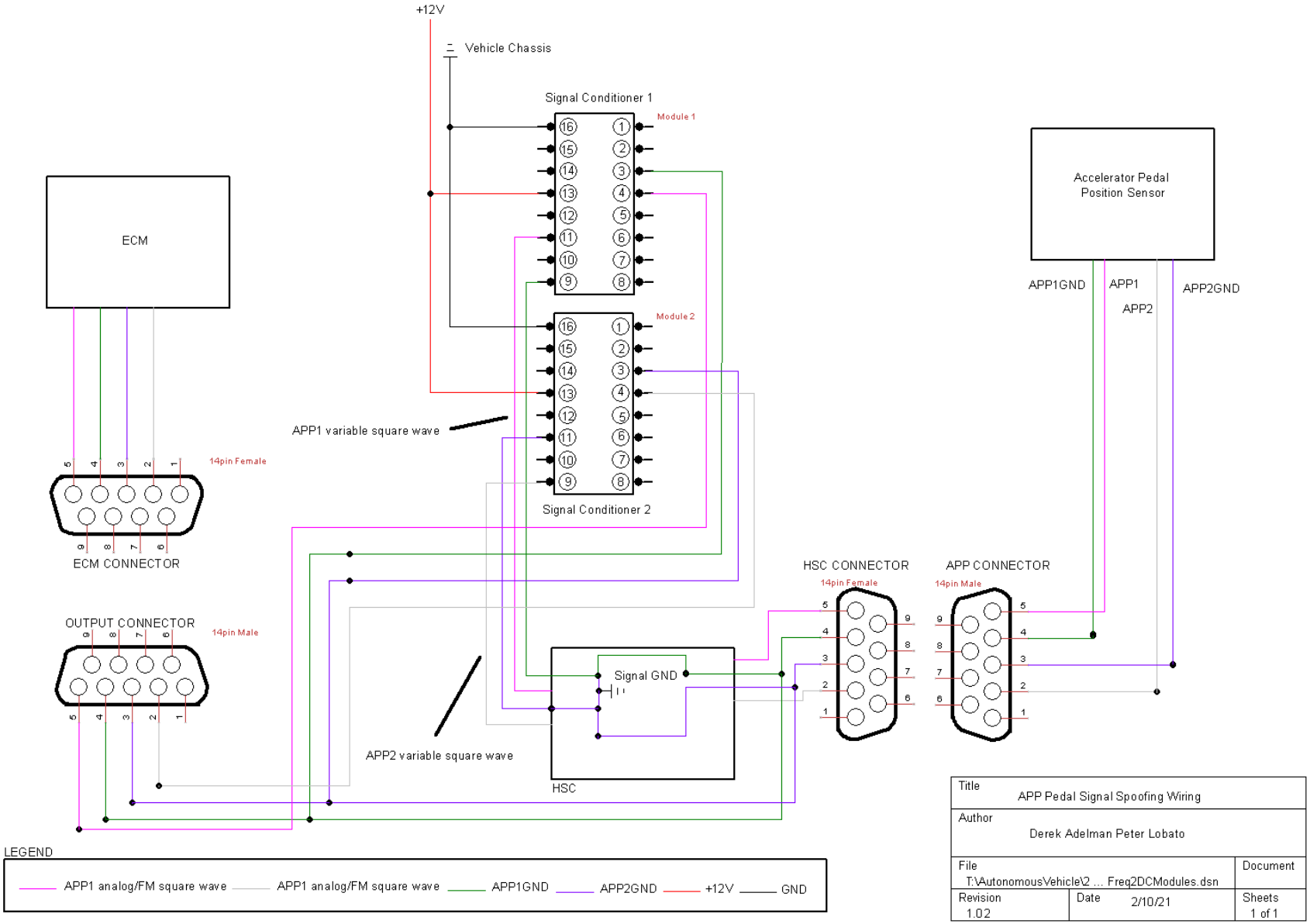

Figure 57: Accelerator pedal position signal routing circuit diagram

The performance of this method is seen in Figure 58, which shows the spoofed pedal percentage calculated by the HSC, and the actual pedal percentage seen by the ECM for a 5-minute road test. For this test, the mean absolute error (MAE) was found to be 5.37% ± 0.05% with 95% confidence. The standard deviation is 3.19%. For perspective, this resulted in the baseline EMS achieving a MAE of the driver requested torque of 11.22 ±0.29 Nm with 95% confidence. Using publicly available data for a general 4-cylinder ICE, the uncertainty in the brake specific fuel consumption is approximated to be roughly 2% [54].

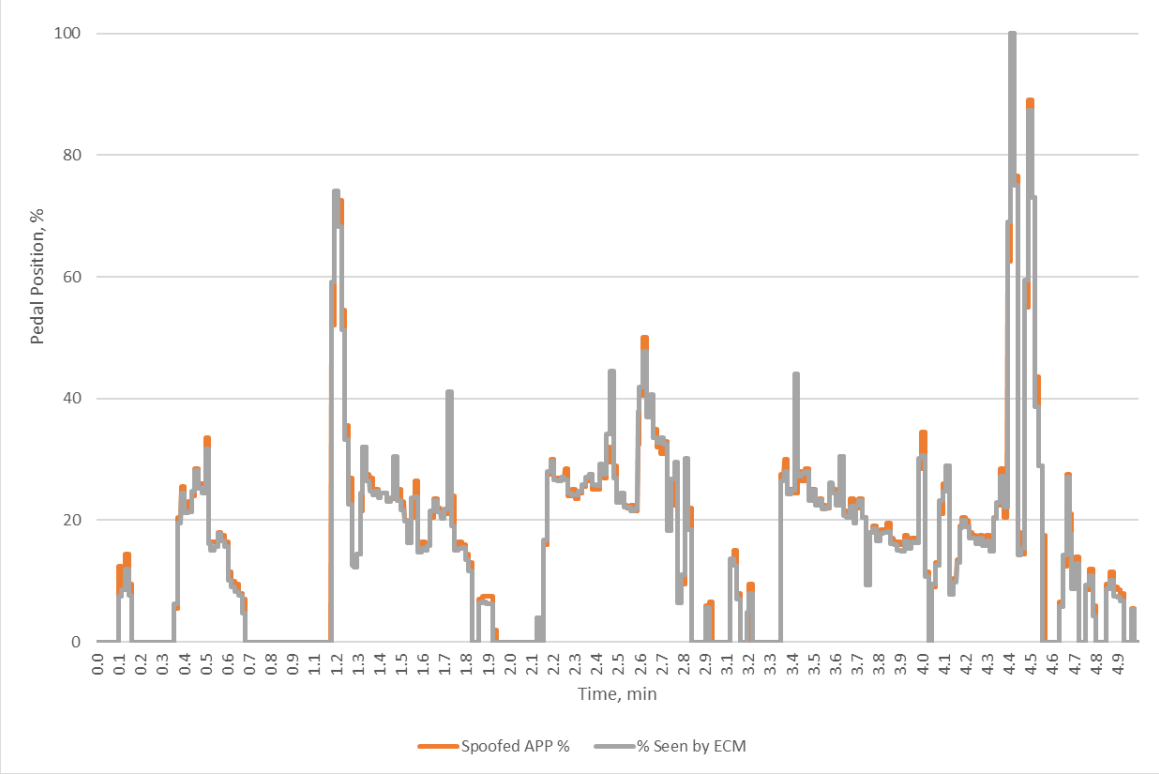

Figure 58: Spoofed pedal position % compared to actual pedal percentage seen by ECM

4.1.2.2 Controller Area Network

Two custom CAN buses were built to allow communication and control between the non-stock hybrid components. The hybrid buses serve as the interface between the HSC, BMS, EMC, OBC, and Toyota CAN Gateway. HCAN1 and HCAN2 are independent of any of the vehicle's stock buses and operate at 500 kbps with 120-ohm terminal resistors are located at the HSC and BMS for HCAN1 and the

HSC and Inverter for HCAN2. Each component has its own CAN protocol for communication and control functions as described in the following paragraphs.

Inverter

The EMC data has arbitration identifiers (ArbID) 0xA0 through 0xAF. This includes information such as motor torque, temperatures, motor flux, angular position, and any faults. The inverter is controlled using a single message on ArbID 0xC0, and the following parameters must be transmitted:

- Inverter Enable (on or off)
- Direction (CW or CCW)
- Speed (if Speed Mode Enabled is on: not used for TVP)
- Torque (if Speed Mode Enabled is not on)
- Inverter Discharge
- Torque Limit Command
- Speed Mode Enabled (not used for TVP)

The only parameter that changes as a function of time is Torque , a command to the inverter which is determined by the torque-split strategy in the HSC. A timeout of approximately 300ms is used as fail-safe so that if the inverter does not receive a command message within this time, it will set a fault and disable the electric motor.

The Inverter produces significant EMI, i.e. noise, when energized by the high voltage battery pack. To reduce noise and ensure reliable operation it was placed on its own CAN bus (HCAN2) in communication with only the HSC. The HCAN buses in the vehicle are constructed with twisted/shielded CAN wire with shielding grounded at both the HSC and Inverter for HCAN2 and HSC and BMS for HCAN1. General practice of where to ground shielding is often debated [55] [56] [57] [58]; however, it was found in testing that grounding at both ends of HCAN buses further reduced noise both qualitatively on an oscilloscope and quantitatively in bit stuff errors per second. Also, testing found that branches in

the HCAN buses needed to be kept under 3 feet in length, otherwise noise on the CAN bus would be induced, and communication errors would limit the function of the vehicle.

Battery Management System

The BMS broadcasts status data with ArbIDs 0x622 through 0x62A. This includes information such as battery voltage, battery current, resistance, temperatures, SOC, and any faults. The only control function the BMS performs is commanding high-voltage contactors. Contactor control is done through a single on/off bit in message ArbID 0x632. Through testing, it was found the BMS is extremely unreliable, failing to balance cells, losing communication with cell boards, and at one point, catching on fire due to failure of internal components. As such, manual contactor control switches were also installed in the event of BMS failure. This is possible as the BMS is only necessary in balancing the HV battery pack, discharging can occur without it.

On-Board Charger

The charger broadcasts status data on ArbIDs 0x610 through 0x614. This includes information such as charger temperature, type of utility power plugged in (US mains voltage 120V or 240V), charging current, charging voltage, and any faults. A single command message on ArbID 0x618 must be sent to the charger to initiate charging and includes the following values:

- Charger Enable
- Clear Faults
- Mains voltage request on/off
- Max current (AC, must keep below mains breaker rating, usually 16A)
- Desired charging voltage (DC)
- Desired charging current (DC)

Figure 59 is an example list of some of the messages mentioned above sent on the HCAN buses using 3rd party analysis software (Vehicle Spy).

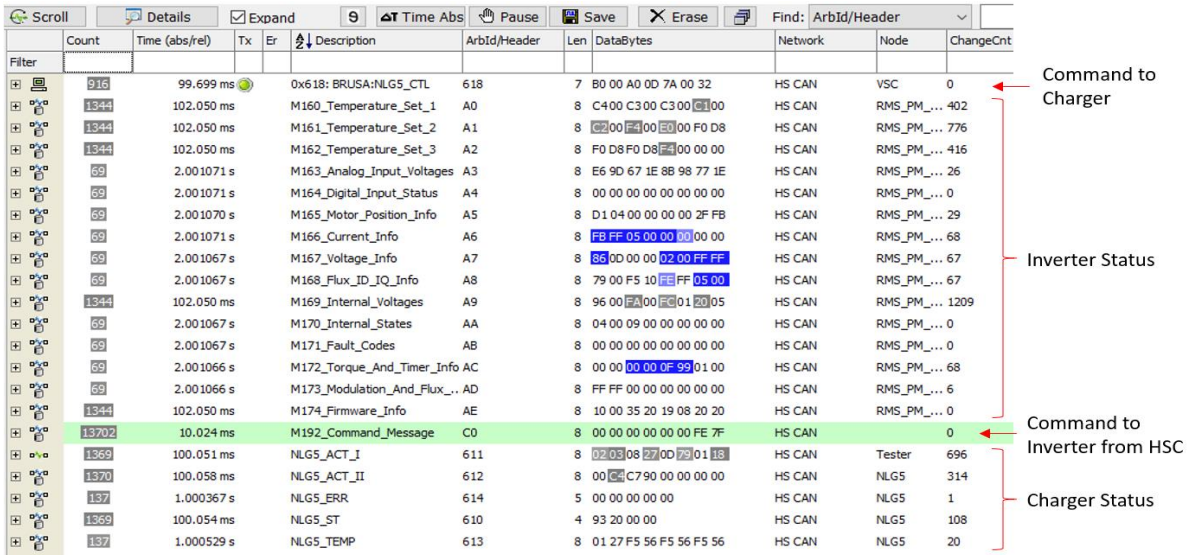

Figure 59: Messages present on HCAN buses

4.2 Controls Hardware Testing

4.2.1 Power Distribution

After construction and installation, the fuse box and power distribution of each component or group of components was tested. These results are summarized in Table 8. Note that the automotive relays used in the fuse box have a max continuous current rating of 35 A and each device has its own relay.

Table 8: Low voltage controls hardware power consumption

Component	Applied Voltage (V)	Current Draw (A)	Fuse (A)	Notes
Oil pump	PWM signal (12.55 peak, 8.5 average)	11.3	20	Pump can draw significantly more when PWM duty cycle is increased, 15 A fuse blown in testing.
AF pump	12.55	25.3	30	Both AF and oil pumps use 8 gage wire to minimize voltage drop
Fan (note there is only one fan)	12.55	12.5	30	Inrush current is high and has a relatively long duration. 30 A fuse is the lowest tested that does not blow on startup.
Hybrid controllers (EMC, BMS, HSC, Toyota Gateway, OBC)	12.55	Varies, power on: 3-4. Power on and at system operating conditions: 6-8	EMC-4, BMS-10, OBC-5, Gateway-4, HSC-4	Power varies due to auxiliary devices powered via controllers.
Total Power Consumption (W)	717			

4.2.2 Controller Area Network Validation

Three main steps were taken to validate the hybrid CAN bus: Signal quality validation, testing and troubling shooting CAN broadcast and command messages, and testing HSC functionality.

4.2.2.1 Signal Quality Validation

The CAN bus signal on both HCAN1 and HCAN2 was qualitatively evaluated using an oscilloscope with a differential probe and quantitatively by monitoring the number of bit stuff errors registered by the Vehicle Spy hardware and software. As mentioned, the Inverter produces significant amounts of EMI when energized and as such, HCAN1 and HCAN2 are constructed of specialized

twisted, shielded, CAN wire. After significant troubleshooting of CAN bus construction, HCAN1 displayed the following signal quality, Figure 60.

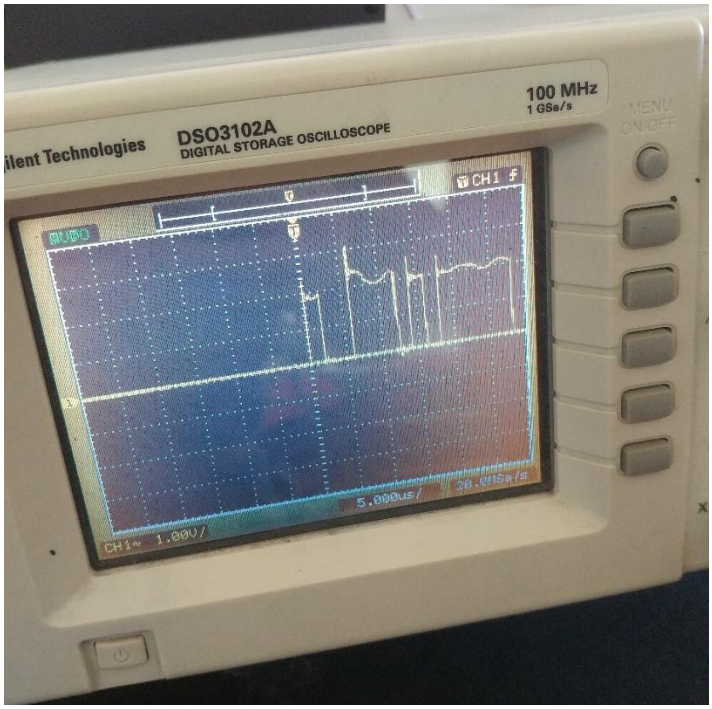

Figure 60: HCAN1 bus noise after significant noise attenuation

The resulting bit stuff error rate in Vehicle Spy ranged from 0 to 100 errors/sec depending on the length of the branch used to connect Vehicle Spy software and the Toyota Gateway to the bus. In general, the shorter the extension, whether shielded or unshielded, the lower the induced noise and error rate. HCAN2, containing just the Inverter and HSC displayed the following signal quality with the Inverter energized, Figure 61.

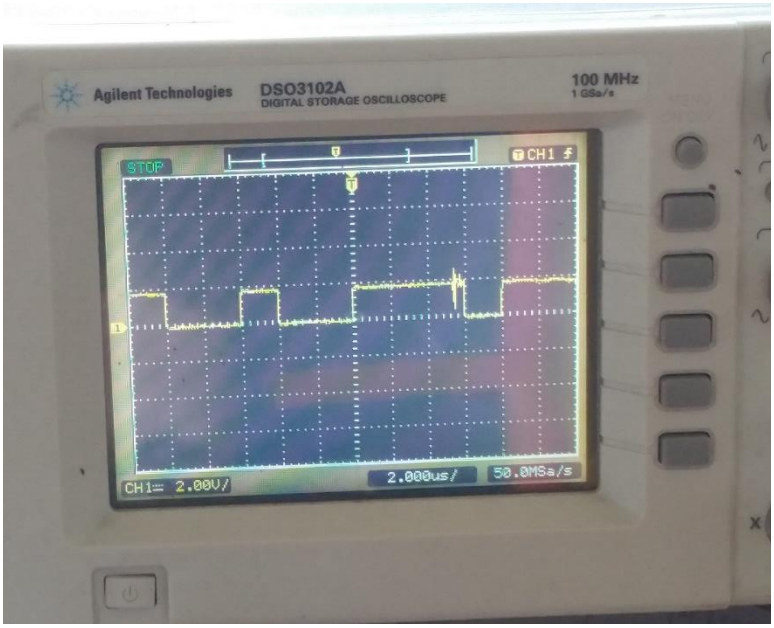

Figure 61: HCAN 2 bus noise after significant noise attenuation

It is seen that HCAN2 displays less ringing and overshoot behavior. However, noise is sometimes present in the signal, seen here at roughly 6 µs. This noise is believed to be a from a burst of Inverter EMI that occurs at a frequency of 25 kHz or every 40 µs, as it can be seen repeating at this frequency when the time axis of the oscilloscope is increased. Regardless, the noise is acceptable as Vehicle Spy had a rate of 0 stuff bit errors per second.

4.2.2.2 CAN Broadcast and Command Messages

To setup and test the CAN message formats, each CAN hybrid component was first individually controlled through Vehicle Spy before implementing the control on the HSC. The OBC and BMS CAN communication were validated by sending a charging command to the charger, Figure 62, and comparing the command charging voltage and current with that reported by the BMS graphical user interface (GUI) through the BMS RS232 port.

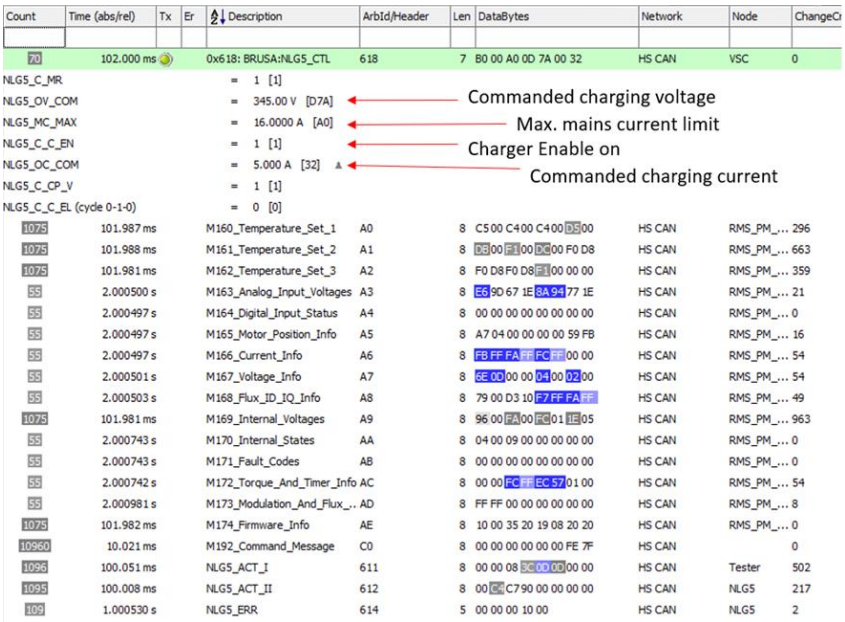

Figure 62: Control of BRUSA charger via HCAN1

Similarly, the Inverter was validated by sending motor torque commands via Vehicle Spy, visually confirming wheel rotation, and sensor data (DC bus current and Inverter output voltage) reported back to Vehicle Spy, Figure 63.

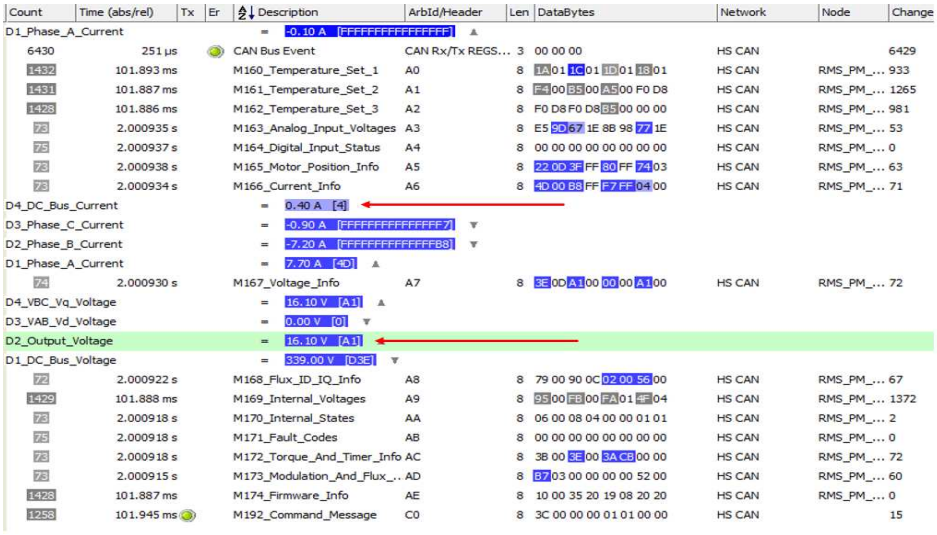

Figure 63: Reported current and voltage values of Inverter after torque is commanded

The data output shown above is summarized in Figure 64. Torque command (blue) is sent from Vehicle Spy and incremented up in steps of 1 Nm to 7 Nm and DC bus current (green) increases

concurrently. Motor speed (red) increases to roughly 200 rpm (shown negative in the plot as the direction of rotation is defined as negative in software), which translates to approximately 3 mph. The motor phase angle (yellow) goes from a constant value to random numbers between 0 and 360 degrees as would be expected as phase angle changes much faster than the sampling rate of the HCAN2 bus. Torque command and motor position does not change after zero torque is commanded and the Inverter is commanded to turn off (black).

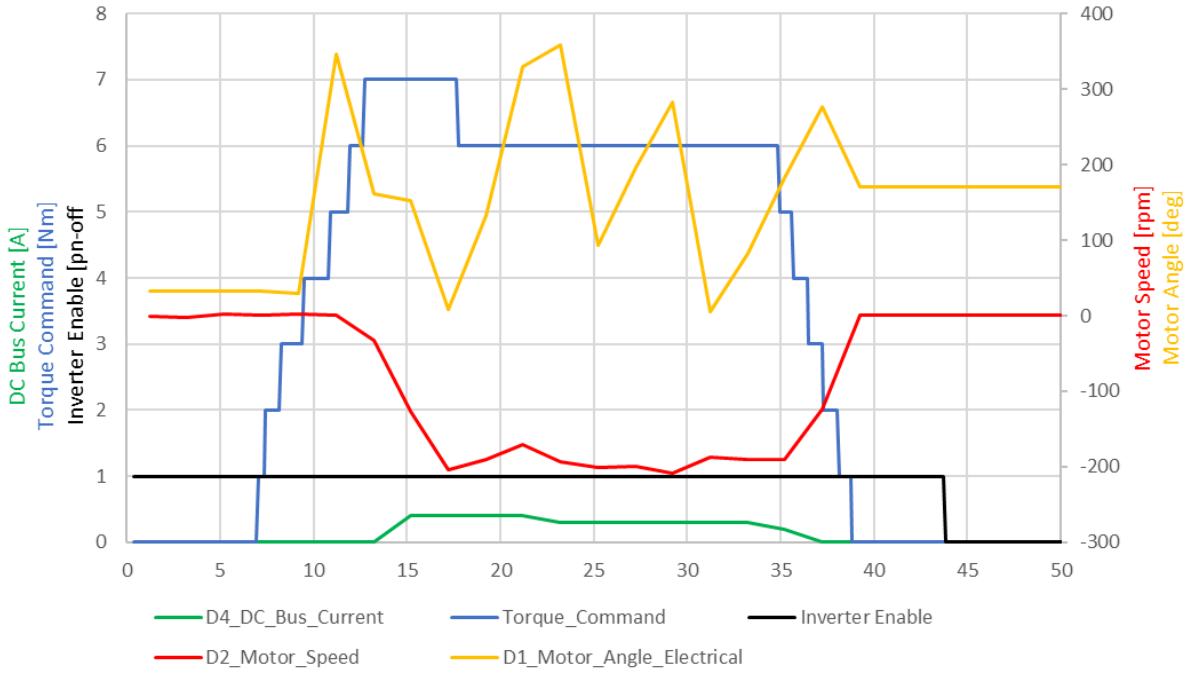

Figure 64: Recorded output of Inverter on HCAN2 through various torque commands

With the individual components tested through Vehicle Spy, the HSC was then added to the system to control the system functions previously done through Vehicle Spy. The software used to interface with the HSC is MotoTune and through it, high voltage contactor actuation, auxiliary device actuation (pumps, fans, shifting, etc.), and torque commands were all successfully actuated. The HSC was also able to retrieve stock vehicle information through the Toyota Gateway without any errors. Actuation of commanded torque through MotoTune was then replaced by the spoofed accelerator pedal position

signal discussed previously. The TVP was then successfully driven in hybrid mode with various basic torque split strategies as seen above in Figures 48 and 52.

Chapter 5: Initial PAE Testing Results

5.1 Testing Procedure

To perform repeatable acceleration event tests, the TVP was taken to Christman airfield. 0-25 and 0-40 mph runs were performed in both directions with driver-initiated shifts at 2500 rpm, Figure 65.

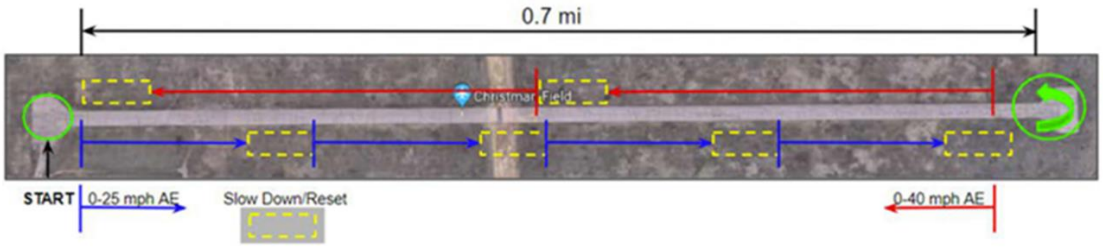

Figure 65: Acceleration runs at Christman airfield

Three test series were performed on separate days with each consisting of stock, Baseline, and PAE data collection for the two different acceleration events. Results for the second test series is summarized in the following section. Testing data can be found at T:\AutonomousVehicle\2021 TEMA\TestingLogs_Mototune

5.3 Test Series 2

Test series two was performed on 5/9/2021. Results are shown in the following figures and tables.

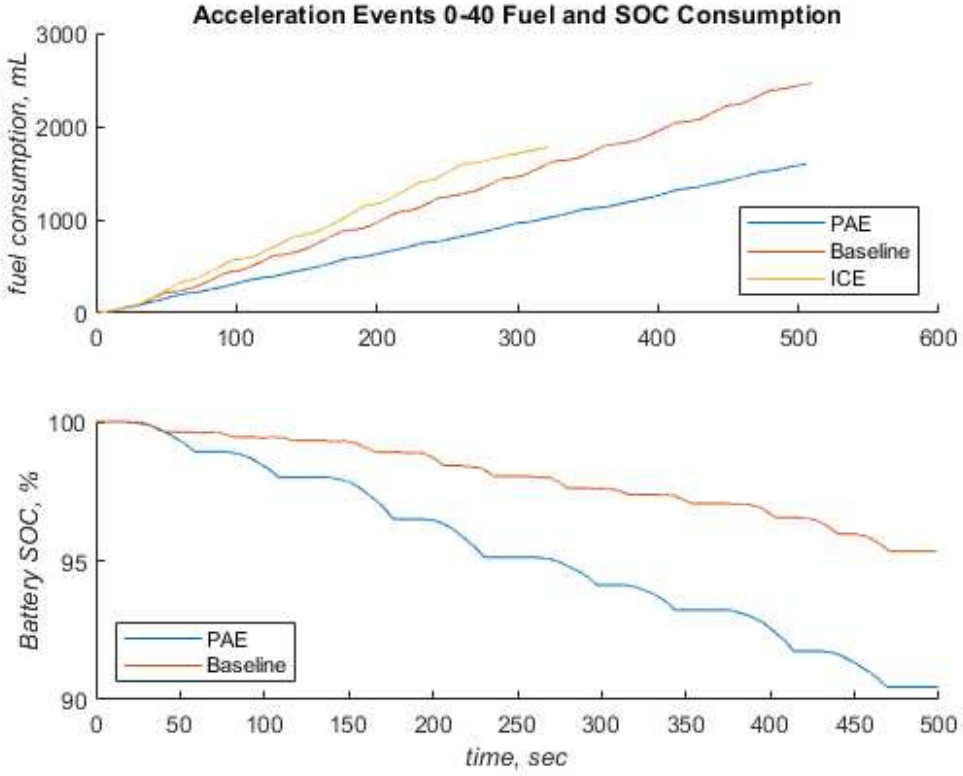

Figure 66: Fuel and battery energy consumption for multiple back-to-back accelerations, 0-40 mph

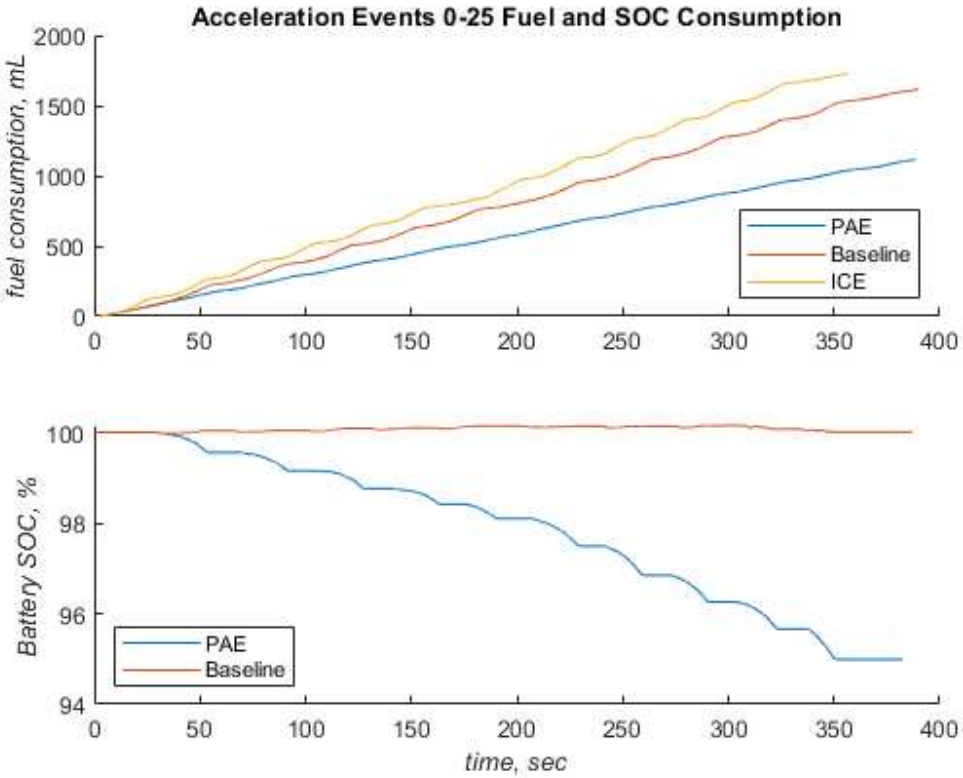

Figure 67: Fuel and battery energy consumption for multiple back-to-back accelerations, 0-25 mph

Table 9: Calculated MPG for each acceleration event for stock, Baseline, and PAE EMS

Test	Average MPG	Standard Deviation	Covariance	Mean MPG South	Mean MPG North
Stock, 0-25	10.21	0.325	3.19%	10.02	10.39
Baseline, 0-25	14.06	0.980	6.97%	14.66	13.58
PAE, 0-25	18.51	0.515	2.78%	18.54	18.49
Stock, 0-40	15.28	0.674	4.4%	15.00	15.56
Baseline, 0-40	17.25	0.362	2.10%	17.36	17.15
PAE, 0-40	28.07	0.450	1.60%	28.14	28.00

5.3 Initial Test Results Discussion

From the above data, PAE EMS does indeed attain better fuel economy than the Baseline EMS, by a significant margin. This is much larger than expected from early fuel economy simulations, indicating the PAE EMS needs to be tuned. In test series three this tuning was performed, bringing the PAE fuel economy much closer to Baseline, however these results are not included as data analysis and further PAE tuning is still being performed to ensure PAE EMS is operating as intended. At this time, the only conclusion that can be drawn from the above results is that PAE attains higher fuel economy because it is using more battery energy and needs to undergo further tuning until the battery energy consumption is the same as Baseline. While promising, these are initial results and much more testing is required before PAE EMS can be validated with confidence.

Conclusion

C.1

This thesis has described the design, manufacture, and performance evaluation of a parallel P3-type hybrid electric vehicle with regards to powertrain, cooling, and communication. The vehicle was built as a test vehicle platform to implement the EMS PAE strategy detailed in [7] as well as future V2X autonomous technologies.

Chapter 2 detailed the design, manufacture, and assembly of the hybrid powertrain. The design process consisted primarily of FEA modeling and stress analysis for shrink fits, as well as threaded and splined interfaces. Multiple manufacturing methods were discussed, most notably the creation of external and internal splines via 4-axis CNC milling and wire electronic discharge manufacturing. Heat treatment theory, methods, and results were also presented for 17-4 precipitate hardened and chromium-molybdenum steels. Economical metal identification methods and hardness testing were also addressed, which given the powertrain results, are deemed satisfactory for this type of application in the TVP.

Chapter 3 reviewed the cooling requirements of the high voltage system, design of a two-loop cooling system, one using a dielectric oil, the other anti-freeze, as well as construction and testing of said system. Before the system was built, quasi-equilibrium modeling was conducted implementing the $\varepsilon - NTU$ method to predict the performance of the system. It was determined from the model that a minimum speed of roughly 10 mph is needed to maintain component temperatures below their maximum limits. In road testing, it was found the system steady-state temperatures were well below the maximums specified in the system requirements and the average temperature of the components agreed well with the steady-state temperatures of the adjusted model.

In Chapter 4, low voltage controls hardware implementation pertaining to power distribution, accelerator pedal position senor signal modification, and controller area network communication was described. Primary power distribution results found that significant voltage drop occurred from the front to rear of the vehicle, requiring heavier gage wire. Total power consumption was found to be over 700

Watts. It was also seen that spoofing of the pedal position had an average error of 5.37% ± .05% with 95% confidence, which was deemed successful, as this corresponds to a MAE torque application of 11.22 ±0.29 Nm with 95% confidence. CAN communication was verified for each component and signal quality was tested qualitatively and quantitatively via bit errors/sec. Through this testing, it was found that shielding performance improved when grounding at both ends of the CAN bus.

Finally, Chapter 5 briefly presented some initial PAE EMS testing results, indicating that PAE does achieve higher fuel economy that Baseline EMS. However, further testing and tuning of the PAE EMS is required before results can be validated.

This design and development effort is novel in that this is the first document development of a vehicle that is capable of performing predictive optimal energy management and control. This is done without knowing any propriety Toyota information, specifically stock vehicle communication and operation such as CAN protocols, stock transmission shift schedules, and engine pedal maps, to name a few. The result is a relatively robust and fully operational test vehicle platform for PAE EMS and V2X technology research.

C.2 Future Work

As outlined above, TVP design and validation as well as initial testing has been performed. The next steps for the TVP as it relates to PAE EMS are tuning the PAE strategy algorithm to attain maximum fuel economy improvements, validate results and performance, and improve drivability. Part of this may include working with Toyota to obtain more transmission shift control, so the vehicle can be tested in a larger variety of acceleration behavior. Subsequently, the “predictive” part of PAE needs to be developed so the TVP can automatically discern what acceleration event is about to occur. This will incorporate V2X technology (GPS, vehicle-to-infrastructure communication, vehicle sensing, etc.) as the TVP will ultimately need to be able to perform this prediction on the road in real world driving conditions.

Two areas of more focused work are addressed here. The first involves performing a detailed characterization of the YASA electric motor. By knowing the conditions in which the YASA is most efficient, this information could be used to increase the fuel economy gains when integrated into an EMS strategy, or ideally, further improve the EMS PAE strategy. Such work is envisioned to encompass experimental determination of the YASA magnetic flux linkages and ultimately a set of dynamical equations describing the YASA and TVP powertrain, which would then be simulated in software to determine if any efficiency conditions exist that could be leveraged in an EMS strategy. If such conditions exist, they could be implemented on the TVP and tested for EMS improvement. A starting point for simulations can be found in [59] and theoretical operation of electric motors can be found in [60] [61].

The second proposed area of improvement for this vehicle focuses on the physics behind grounding the CAN shielding wire in the TVP. Noise due to the Inverter is a persistent problem on the HCAN buses and there is much debate about whether proper shield grounding constitutes grounding at one end of the CAN bus or both. So a proposed research topic is to perform a detailed analysis on EMI effects on signal quality of automotive CAN networks and what the best method of attenuation is. Similarly to the YASA analysis, this work could then be tested on the TVP or on a benchtop using TVP components.

References

[1] S. Onori, Hybrid Electric Vehicles: Energy Management Strategies, Springer, 2016.

[2] Asher, Z., Wifvat, V., Navarro, A., Samuelsen, S. et al., "The Importance of HEV Fuel Economy and Two Research Gaps Preventing Real World Implementation of Optimal Energy Management," SAE Technical Paper 2017-26-0106, 2017, https://doi.org/10.4271/2017-26-0106.

[3] Baker, D., Asher, Z., and Bradley, T., "Investigation of Vehicle Speed Prediction from Neural Network Fit of Real World Driving Data for Improved Engine On/Off Control of the EcoCAR3 Hybrid Camaro," SAE Technical Paper 2017-01-1262, 2017, https://doi.org/10.4271/2017-01-1262.

[4] Liu, K., Asher, Z., Gong, X., Huang, M. et al., "Vehicle Velocity Prediction and Energy Management Strategy Part 1: Deterministic and Stochastic Vehicle Velocity Prediction Using Machine Learning," SAE Technical Paper 2019-01-1051, 2019, https://doi.org/10.4271/2019-01-1051.

[5] Thomas Cummings, Thomas H. Bradley, Zachary D. Asher, "The Effect of Trip Preview Prediction Signal Quality on Hybrid Vehicle Fuel Economy," *IFAC-PapersOnLine,* vol. 48, no. 15, pp. 271-276, https://doi.org/10.1016/j.ifacol.2015.10.039, 2015.

[6] Z. D. Asher, D. A. Baker and T. H. Bradley, "Prediction Error Applied to Hybrid Electric Vehicle Optimal Fuel Economy," in IEEE Transactions on Control Systems Technology, vol. 26, no. 6, pp. 2121-2134, Nov. 2018, doi: 10.1109/TCST.2017.2747502.

[7] D. Trinko, "Predictive Energy Management Strategies for Hybrid Electric Vehicles Applied During Acceleration Events," Colorado State University, Fort Collins, 2019.

[8] T. H. Bradley and A Frank, "Design, Demonstrations and Sustainability Impact Assessments for Plug-in Hybrid Electric Vehicles," Renewable and Sustainable Energy Reviews, https://doi.org/10.1016/j.rser.2007.05.003, vol. 13, no. 1, pp. 115-128, 2009.

[9] "Mild Hybrid Electric Vehicle (MHEV) – Architectures," Xengineer, x-engineer.org/automotive-engineering/vehicle/hybrid/mild-hybrid-electric-vehicle-mhev-architectures/.

[10] T. Bradley, D. Trinko, M. Knopf, T. Johnson and G. DiDomenico, "CSU Test Vehicle Platform Design," *Colorado State University,* 2019.

[11] T. Woolmer and M. McCulloch, "Analysis of the Yokeless And Segmented Armature Machine," in *2007 IEEE International Electric Machines & Drives Conference, doi: 10.1109/IEMDC.2007.382753*, Antalya, 2007.

[12] D. J. Dunn, "Mechanical Principles Thin Walled Vessels and Thick Walled Cylinders," Http://Www.freestudy.co.uk/Statics/Complex/t1.Pdf.

[13] B. McGinty, "Von Mises Stress," *www.continuummechanics.org/vonmisesstress.html.*

[14] "YASA Installation Guide," YASA Limited, 2018.

[15] C. MacCauley and E. Oberg, Machinery's Handbook: a Reference Book for the Mechanical Engineer, Designer, Manufacturing Engineer, Draftsman, Toolmaker, and Machinist.

[16] "Mechanical Properties of Fasteners Made of Carbon Steel and Alloy Steel," Https://Www.nbk1560.Com/Images/En/Product/technical_data/teiketubuhin_seishitsu_NBK/teiketubuhin_seishitsu_NBK_1.Pdf.

[17] J. Yochim, "Mechanical Properties," fullerfasteners.com/tech/mechanical-properties/, 2017.

[18] "Bolt Grade Markings and Strength Chart," www.boltdepot.com/fastener-information/materials-and-grades/bolt-grade-chart.aspx.

[19] C. Cavallo, "All About 6061 Aluminum (Properties, Strength and Uses)," Thomasnet® - Product Sourcing and Supplier Discovery Platform - Find North American Manufacturers, Suppliers and Industrial Companies, www.thomasnet.com/articles/metals-metal-products/6061-aluminum/.

[20] "Tight-Tolerance Multipurpose 6061 Aluminum Rods and Discs," McMaster, www.mcmaster.com/aluminum/tight-tolerance-multipurpose-6061-aluminum-rods-and-discs/.

[21] R. Juvinall and K. Marshek, Fundamentals of Machine Component Design, Wiley, 2017, pp. 227-254.

[22] E. Chesson, "W. H. STATIC STRENGTH OF HIGH STRENGTH BOLTS UNDER COMBINED SHEAR AND TENSION," *University of Illinois,* 1964.

[23] CG, "YASA P400 S MOTOR INSTALLATION," YASA Motors, 2015.

[24] "How Accurate Is Wire EDM?," MicroPulse West, www.micropulsewest.com/our-blog/how-accurate-is-wire-edm/#:~:text=While%20accuracies%20of%20%2B%2F%2D%200.00004,the%20time%20available%20for%20machining, 2017.

[25] R. Chen and W. Yeun, "Review of the High-Temperature Oxidation of Iron and Carbon Steels in Air or Oxygen," *Oxidation of Metals 59, https://doi.org/10.1023/A:1023685905159,* p. 433–468, 2003.

[26] K. G. Swift and J. D. Booker, Manufacturing Process Selection Handbook, Elsevier: Butterworth-Heinemann, 2013.

[27] D. H. Herring, "Principles of Gas Nitriding: The Nitriding Process (Part 1)," Industrial Heating RSS, 2012.

[28] G. E. Moore and H. H. Hansen, "Direct Observation of the Thermal Dissociation of Molecular Nitrogen," *AIP The Journal of Chemical Physics,* vol. 54, no. 1, 2003.

[29] D. R. Askeland and W. J. Wright, The Science and Engineering of Materials, Cengage Learning, 2016.

[30] Zai, "Laser Powder Bed Fusion of Precipitation-Hardened Martensitic Stainless Steels: A Review," *Metals - Open Access Metallurgy Journal,* 2020.

[31] "AK Steel Product Bulletin: 17-4 PH Stainless Steel," AK Steel, www.aksteel.com/sites/default/files/2018-01/174ph201706.pdf, 2013.

[32] "Precipitation Hardening Stainless Steels – Alloys, Properties, Fabrication Processes," AZoM.com, www.azom.com/article.aspx?ArticleID=2819, 2020.

[33] "4140 Steel Applications: An Expert Guide to the Top 10 Applications," Wisconsin Metal Tech, wisconsinmetaltech.com/4140-steel-applications-top-10/, 2020.

[34] "AISI 4140 Chrome-Molybdenum High Tensile Steel," AZoM.com, www.azom.com/article.aspx?ArticleID=6116, 2019.

[35] "AISI 4340 Alloy Steel (UNS G43400)," AZoM.com, www.azom.com/article.aspx?ArticleID=6772#:~:text=or%20heat%20treatment.-,Applications,gear%2C%20and%20other%20structural%20parts, 2013.

[36] J. Hektor, "TRADITIONAL METAL IDENTIFICATION TECHNIQUES," Winn Machine, winnmachine.com/2020/06/11/traditional-metal-identification/, 2020.

[37] "Metal Identification Tests: Methods & Tips On How to Identify Metals," The Welding Handbook, www.weldinghandbook.com/types-of-metals/metal-identification/, 2021.

[38] "Stainless Steel: The Role of Nickel: Nickel Institute," Nickel Institute, nickelinstitute.org/about-nickel/stainless-steel.

[39] "Spark Testing of Metals Poster," Hobart Institute of Welding Technology, www.welding.org/product/spark-testing-metals-poster/?doing_wp_cron=1616858586.5210158824920654296875, 2016.

[40] M. A. Ahssi, "The Effect of Nickel on the Microstructure, Mechanical Properties and Corrosion Properties of Niobium–Vanadium Microalloyed Powder Metallurgy Steels," *Materials, https://doi.org/10.3390/ma13184021,* vol. 13, no. 18.

[41] S. Singla and A. Bhattacharya, "Dissimilar GTAW between AISI 304 and AISI 4340 Steel: Multi-Response Optimization by Analytic Hierarchy Process," *SAGE Journals, journals.sagepub.com/doi/10.1177/0954408916641458,* 2017.

[42] "How To Weld 4140 Steel," WELDING ANSWERS, weldinganswers.com/how-to-weld-4140-steel/, 2015.

[43] D. Adelman and B. Masterson, "Chrome Moly Knuckle," 2020.

[44] "Heat Treatment of Low-Alloy Steels: Effects on Macroscopic Mechanical Properties," Massachusetts Institute of Technology Department of Mechanical Engineering, https://doi.org/10.3390/ma13184021, Cambridge.

[45] "Through-Hardening Low Allow Steel Bar 4140," Atlas Specialty Metals, www.atlassteels.com.au/documents/Atlas4140.pdf.

[46] "Through-Hardening Low Allow Steel Bar 4340," Atlas Specialty Metals, www.atlassteels.com.au/documents/Atlas4340.pdf.

[47] A. Clarke, "Perspectives on Quenching and Tempering 4340 Steel," *https://doi.org/10.1007/s11661-020-05972-1.*

[48] "4340 High Tensile Steel," Interlloy, www.interlloy.com.au/our-products/high-tensile-steels/4340-high-tensile-steel/.

[49] "Heat Treating AISI / SAE 4140 Steel," Anvilfire.com, www.anvilfire.com/FAQs/heat-treating-4140.php.

[50] C. Brune and A. Khan, "RMS PM/RM Hardware User Manual," Cascadia Motion.

[51] "Fleetguard LF16035 Stratapore Oil Filter," KLM Performance, klmperformance.com/products/fleetguard-lf16035-stratapore-oil-filter.

[52] T. L. Bergman, Fundamentals of Heat and Mass Transfer, Wiley, 2011, pp. 718-721.

[53] A. Khot, "An Overview of Radiator Performance Evaluation and Testing," *Journal of Mechanical and Civil Engineering,* pp. 7-14.

[54] "Brake Specific Fuel Consumption (BSFC)," x-engineer, https://x-engineer.org/automotive-engineering/internal-combustion-engines/performance/brake-specific-fuel-consumption-bsfc/.

[55] I. Bure, "Influence of the shield grounding system on choice of section," *Russ. Electr. Engin., https://doi.org/10.3103/S1068371216110031,* p. 641–646, 2016.

[56] "Where Should We Terminate the Cable Shields?," Instrumentation Tools, instrumentationtools.com/where-should-we-terminate-the-shield-and-why/, 2017.

[57] "Understanding Shielded Cable," AlphaWire, https://www.mouser.com/pdfdocs/alphawire-Understanding-Shielded-Cable.pdf.

[58] L. West, "Cable Shield Grounded At One End Only," EMC Standards, www.emcstandards.co.uk/cable-shield-grounded-at-one-end-only, 2018.

[59] D. Adelman, "Dynamics and Speed Control of Axial Flux Permanent Magnet Brushless DC Machines," Colorado State University, Fort Collins, 2020.

[60] P. C. Krause, Analysis of Electric Machinery, IEEE Press, 1995.

[61] P. C. Krause, Electromechanical Motion Devices, Wiley, 2012.

Appendix

The following is meant as a resource for future CSU graduate students working on the TVP.

Procedures

Starting/Shutting Down the TVP

1. Check that there are no check engine or warnings lights on the dash (12V master switch must be ON!).
    a. If there are, clear all DTCs with a diagnostic tool.
2. With the vehicle off, turn on the 12V master switch. Always make sure the vehicle is completely powered off when the 12V master switch is off, otherwise the vehicle will throw APPS DTCs and go into limp mode.
3. With the 12V master switch on, start the TVP. If the BMS throws an error and opens contactors, cycle power to the HV components via the dash EDS switch. This should clear any BMS faults. If it does not, or if other faults occur, shut down and begin diagnosing.
4. To shut down, bring the car to a stop and place into park.
5. Fully turn off the vehicle (i.e. make sure auxiliary is off as well, not just the engine).
6. Turn off the 12V master switch.

Driving the TVP

1. To drive the vehicle in ICE mode only, shift the PRNDL to Drive.
2. To drive in hybrid mode, shift the PRNDL to Sport mode.
3. To remove the HSC's control of the APP signals, connect 'APP' to 'ECM' in the passenger floor connectors. To give HSC control of the signals, connect 'APP' to 'To HSC' and 'From Signal Conditioners' to 'ECM'.
4. For high pedal position percentages (roughly greater than 70%) and loads, the Tacoma transmission will not shift when told to by the sport shifter. Nothing can be done about this. The transmission will ultimately shift when it wants to protect itself and will not follow driver or HSC shift commands via the sport shifter under high loads. For casual accelerations, the transmission shifts when the sport shifter commands a majority of the time.
    a. Hold the overhead traction control button while in neutral until "TRAC OFF" is displayed on the dash.
5. Drive slowly over speed bumps or other potholes/road obstructions. The EM is cantilevered off the end of the transmission and there is a high risk of powertrain failure if care is not taken over bumps. It is recommended to install more EM supporting brackets (green cantilever brackets).
6. When starting test drives, check the inlet pressure to the EM at the pressure gage in between the seats. This pressure can change depending on the temperature of the fluid. Adjust the potentiometer next to the flow meter and pressure gage until the inlet pressure is just below 1 bar. It is recommended to install a pressure bypass valve to resolve this issue.
7. After a couple of hours of driving, check the ATF fluid level in the transmission. The powertrain does leak ATF through the tailstock seal. Fluid can be seen leaking from the different interfaces between the EM, donut, and dinnerplate. The leaking is not bad but needs to be monitored. It is recommended to disassemble the powertrain and install sealant at these interfaces. The YASA EM is IP67 rated so do not worry about the leaking ATF affecting the motor.
8. It is also recommended to check the assembly of Part E and G if any abnormal noises or vibrations occur.

Charging the TVP

1. Hook up a 12V power supply to the battery terminals.
2. Make sure the DAQ switch on the dash is on.
3. Undo the split loom containing the wires that go to the HSC. In the loom there are wire pigtails that allow one to turn on components by connecting the pigtail to ground without turning on the HSC.
4. Disconnect the HSC connector that has 12V power (leftmost one).
5. Connect the BMS and OBC pigtails to ground (these are labeled).
6. Turn on the 12V master switch. The BMS and OBC should turn on, with everything else off.
7. Hook up the charging harness to the OBC. The harness has a female EVSE receptacle. Connect the 3-phase part of the harness to the 3-phase connector that is attached to the OBC (this is in the battery box) and the Deutsch connector from the charging harness to the Deutsch connector that is attached to the OBC. The Deutsch connector contains the control pilot and proximity lines required for level 2 charging. At this point, plug in the male EVSE receptacle from the wall into the charging harness. Make sure the EVSE has 'Power' and 'Charging' illuminated.
8. Plug in the silver laptop (that has 'ecocar' as the username and no password) to the RS232 on the BMS and to HCAN1 in the glovebox.
9. Open Vehicle Spy and the eLithion BMS GUI. These are both pinned to the taskbar.
10. In Vehicle Spy, open Toyota_VSpy_Config_V2. The CAN commands to use are 'BRUSA:NLG5_CTL' and 'BMS: Contactor_Request'.
11. Set the 'BMS: Contactor_Request' rate to 0.1s. You should hear the contactors close.
    a. Check the BMS GUI. Often the BMS loses connection to the cell boards when the contactors close. To fix this, go to the Configure tab and then the Measure subtab. Click 'Relearn' in the bottom left until the BMS finds all the cell boards again. This may take several clicks.
12. With the contactors closed, set the 'BRUSA:NLG5_CTL' rate to 0.1s. You should hear the BRUSA fans come on and see negative current on the BMS GUI Status tab. Charging is now occurring.
    a. If not, check that the BRUSA is not in a fault condition in the 'NLG5_ERR' CAN message (arbID 614). You can clear faults by cycling 'NLG5_C_C_EL' signal in the 'BRUSA:NLG5_CTL' message (cycle 0-1-0).
13. Charging can be done remotely by first performing steps 1-8 then remotely logging into the silver laptop. To do this, you must connect to the CSU network either via directly connecting to the network or through a VPN https://www.acns.colostate.edu/networking/. The silver laptop IP address can be found in the settings. It will change each time the laptop connects to the network.
    a. Once you are connected to the CSU network, open remote desktop connection and type the IP address found in settings in the Computer box. The username is ecocar. No password is required. Just hit enter without typing in a password and you should connect. IF YOU ARE CHARGING REMOTELY, YOU MUST ACTIVELY MONITOR THE CHARGING PROCESS. THE BMS HAS BEEN KNOWN TO CATCH FIRE.
    b. Note that you must open Vehicle Spy physically at the silver laptop beforehand. You cannot open it through remote desktop.
14. To stop charging, simply turn the HCAN1 rates in Vehicle Spy to 0. The BMS will then continue to balance the cells until they reach the criterion entered in the BMS GUI. If charging remotely, once balancing is completed and the contactors are opened and HCAN1 messages disabled, you can safely disconnect from remote desktop. NOTE, DO NOT CLOSE VEHICLE SPY. IT CANNOT BE OPENED AGAIN THROUGH REMOTE DESKTOP.

Powertrain Disassembly

1. Drain the oil coolant loop. This can be done by unhooking the tube at the L2LPHE and using the pump to pump out the fluid.
    a. Note the pump must NEVER be run in reverse. Always make sure the switch is in the II position at the PWM box in the back left of the truck bed.
2. Disconnect the electrical connections from the PRNDL and remove the PRNDL, protective acrylic covering, PRNDL mounts, and handbrake.
3. Disconnect the EM sensor wires (two MIL type connectors on the passenger side and the 5-wire connector) and the coolant hoses.
4. Remove the four propshaft bolts at the rear differential and the two bolts holding the propshaft bushing. Slide the propshaft and Part L off Part G.
5. Place the transmission jack under the EM and crank it up so it just slightly touches the bottom of the EM. It is useful to raise the vehicle slightly using the shop lift.
6. At this point, start removing the M8x1.25 bolts holding the EM in place. Note that a lot of ATF fluid will begin to leak, so prepare mats or spill pans to catch what you can. It will be messy.
7. Loosen the bolts to hand tightness. Now using two ¼" extensions, remove the M6 bolt that is down the axial hole of Part G. Use a magnet grabber or Teflon tape on the bit to remove it from the hole.
8. Now fully remove the M8x1.25 bolts. Note that the lower two bolts are 18-8 stainless (torque to 15Nm) and have nuts on the back that secure the green cantilever mounts. You must remove these nuts first before trying to loosen these bolts.
9. With all M8 and the one M6 bolts removed, you can now begin to slide the EM and the assembly of Part E and G off the dinnerplate (Part I) and the transmission output shaft. A prybar may be required to break the assembly loose. It should not be needed once the motor is separated approximately 1 inch from Part I. Use the transmission jack as a flat support that the EM can ride on as you slide it off. The EM will bring the assembly of Part E and G with it.
    a. This step will be tricky as it does require some leverage and bodyweight to remove the EM assembly. Do not try and do this by yourself. This is at least a two-person job and can be dangerous as heavy equipment (EM weighs 60lbs by itself) is being removed while underneath a vehicle.
10. As the EM is slid toward the back of the vehicle, you can begin lowering the transmission jack at the same time as soon as the splines of Part E disengage from the transmission output shaft (this occurs at approximately 6 inches of separation between the EM and Part I mounting face). To remove the end of Part E from the pocket formed by Part I and D you will need to lower the EM so the top of it will clear the transmission tunnel. It may also be helpful to tap the assembly of Part E and G either forward or backwards relative to the EM as you are removing it. The EM cannot be removed from the powertrain by completely removing Part G from the internal EM splines. The clearances do not allow for it. The EM and Parts E/G must all come off together.
11. Once the assembly of the EM and Parts E/G are lowered down from the transmission, a mallet can be used to tap out the assembly of E and G from the EM.

Data Locations

1. CAD and drawings can be found at T:\AutonomousVehicle\2020 TEMA Research\TVP\TVP Project Folder_updated_1_11_21\Powertrain\Updated CAD_10_29_2020\CAD
2. LV diagrams can be found at T:\AutonomousVehicle\2020 TEMA Research\TVP\TVP Project Folder_updated_1_11_21\LV Wiring Diagrams

3. Manuals for BMS, OBC, INV, HSC, Gateway, YASA EM, and pumps can be found at T:\AutonomousVehicle\2020 TEMA Research\TVP\TVP Project Folder_updated_1_11_21\Component manuals
4. Project Updates and power points can be found at T:\AutonomousVehicle\2020 TEMA Research\TVP\TVP Project Folder_updated_1_11_21\Project_Updates

Manufacturing Services

As noted above, several companies were employed to manufacture various powertrain components. These companies are listed here.

1. Distinctive Welding, Inc., Fort Collins. Welding (AL, Chromoly, they can do just about anything).
2. Northern Colorado Driveline, Greeley. Propulsion shaft shortening (they did it for free).
3. CSU EMEC, Fort Collins. Part G manufacture by Dr. Schaeffer.
4. Rapid Prototyping and Development Lab, Fort Collins (Powerhouse, run by John Mizia). Parts I and D. Utilize these guys as much as possible. They are in-house and turnaround times are very quick.
5. Alfred Manufacturing Co Inc., Denver. Part L manufacturing and WEDM. I have personal contacts here, so if you need their services let me know and I can get you setup. They also specialize in high volume stamping and plastic injection molding.

List of Abbreviations

17-4 PH	17-4 Precipitate Hardened
AE	Acceleration Event
AF	Anti-Freeze
AL	Aluminum
APP	Accelerator Pedal Position
APPS	Accelerator Pedal Position Sensor
ArbID	Arbitration Identifier
BMS	Battery Management System
CAD	Computer Aided Design
CAN	Controller Area Network
CCT	Continuous Cooling Transformation
Chromoly	Chromium-Molybdenum
CNC	Computer Numeric Control
CSU	Colorado State University
DC	Direct Current
ECM	Engine Control Module
ECU	Electronic Control Unit
EM	Electric Motor
EMC	Electric Motor Controller
EMEC	Engineering Manufacturing Education Center
EMI	Electro-Magnetic Interference
EMS	Energy Management Strategy
EVSE	Electric Vehicle Supply Equipment
FEA	Finite Element Analysis
FM	Frequency Modulation
FOS	Factor Of Safety
GUI	Graphical User Interface
HCAN	Hybrid Controller Area Network
HRC	Hardness Rockwell C
HSC	Hybrid Supervisory Controller
HV	High Voltage
ICE	Internal Combustion Engine
INV	Inverter
L2LPHE	Liquid-to-Liquid Plate Heat Exchanger
LSO	Low Side Output
LV	Low Voltage
NVH	Noise Vibrations and Harshness
OBC	On-Board Charger
P0-4	Parallel-0 to Parallel-4
PAE	Predictive Acceleration Events
PRNDL	Park, Reverse, Neutral, Drive, Low
Propshaft	Propulsion Shaft
TME	Tempered Martensite Embrittlement
TVP	Test Vehicle Platform
V2X	Vehicle-to-Everything
WEDM	Wire Electronic Discharge Manufacturing